Towards single-atom imaging of the unitary Fermi gas

Kunlun Dai

PSL UNIVERSITÉ PARIS

THÈSE DE DOCTORAT
DE L'UNIVERSITÉ PSL

Préparée à École Normale Supérieure

Towards Single-atom Imaging of the Unitary Fermi Gas

Soutenue par

Kunlun DAI

Le 03 11 2022

École doctorale n°564

Physique en Île-de-France

Spécialité

Physique Quantique

Composition du jury :

Prof. Denis Boiron Laboratoire Charles Fabry (Palaiseau)	*Rapporteur / Président du jury*
Dr. Sebastian Will Columbia University (New York)	*Rapporteur*
Dr. Juliette Simonet Universität Hamburg (Hamburg)	*Examinatrice*
Porf. Christopher Foot University of Oxford (Oxford)	*Examinateur*
Dr. Antoine Heidmann Laboratoire Kastler Brossel (Paris)	*Directeur de thèse*
Dr. Tarik Yefsah Laboratoire Kastler Brossel (Paris)	*Invité*

ENS | PSL

Département de Physique
École Normale Supérieure

Laboratoire Kastler Brossel

Thèse de Doctorat de l'École Normale Supérieure

Spécialité : Physique Quantique

présentée par

Kunlun Dai

pour obtenir le grade de docteur de l'École Normale Supérieure

---

Towards Single-atom Imaging of the Unitary Fermi Gas

Soutenue le 03 11 2022
devant le jury composé de :

M. Denis Boiron	. . . . .	Rapporteur / Président du jury
M. Sebastian Will	. . . . .	Rapporteur
Mme. Juliette Simonet	. . . . .	Examinatrice
M. Christopher Foot	. . . . .	Examinateur
M. Antoine Heidmann	. . . . .	Directeur de thèse
M. Tarik Yefsah	. . . . .	Membre invité

TABLE OF CONTENTS

List of Tables v

List of Figures vi

Introduction 1

Context 1

Objective of our experiment 4

Chapter 1: Experiment Overview 8

1.1 Experiment hardware 8

1.2 Laser system 11

1.2.1 ^{6}Li atomic structure 11

1.2.2 Laser table 13

1.2.3 High power infrared lasers 17

1.3 Around the science cell 19

1.3.1 Imaging axes 19

1.3.2 Feshbach and curvature coils 19

Chapter 2: From Laser Cooling to Evaporative Cooling 22

2.1 Laser cooling 22

2.1.1 Zeeman slower . . . 22
2.1.2 MOT and D_2 molasses . . . 23
2.1.3 D_1 gray molasses cooling . . . 25
2.2 Optical transport . . . 26
2.2.1 Loading performance . . . 28
2.2.2 Transport performance . . . 29
2.3 Preparation for evaporative cooling . . . 29
2.3.1 Feshbach resonance of ^{6}Li . . . 31
2.3.2 Spin population control . . . 31
2.3.3 Loading of the crossed dipole trap . . . 34

Chapter 3: Reaching Superfluidity . . . 37
3.1 Evaporation sequence . . . 37
3.1.1 Power ramp . . . 37
3.1.2 Evaporation efficiency in the crossed dipole trap . . . 37
3.2 Thermometry in axial-symmetric harmonic trap . . . 39
3.2.1 Thermometry using the Equation of State . . . 40
3.2.2 Temperature fit results . . . 42
3.3 A unitary Fermi superfluid . . . 45

Chapter 4: High Resolution Imaging system . . . 51
4.1 Microscope objective . . . 51
4.2 Choice of magnification . . . 55
4.2.1 Simulations of fluorescence images . . . 55

4.2.2 Imaging setup 60

Chapter 5: Optical Pinning Lattices 62

5.1 Laser sources and control 62

5.1.1 Lattice beam configuration 62

5.1.2 Turn-on sequence 64

5.2 Characterizing the pinning lattice 67

5.2.1 Estimated trapping frequency 67

5.2.2 Modulation measurements 69

5.2.3 Kapitza-Dirac scattering 71

5.2.4 Band mapping 74

5.3 Evaluating the pinning efficiency 75

5.3.1 A quick reminder on lattice band theory 76

5.3.2 Calculated structure for the pinning lattice 78

Chapter 6: Toward Single Atom Imaging 82

6.1 Cooling scheme 82

6.2 Laser setup 83

6.2.1 Laser source preparation 83

6.2.2 Laser orientations 85

6.3 Estimated cooling rate 86

6.3.1 Raman coupling strength 86

6.3.2 Estimated photon count 88

6.4 Raman sideband cooling result 90

Conclusion 95

Possible upgrades on the experiment 96

Outlooks 97

Appendix A: Electric dipole force on a two-level atom 101

Appendix B: Thermodynamic relations used for EOS fit 105

Appendix C: Absorption imaging 109

Appendix D: DMD setup 110

References 123

LIST OF TABLES

1.1 Feshbach and curvature coils field 20

2.1 Trapping parameters for IPG and ALS 36

2.2 Cooling performance summary before evaporation in CDT 36

4.1 Photon count per pixel vs. magnification 58

5.1 Trapping parameters for pinning lattices 68

LIST OF FIGURES

0.1 Neutron star 3

0.2 Phase diagram of 3D Fermi gases 5

1.1 Vacuum system 9

1.2 Main parts on the vacuum setup 10

1.3 ^{6}Li atomic structure 12

1.4 Zeeman energy shift of the ground state $2S_{1/2}$ 13

1.5 Optical table setup 14

1.6 Spectroscopy cell 16

1.7 Transport beam and the translation stage 18

1.8 Lasers around the science cell 18

1.9 Feshbach and curvature coils 21

2.1 Zeeman velocity groups 23

2.2 Sequence for MOT till D_2 molasses 24

2.3 MOT molasses detuning scan 24

2.4 D_1 cooling principle 26

2.5 Sequence for D_1 gray molasses 27

2.6 D_1 cooling performance 27

2.7 IPG loading from D_1 cloud 29

2.8 Heating against IPG holdtime 29

2.9 Optical transport curve 30

2.10 Scattering lengths a_{12}, a_{13}, a_{23} 32

2.11 Non-adiabatic RF sweeps 33

2.12 Loading into the crossed dipole trap 34

2.13 Breathing mode measurement in CDT 35

3.1 Evaporation laser power ramp 38

3.2 Comparison between two definitions of T/T_F 41

3.3 P/P_0 and T/T_F paramatrized on $\beta\mu$ 42

3.4 Density profile by the end of evaporation 43

3.5 Evaporation curves in ALS single dipole trap 44

3.6 Superfluid plateau 48

4.1 Objective resolution test setup 52

4.2 Objective resolution test result 53

4.3 Objective mount assembly 54

4.4 Statistics on the distance of nearest neighbor 57

4.5 Simulated fluorescence images 59

4.6 Vertical imaging lens setup 61

5.1 Pinning lattice laser setups 63

5.2 Flip mirrors for high power lasers 65

5.3 Control sequence for lattice turning on 66
5.4 Pinning lattice potential plot 68
5.5 Pinning lattice modulation 70
5.6 Measured trapping frequency against lattice power 71
5.7 Kapitza-Dirac scattering 73
5.8 Brilluoin zones of square and triangular lattices. 75
5.9 Band mapping on our triangular lattice 75
5.10 Numerical calculation on band structure example 77
5.11 Numerical calculation on lattice band structure 79
5.12 Pinning atoms into lattice bands 81

6.1 Raman cooling scheme 83
6.2 Raman laser source 84
6.3 Raman beam orientations 85
6.4 Estimated fluorescence photon count 89
6.5 Resolved Raman sidebands 91
6.6 Raman cooling performance 93
6.7 Raman fluorescence example figure 94

7.1 Z-lattice modification 96
7.2 Spin-resolved single-atom images 98
7.3 Fermi polaron 99
7.4 Tailored box potential 99

D.1 DMD setup 111

INTRODUCTION

Context

The perspective of exponentially faster computers, new ways to transmit and store information, and vastly improved sensing capabilities, led quantum science to become an extremely active area of research. These promises rely on physical realizations of large and well-controlled quantum systems. Along this front, the quantum science community has provided many platforms, each with its particular strength. For example, photons have already made quantum cryptography possible [1, 2, 3], superconducting qubits [4, 5] and trapped atoms/ions [6, 7, 8, 9, 10] are commercially pursued for universal digital computing, NV centers promise sensing with unprecedented spatial resolution [11, 12, 13]. With quantum gases of ultracold atoms, experiments have had tremendous success in tackling quantum many-body problems [14], which are notoriously complex owing to the large number of interacting particles, strong interactions, disorder, or nonlinear dynamics.

The contribution of quantum gas experiments in this quest is their ability to place a large number of particles in a well-characterized, tunable and isolated environment. For example, the energy landscape where particles evolve can be programmed at will to be uniform, harmonic, periodic, disordered, or even tightly-confining in one or more directions to simulate a 1D or 2D environment [15]. Inter-particle interactions can be short range or long-range, repulsive or attractive, vanishingly small or as large as allowed by quantum mechanics [16]. The ensembles can be prepared in thermal equilibrium, and dynamically driven Hamiltonians can be explored. The quantum gas toolbox goes beyond these examples and offers many capabilities to create quantum systems with incremental complexity, which was underlined by major breakthroughs over the last two decades in our understanding of quantum matter.

Among the various many-body quantum problems within reach of atom-based quantum simulators, strongly-interacting Fermi systems play a special role. Strongly-correlated fermions are indeed ubiquitous in nature, from the quark-gluon plasma of the early universe to neutron stars, and also lie at the heart of many modern materials such as high-temperature superconductors [17] and giant magneto-resistance devices [18]. The understanding of strongly-correlated fermions thus represents a pressing issue covering a wide fundamental and technological scope. For these systems, the large number of interacting particles involved indeed constitutes a serious challenge. But with the advent of ultracold atom plat-

forms – and concomitantly, the ability to place fermionic atoms in a well-characterized environmen, a whole new set of opportunities has opened to tackle this endeavor, as microscopic and macroscopic parameters can be tuned dynamically [14]. Due to this high level of control over the trapped fermions these quantum gas experiments are often referred to as quantum simulators and provide a unique approach to investigate correlated fermionic matter [19].

The BEC-BCS crossover

In recent decades there has seen a surge of experimental and theoretical efforts that aimed at probing the states of matter attainable in Fermi gases at ultralow temperatures. More precisely the system of interest here is a two-component Fermi gas, where the interaction between the two spin components is characterized by a single quantity — the scattering length a. Despite being a very simple description, this picture reflects the cold Fermi gas system quite accurately. Thanks to the low kinetic energy of these cold Fermi gases, their de Broglie wavelengths are much larger than the range of the interpartical Van der Walls interactions, which can be seen as short-range contact potentials. Therefore the cold fermions' collisional dynamics are not sensitive to the exact form of the interaction potential. In other words the Fermi gases are said to be in the s-wave scattering regime. As the interaction parameter $1/k_F a$ is changed from $-\infty$ to $+\infty$, this degenerate Fermi system evolves smoothly from the Bardeen-Cooper-Schrieffer superfluid [20, 21] (BCS) state to the molecular Bose-Einstein Condensate (BEC) state. The former consists of a fraction of losely bound, attractive Cooper pairs existing on the surface of the Fermi sea. The size of these Cooper pairs can be exponentially larger than the interparticle distance k_F^{-1}, and correspondingly the condensation temperature is reduced compared to the Fermi temperature by this exponent $\exp(-\pi/2k_F a)$. The molecular BEC is a condensate of the diatomic molecules that in general behave like bosons. At the limit $\dfrac{1}{k_F a} \to 0$, the interaction is as strong as allowed by quantum mechanics while the Fermi cloud bears many universal properties [22, 23], in the sense that the only remaining relevant length scale is k_F^{-1}. In consequence the thermodynamics of this strongly-interacting system resembles a non-interacting ideal Fermi gas. In particular, the ground state energy of a unitary gas is proportional to the Fermi energy by a constant called the Bertsch factor at zero temperature $E_{\text{Unitary}} = \xi E_F$. For finite temperature, this relation is only modified by a universal function $f\left(\frac{T}{T_F}\right)$. An implication of the universality of the unitary Fermi gas is that a cold cloud in the lab can be used to understand systems at drastically different length or temperature scales, such as neutron stars (figure 0.1).

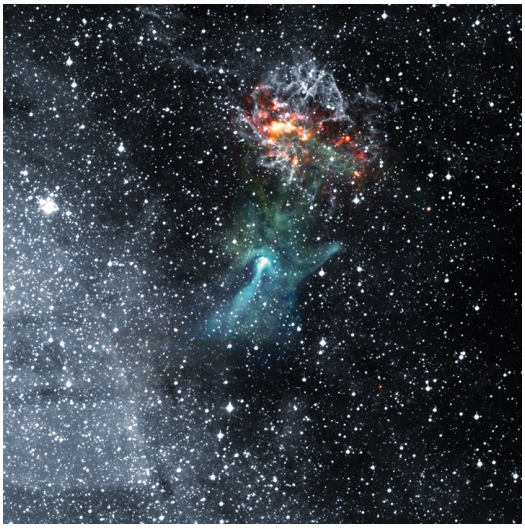

Figure 0.1: False color image of Pulsar PSR B1509-58 [24]. The inner crust consists of electrons, neutrons and remnant amount of nuclei. The neutrons are essentially a unitary Fermi gas with temperature on the order of $T = 10^9$ K and density $n = 10^{38}$ at/cm^3. This corresponds to $T/T_F \sim 0.01$ and is very similar to our lab condition despite of the completely different environment, thanks to the universal properties at unitarity.

Experimental tuning of the interactiong strength through Feshbach resonance [25, 26] was first demonstrated using Boson gases [27, 28]. Following the achievement of degenerate Fermi gas firstly in 1999 [29], and soon in six other groups [30, 31, 32, 33, 34], Feshbach resonances had been quickly explored in optically-confined two-component Fermi mixtures [35, 36, 37, 38] in 2002, and thence became a powerful tool to study the BEC-BCS crossover.

After the first observations of condensation on the BEC side [39, 40, 41] and on the BCS side [42], more and more groups have dedicated their work to measuring the properties of degenerate Fermi gas at or around the unitarity point. The research interests include thermodynamic measurements [43, 44], collective excitations [45, 46], RF spectroscopy [47], optical molecular spectroscopy [48], and direct observation of superfluid vortices [49].

In recent years, more quantitative results have been obtained from trapped fermions in inhomogeneous potentials, by precise measurements on the thermodynamic observables within local density approximation [50, 51, 52]. Through these measurements, the ground state equation of state has been determined in certain regions on the phase diagram (shown by figure 0.2) for the two-component Fermi gas. Specifically, for a spin-balanced gas at unitarity across the superfluid transition [50], and at the zero temperature limit throughout the crossover for a wide range of spin population imbalance [53]. Up to now, correlations in strongly interacting Fermi gases have not been systematically studied. Progress has been revolving around the short-range limit of the density-density correlation, which can be determined from the contact C [23, 54, 55]. The measuring techniques include RF spectroscopy [56, 57, 58], Bragg spectroscopy [59, 60] and three-body losses [61]. However, with the advent of quantum gas microscopy, more direct detection of correlations has become possible.

Quantum gas microscopy

High-resolution fluorescence imaging on cold atoms was initially applied in optical lattices to study the Mott insulator transition in Bose-Hubbard model [62, 63]. The deep lattices pin the atoms in position during the long interrogation time required by the fluorescence imaging. This technique can create images with a large signal-to-noise ratio, leading to a very high fidelity in reconstructing the cloud distribution to single atom level. Quantum gas microscopy immediately brought out enormous progress in many topics, including quantum magnetism [64], correlation [65], transport [66, 67, 68], spin-interactions [69], spin-entanglement [70, 71], and long-range interactions using Rydberg atoms [72, 73, 74].

Given the success of bosonic microscopes, many groups soon extended the tool to fermions [75, 76, 77, 78, 79]. Abundant results have also been obtained on probing Fermi-Hubbard systems, such as Mott insulator [80, 81], and long-range antiferromagnets [82, 83, 84]. However, quantum gas microscopes have been devoted only to the study of lattice physics and spin chains so far, and we plan to apply it to probe the physics in continuous systems.

Objective of our experiment

There have been extensive studies on the BEC-BCS crossover in the past decades, which have pushed our understanding on strongly correlated Fermi gases. However, the nature of the correlations and how they build up through the superfluid transition remain elusive.

When one considers the phase diagram of Fermi gases as depicted in figure 0.2, the vast majority of the parameter space remains uncharted. Past experiments have been conducted mostly in the deep superfluid regime, while the rich physics near the superfluid critical temperature T_c remains relatively unprobed. With our new generation setup, we aim at filling up measurements for phenomena happening near the superfluid transition, finding experimental support with highly quantitative perspective to the debates on many-body correlations. This will be done by incorporating cutting edge techniques such as quantum gas microscopy and tailored optical potentials [85, 86, 87].

As introduced above, most experiments on Fermi gases until today work with inhomogeneous potentials, which has the advantage of encompassing a full range of thermodynamic states over the size of the trap, that provides convenient thermometry. However, this also poses problem when one wishes to access a particular observable under particular thermodynamic conditions, because any probe addressing the whole cloud will detect responses that have been averaged and biased by the trap inhomogeneity. In our experi-

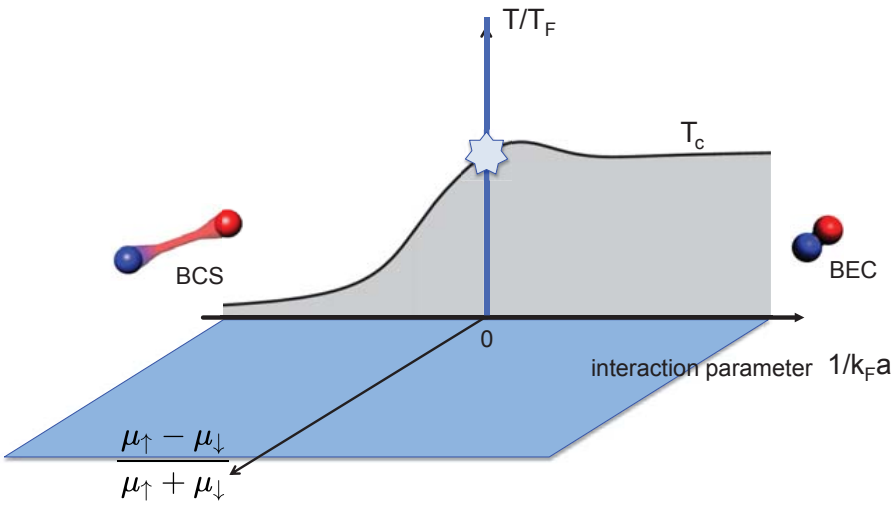

Figure 0.2: Phase diagram of a two-component Fermi gas, characterized by three axes: temperature as measured by T/T_F, interaction strength as measured by $k_F a$, and spin imbalance. The EoS has been measured experimentally at unitarity for spin-balanced gas [50] (blue solid line), and at low temperature limit [53] (blue-shaded plane). The large parts of the diagram remains uncharted.

ment design, instead, a tailored box potential will be used to create a spatial boundary to contain a homogeneous Fermi cloud inside. Combining with a microscope plus pinning lattice[a] to directly extract the density and spin correlations of the *bulk* gas cloud, our setup will be a useful tool to study the phase diagram near superfluid transition and in various interaction regimes. One interesting perspective is to look for the exotic FFLO phase [88, 89], which could only exist within a very narrow set of thermodynamic conditions near the "Clogston-Chandrasekhar limit" [90].

Thesis outline

The thesis introduces our experiment in two main parts. Part I looks at the preparation of a unitary Fermi gas and the cooling process that brings it to quantum degeneracy, where:

- Chapter 1 describes the hardware of the experiment, including the vacuum setup, the 671 nm laser system for cooling and imaging, and the coils for magnetic field control.
- Chapter 2 focuses on the laser cooling performance in the Magneto-optical trap (MOT) and in the D_1 molasses, as well as the preparation before evaporative cooling.

[a]The pinning lattice is only turned on during the acquisition of fluorescence photons, while the dynamics of the cloud is that of a 3D free fermions in space.

In particular, the optical transport and the spin balancing method using a RF sweep are discussed. The crossed dipole trap for evaporation is also characterized.

- Chapter 3 focuses on the evaporative cooling performance. The cooling result is a degenerate Fermi gas with relatively low density, that is suitable for single-atom imaging. Thermometry based on the equation of state (EoS) of the unitary Fermi gas inside the harmonic trap is described in detail and a superfluid plateau is demonstrated on a spin-imbalanced cloud.

Part II revolves on the setups and the preparations for the single atom quantum gas microscope, where:

- Chapter 4 describes the 2D + 1D pinning lattice that is used to pin the atoms during the exposure of a fluorescence imaging. The laser setups are shown and the lattices are characterized through parametric heating. The occupancy in the lattice bands is estimated by numerical calculations and also experimentally through band mapping.

- Chapter 5 focuses on the Raman sideband cooling process that is essential for the fluorescence imaging. The laser setup and some preliminary measurements are presented.

- Chapter 6 shows the high resolution objective setup. Some simulations on the fluorescence images are performed to help estimate the fluorescence image quality and to determine a proper choice of magnification in the imaging system.

Part I

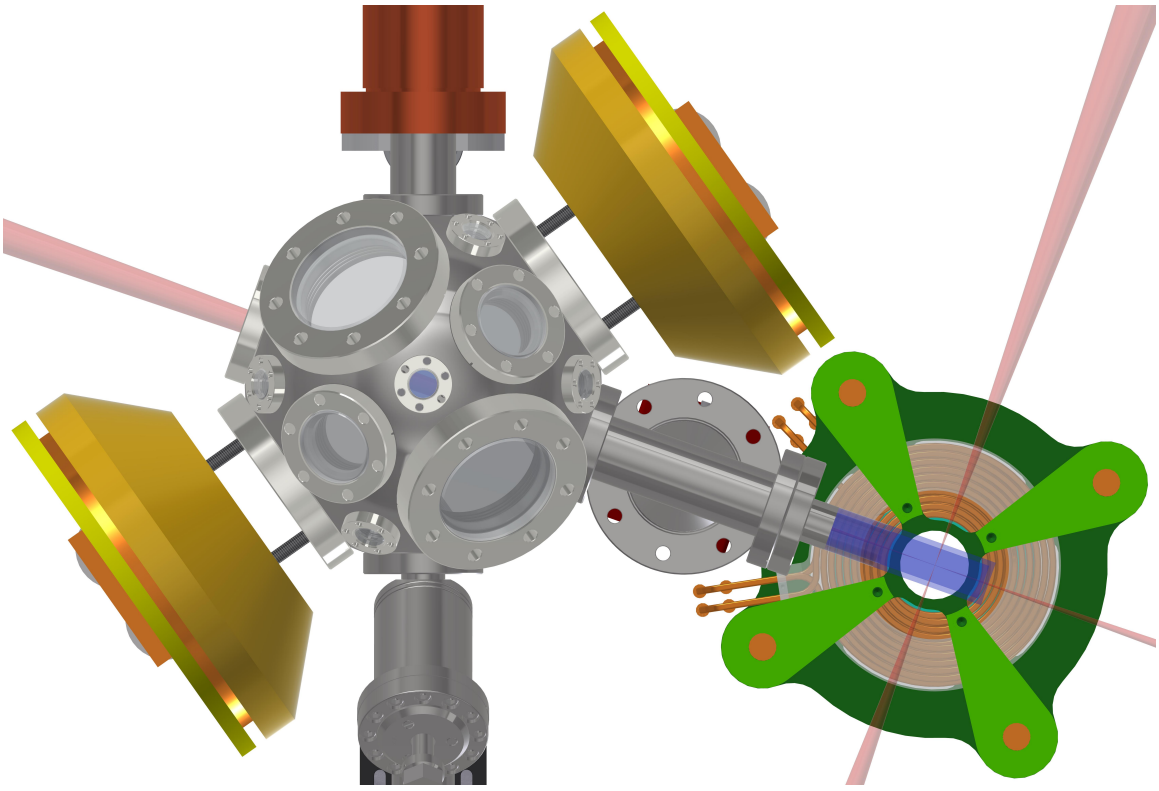

CHAPTER 1
EXPERIMENT OVERVIEW

In this chapter we describe the overall structure of the experiment setup, the vacuum system, and the laser table. Details on the laser cooling taking place at each part of the setup will be discussed in the following chapters.

1.1 Experiment hardware

The overall structure of our vacuum system is shown in figure 1.1. It consists of four main sections: the oven, the differential pumping sections, the MOT chamber and the science cell.

Oven

The oven is a T-shaped vacuum part containing lithium. Natural lithium consists of isotopes ^{6}Li (7.5% abundance) and ^{7}Li (92.5% abundance) [92]. Although our experiment now only works with ^{6}Li, the oven was initially loaded with 1 gram of natural Lithium and 1 gram of enriched ^{6}Li, hence containing roughly equal amount of ^{6}Li and ^{7}Li. The oven is heated around the narrow tube. The heater temperature is altered daily between 530°C while running the machine and 400°C when the machine is idle. This operation routine ensures that we have stable atomic flux within 15 minutes of heating, without clogging the thin tube when idle.

The oven is isolated from the later part of the experiment by differential pumping tubes to maintain a low pressure in the main experiment. Two ion pumps are installed next to the isolation valves, one on the oven side and one on the Zeeman window side. Four additional getter pumps[a] provide higher pumping capacities by absorbing residual gases into the getter material. Two of these getter pumps are before the Zeeman slower and two are next to the MOT chamber. With these pumping power, we obtain a good vacuum on the order of 1×10^{-11} Torr in the MOT chamber.

[a] model No. NexTorr D 200-5, NexTorr D 500-5

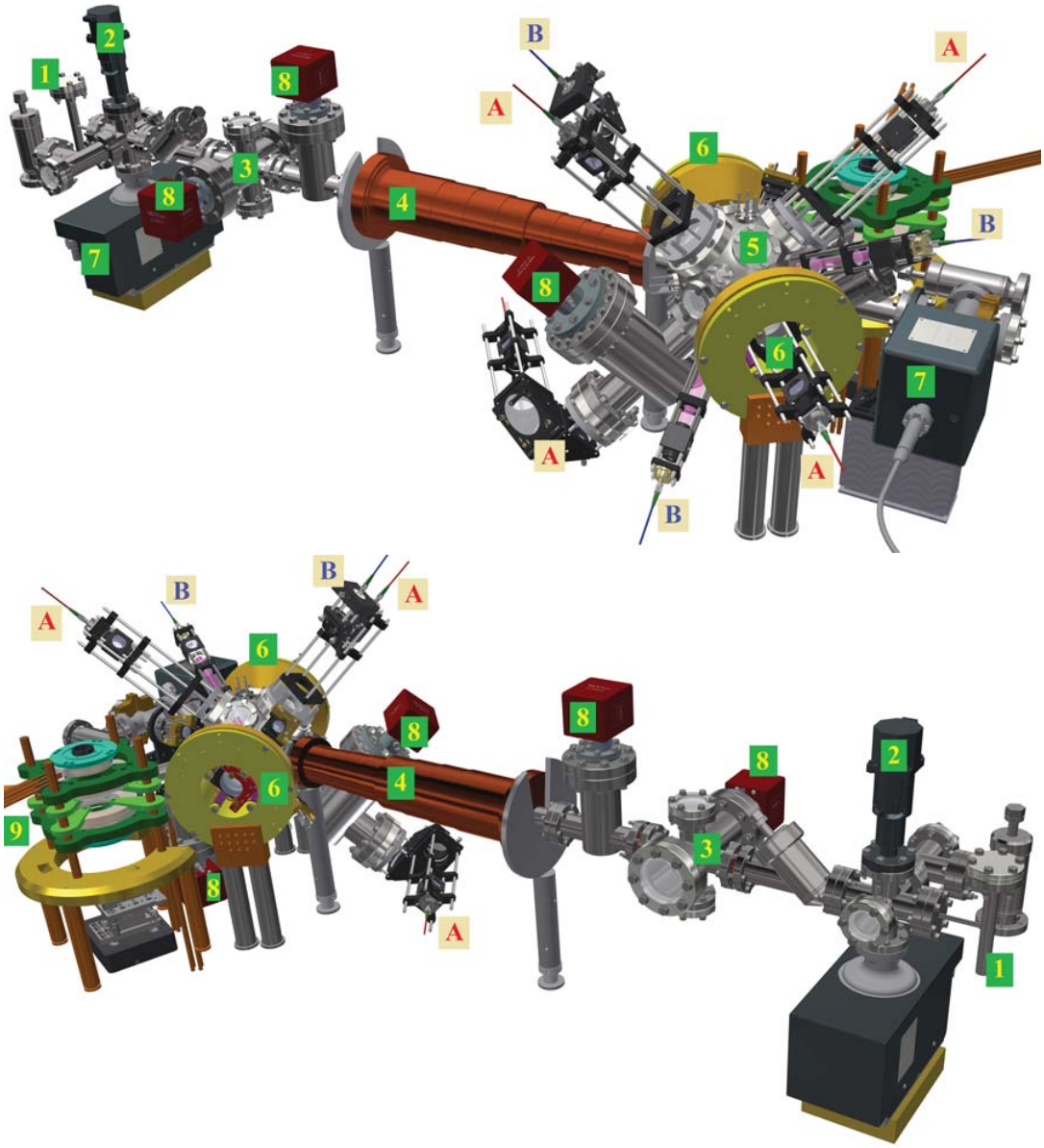

Figure 1.1: 3D drawings of the vacuum setup: (1) lithium oven, (2) oven shutter, (3) differential pumping section, (4) Zeeman slower, (5) MOT chamber, (6) MOT coils, (7) ion pumps, (8) SAES getter pumps, (9) science cell section with Feshbach & curvature coils. (A) MOT beams. (B) gray molasses beams. Adapted from [91].

(a) (b) (c)

Figure 1.2: CAD drawings of main vacuum parts: (a) Lithium oven, (b) MOT chamber, the view is facing one of the CF40 viewport, (c) The science cell.

MOT chamber

The MOT chamber is a spherical cube[b] structure with multiple CF viewports for optical access. As seen in figure 1.1, on the face positions of the spherical cube, the 6 largest CF63 viewports are reserved for MOT molasses beams. Among the three pairs of orthogonal MOT beams, two are prepared by retro-reflection and one by counter-propagating beams. On the outer rim of these viewports three pairs of compensation coils are mounted to cancel the magnetic field precisely during the D_1 molasses cooling. The MOT coils are larger in size and are installed further back with the coil axis aligned along one molasses pair that is parallel to the table. On the corner positions of the spherical cube, there are 8 CF40 viewports, among which 6 have been occupied: One pair is along the Zeeman slower axis, one pair is along the optical transport axis, and one pair is used for MOT chamber absorption imaging. The remaining 12 edge positions have CF16 viewports, most of which remains available. Two of the CF16 viewports let through counter propagating gray molasses beams. The last axis of the gray molasses shares the same viewport as one of the MOT molasses, and therefore is not exactly orthogonal to the first two axes.

Science cell

To study the physics near unitarity, the cloud will be transported optically (in an optical tweezer, see 1.2.3) about 30 cm away to a Borofloat glass cell with special AR coating. When incident angle is smaller than 30°, the reflection is measured to be below 0.3% for 1064 nm light and below 0.2% for 671 nm light. The science cell therefore provides a wide optical access for the pinning lattice (chapter 5.1) and for the microscope (chapter 4). This

[b] Kimball Physics MCF450-SphCube-E6C8A12

science cell has inner dimension $20 \times 20 \times 60\,\mathrm{mm}^3$ and a thickness of 3 mm. The cell is connected to the main vacuum structure by a rotatable CF flange. The orientation of the cell was checked during assembly with a self-made Michelson interferometer to make sure that the top and bottom surfaces are parallel to the horizontal plane. The front surface comes with a 1° tilt in the design to avoid creating an optical cavity with mirrors in earlier optical paths.

1.2 Laser system

1.2.1 ^{6}Li atomic structure

Lithium is the lightest alkali metal with atomic number $Z = 3$. There are two natural occurring isotopes — ^{6}Li, a fermion, and ^{7}Li, a boson. In this experiment we work with ^{6}Li. The ground state of Lithium has electron configuration [He]$2s^1$, where the first shell is completely filled and shell 2 contains one single electron. Like other alkali metals, the simple atomic structure due to the transition of this free electron allows all kinds of manipulation through atom-light interactions. We perform laser cooling, trapping and imaging on ^{6}Li all through its 671 nm *D*-lines. The UV transition to higher excited state is not used in our experiment, but can also be exploited in a MOT [93]. Figure 1.3 shows the wavelengths of the *D*-lines, the hyperfine structures in $2P$, and the transitions that are used in our experiment.

The *D*-line has natural linewidth $\Gamma = 2\pi \times 5.87\,\mathrm{MHz}$. Whereas the hyperfine constant a_{hf} for $2P_{1/2}$ and $2P_{3/2}$ are 17.39 MHz and -1.16 MHz respectively [94]. Therefore the D_2 hyperfine levels are not resolved. Both the D_2 and D_1 molasses beams are detuned from resonance by several Γ to provide the dissipative force in the molasses and keep the atoms trapped. Before taking images of the atoms, they are not guaranteed to be in the same hyperfine manifold in the ground state. Therefore a repumper light is shined on shortly to bring all atoms in the $F = 3/2$ state, and the subsequent absorption imaging light has frequency targeting transition from $F = 3/2$ to the $2P_{3/2}$ excited state.

Under external magnetic field, the degeneracy of the Zeeman states in the hyperfine structure is lifted. As the Zeeman shifts become larger compared to the hyperfine splitting, the good magnetic quantum numbers changes from m_F to m_I and m_J, where subscripts I and J denote the nuclear spin angular momentum and the fine structure angular momentum. The energy eigenvalues in the new basis at various magnetic field strength B can be

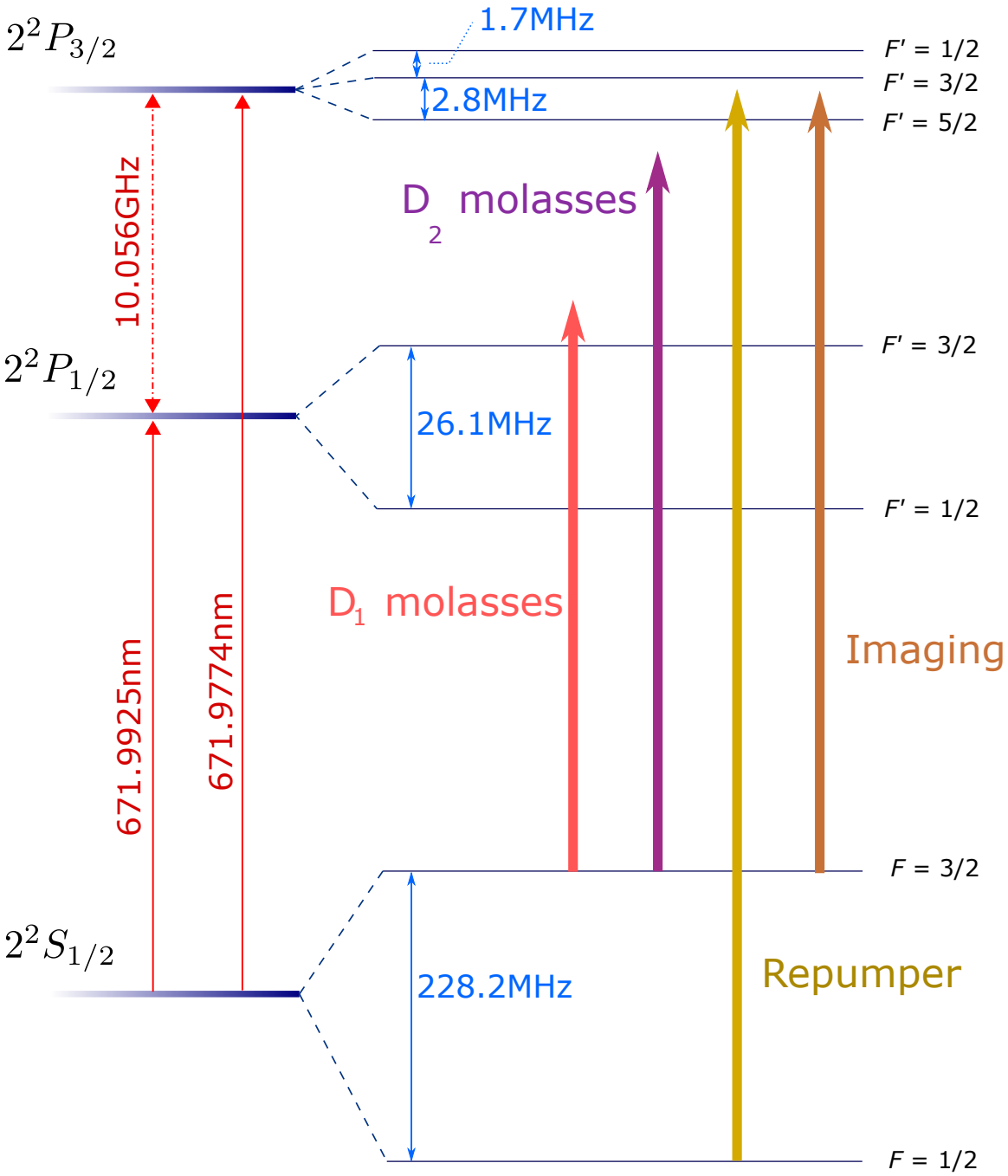

Figure 1.3: *D*-line of ^{6}Li atom. D_1 and D_2 lines are 671 nm red and are 10.06 GHz apart in frequency. The natural linewidth is 5.87 MHz. The hyperfine levels of $2P_{1/2}$ are resolved but those of $2P_{3/2}$ are not. The imaging light uses the D_2 transition targeting $F = 3/2$ ground hyperfine state, whereas the repumper light targets $F = 1/2$ ground state.

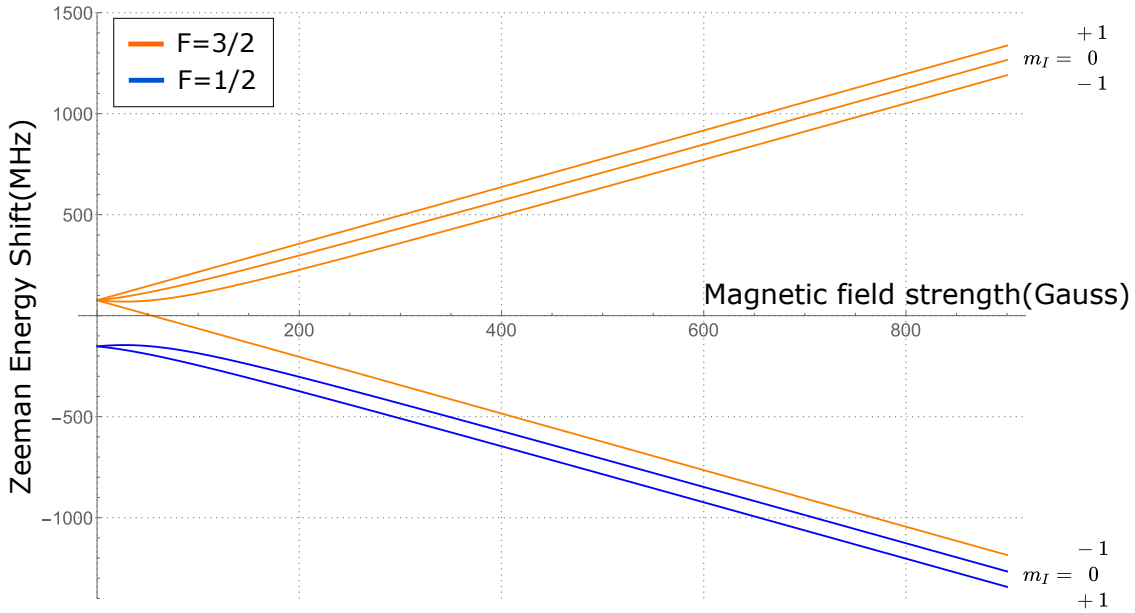

Figure 1.4: Zeeman energy shift of the ground state $2S_{1/2}$

calculated via the Breit-Rabi formula [95]

$$E(m_F)_{\pm} = -\frac{a_{\text{hf}}h}{4} + g_I m_F \mu_B B_z \pm \frac{a_{\text{hf}}h(I+\frac{1}{2})}{2}\sqrt{1+\frac{2m_F\xi}{I+\frac{1}{2}}+\xi^2}, \tag{1.1}$$

With $\xi = \dfrac{(g_I - g_J)\mu_B B}{a_{\text{hf}}h(I+\frac{1}{2})}$. a_{hf} is the hyperfine constant and g_I, g_J are the nuclear and electronic g-factors.

Figure 1.4 shows the energy shift with respect to the fine structure level for the six Zeeman states in $2S_{1/2}$. They are labeled $|1\rangle$ to $|6\rangle$ from lowest to highest energies. Among these, the two lowest Zeeman states are usually taken as the spin up and down states in quantum simulations using ^{6}Li. The Feshbach resonance between these two states will be discussed later in section 2.3.1.

1.2.2 Laser table

On a separate laser table we prepare all the laser beams required for the cooling and imaging on the main setup, where they are sent through optical fibers. Two lasers of the model "Toptica TA-pro" serve as the sources for D_1 and D_2 beams. The former includes the three retro-reflected gray molasses beams; The latter includes the Zeeman beam, molasses beams

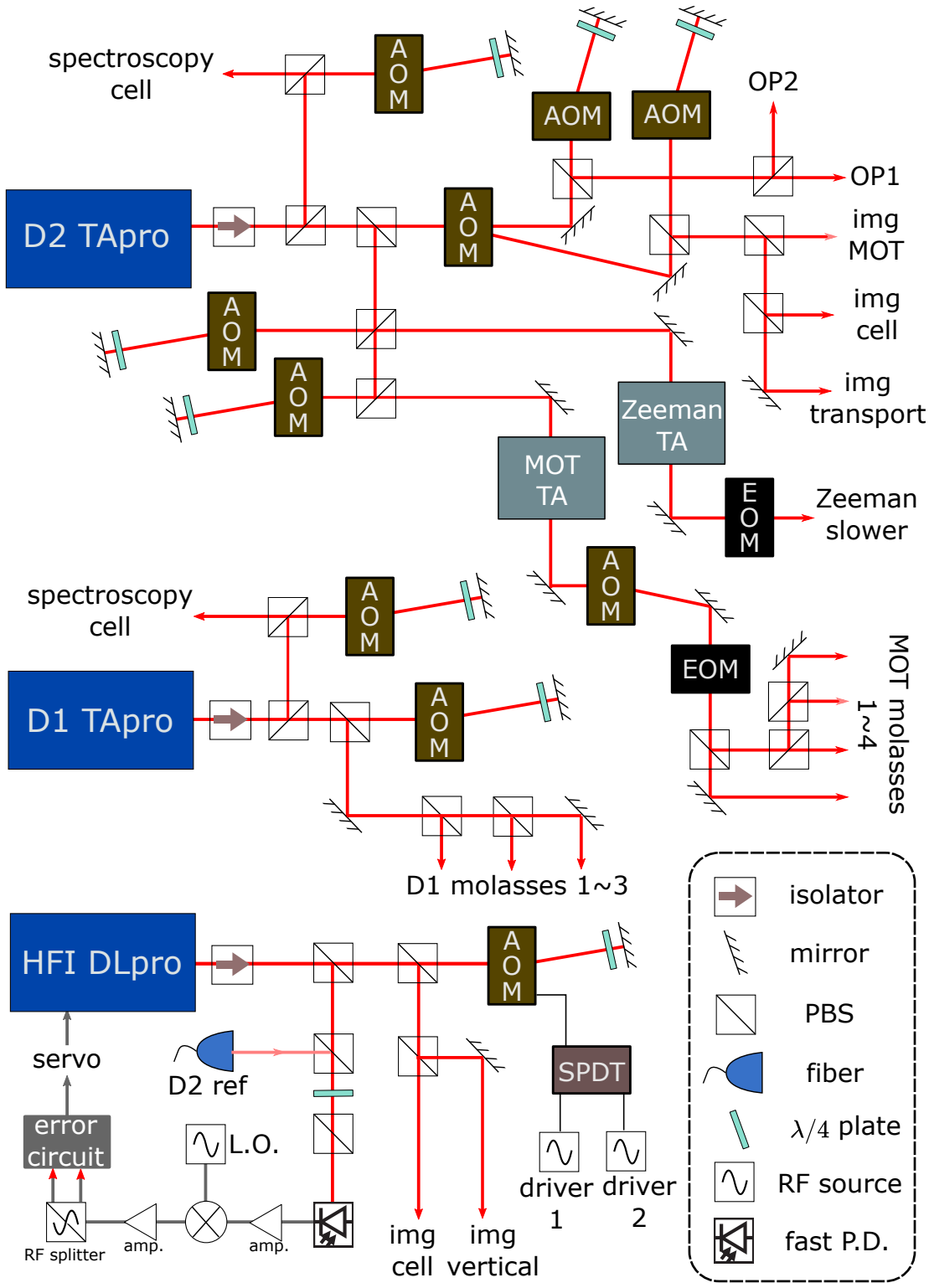

Figure 1.5: Arrangement on the optical table. D_2 laser provides Zeeman slower beam, MOT molasses beams, imaging and repumper light at zero field; D_1 laser provides D_1 molasses beams; HFI laser provides imaging light at arbitrary magnetic field. D_2 and D_1 lasers are locked on ^{6}Li spectrum, whereas HFI laser is locked on D_2 laser with a tunable offset.

for the MOT, absorption imaging beams and optical pumping beams. The Toptica TA-pro is a pre-aligned setup that consists of an external-cavity diode laser (ECDL) seed laser and a tapered amplifier (TA) chip. The frequency of each master is stabilized by locking them on ^{6}Li D_1 and D_2 spectral line respectively.

To prolong the lifetime of the TA-pro lasers, we drive them below their nominated maximum current, and typically obtain 210 mW power. After passing through AOMs, the remaining power is not enough to distribute over all required beams. In particular, Zeeman beam and MOT molasses beams are telescoped to large waists to capture enough atoms from the oven, while their intensities need to be maintained at several times the D_2 saturation intensity $I_{\text{sat}}(D_2) = 2.54\,\text{mW/cm}^2$. Therefore we add in additional self-mounted TA chips from Eagleyard to gain in power. Eventually, we are able to obtain 80 mW on the Zeeman beam with 10 mm waist on the main setup, equivalent to $20\,I_{\text{sat}}$; MOT molasses beams each has 10 mW over 7 mm beam waist, equivalent to $5\,I_{\text{sat}}$; D_1 molasses beams each has intensity[c] $30\,I_{\text{sat}}$. Their detunings are optimized based on the cooling performance and are mentioned in the next chapter 2.1. The remainging beams for imaging and repumping typically have powers below 1 mW.

Lithium laser spectroscopy

To stabilize the master diode of D_2 and D_1 TA-pro frequency, we perform a frequency lock on the spectral line using a spectroscopy cell, as shown in figure 1.6. The laser beam to be locked is split into a probe beam below saturation intensity and an over-saturated pump beam. By overlapping the two beams in counter-propagating manner, one can obtain a Dopper-free absorption spectrum from the probe beam. In order to lock on a dip on the absorption feature, modulation transfer spectroscopy technique [96] is applied by adding an EOM on the pump beam. A Pound-Drever-Hall module then demodulates the absorption spectrum and converts an absorption dip into a zero-crossing in the error-signal.

The D_2 laser is locked on $F = 3/2 \rightarrow F'$ transition peak, whereas D_1 laser is locked on the crossover between $F = 1/2 \rightarrow F'$ and $F = 3/2 \rightarrow F'$ transitions.

High field imaging

From the D_2 TA-pro, one set of imaging and repumper beams are responsible for the absorption imaging at zero magnetic field. In addition to this, we would like to be able to also see the atoms at a non-zero field, especially at 832 Gauss, which is the unitarity point

[c] To avoid confusion, the D_1 molasses intensity is still given in units of the D_2 line saturation intensity $I_{\text{sat}}(D_2)$ = 2.54 mW/cm^2. Notice the saturation intensity 7.59 mW/cm^2 for D_1 line is three times higher.

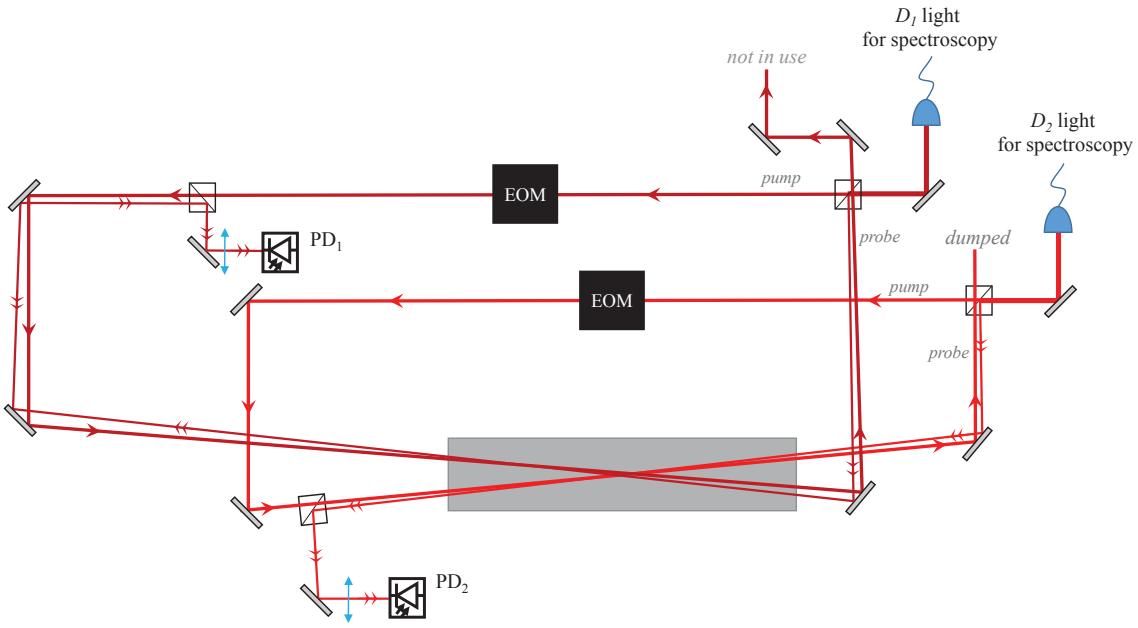

Figure 1.6: Spectroscopy cell for frequency lock on a Doppler-free absorption spectrum.

for ^{6}Li Feshbach resonance between the lowest two hyperfine states (see figure 1.4). At this magnetic field, the energy levels of the two lowest hyperfine ground states are shifted by more than -1 GHz. Using σ_- imaging light, the transition is cycling and therefore no repumper light is needed. The corresponding excited state in $2P_{3/2}$ has Zeeman shift of roughly -2.3 GHz. In the end, the imaging frequency at unitarity is about 1GHz red-detuned with respect to the imaging frequency at zero field. Also, the two spin states are no longer degenerate. Their imaging frequencies are separated by 76.8 MHz.

We use another Toptica DL-pro laser head as the source for high field imaging light. Its frequency is offset-locked on the D_2 laser using a side of filter technique [97]. In this technique, the reference laser and the high field imaging laser are first mixed, and their beatnote picked up by a fast photodiode[d] with 30 ps rise time. The beatnote is then mixed down once more with a local radio frequency (RF) oscillator to produce a signal on the MHz scale. Using a RF splitter, a filter and a set of rectifiers, the fast change in the RF filter gain near its cutting frequency is converted to a zero crossing in the error signal. The slave laser frequency is hereby locked on the edge of the RF filter, and the offset frequency can be changed using the local oscillator. In our experiment we use DS instrument SG4400L as the local oscillator, which allows our high field imaging light to be locked anywhere within 4.4 GHz offset from the D_2 line.

One AOM double pass on the high field imaging laser allows the exact control of the

[d] Hamamatsu G4176-03

imaging frequency. In combination with a solid state switch ZASWA-2-50DRA+, one can switch fast between two driving frequencies for consecutive imaging of the two spin states.

1.2.3 High power infrared lasers

Apart from 671 nm red lasers, our experiment also uses high power infrared lasers that are far red-detuned from lithium lines. These IR lasers are important in creating trapping potentials for transport, evaporation and creating the pinning lattice.

Transport laser beam

The laser source for the optical tweezer is a high power 1070 nm continuous wave Ytterbium laser from IPG photonics[e]. The maximum power out of the fiber is 200 W but we operate it at 160 W on a daily basis. The IPG laser is focused on the atom cloud with a 85 μm beam waist. The transport is done by moving the focus position mechanically through the displacement of two mirrors on a translation stage from Newport[f]. The optical setup is shown in figure 1.7. The traveling range of the stage is 16 cm. By folding the optical path upon reflections on two rectangular mirrors[g] installed on the stage, we can move the IPG focus by 32 cm, which is enough to cover the 31.5 cm distance from MOT chamber center to the cell center. The motion of the stage can be remotely controlled via a analog position-setting signal. The maximum traveling speed it can follow is 0.3 m/s. The actual transport control is explained in section 2.2.2.

The IPG power can be reduced by three orders of magnitude during evaporation (see section 3.1). This is done with a high-extinction-ratio polarizing cube and a halfwaveplate on a motorized rotational mount[h].

Cross dipole beam

Apart from the transport beam, three other high power infrared lasers are used in our experiment. These 1064 nm continuous wave lasers[i] from Azur Light System (ALS) provide maximum output 45 W. One ALS laser (later referred to as "the cross dipole beam") is shone across the cell perpendicular to the transport beam, in order to create a crossed dipole trap to accelerate the evaporation process. The other two ALS lasers are used to

[e] IPG YLR-200-LP
[f] Newport XMS160-S
[g] Laseroptik L-15116 HR1064-1070 nm/45° 75×50×5 mm
[h] OWIS DRTM 40
[i] Azur Light System ALS-IR-50-SF

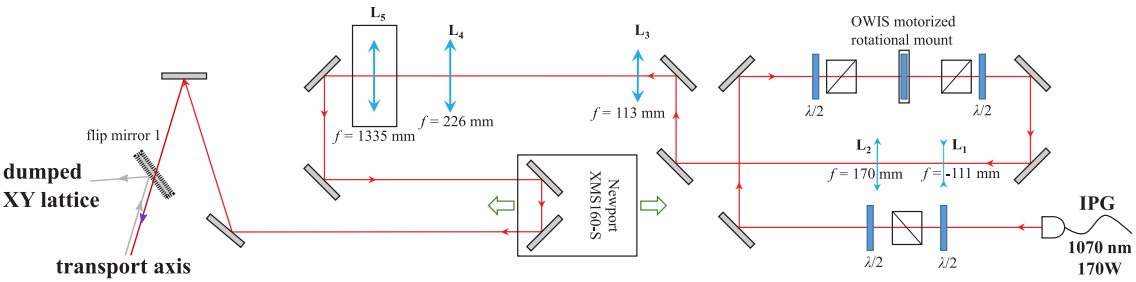

Figure 1.7: Transport IPG laser and the translation stage. A halfwaveplate on rotational motor is used to control the transmitted power over three orders of magnitude. The transport range is 32 cm.

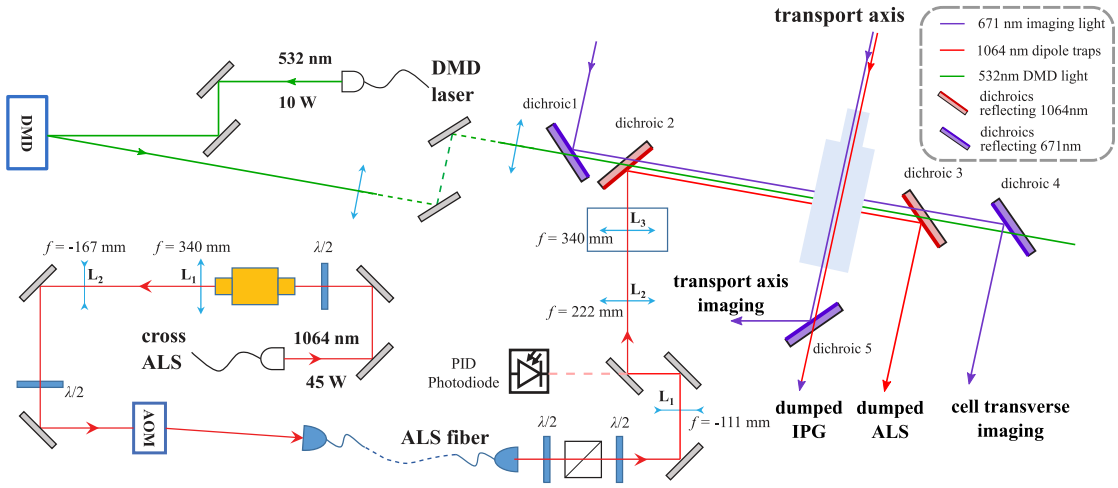

Figure 1.8: Lasers around the science cell: A 45 W ALS laser shines along the transverse axis of the cell and provides additional trapping during evaporation. It is overlapped with a cell transverse imaging beam. Two types of dichroics are used to overlap and separate lasers of different wavelengths. A green laser for gravity compensation is contemplated to be installed in the future (see section 6.4).

form pinning lattices in the horizontal plane and along the vertical direction. They will be introduced later in section 5.1.

The cross dipole beam is brought around the science cell by a high power fiber. 15.5 W power out of the fiber is focused to 60 μm waist at the atoms position. The laser power is regulated by an AOM. The power after the fiber is detected by a photodiode and used in a servo-loop to feed back onto the AOM driving RF power. This power regulation allows the beam power to be ramped down reliably to 30 mW at the end of evaporation.

1.3 Around the science cell

1.3.1 Imaging axes

Four imaging axes along different directions have been setup to see the atom clouds throughout the experiment sequence. One axis goes diagonally up through the MOT chamber and is used for imaging the atoms from MOT loading stage to the D_1 gray molasses stage. One axis is along the optical transportation. The 671 nm imaging light is overlapped with the transport beam before the MOT chamber viewport with the help of a dichroic with reflective coating[j] for 1064 nm. They are separated after the cell by a dichroic mirror of a second type of coating[k]. On this imaging axis we can switch the object plane from MOT chamber to science cell by replacing one lens on the imaging path.

Two imaging axes are available for the science cell. One is the vertical imaging through the high-resolution objective, as will be introduced in chapter 4. The other is looking from the side of the cell perpendicular to the transportation axis, which we call the cell transverse imaging. On this axis the imaging light is overlapped with the 1064 nm cross dipole beam. An illustration on the optical paths is given in figure 1.8.

1.3.2 Feshbach and curvature coils

Above and below the science cell, one pair of Feshbach coils and one pair of curvature coils are mounted. Two winded Feshbach coils with inner radius 43 mm and outer radius 73 mm are in Helmholtz configuration to provide a uniform magnetic field near the atoms position in the vertical direction. In the experiment we typically send 246 A current through 22 turns in each Feshbach coil to produce 832 Gauss magnetic field. Due to limited precision on the winding and the geometry, the Feshbach coils also create a small but non-negligible magnetic curvature. To provide additional magnetic trapping in the plane when optical traps are turned off, a pair of curvature coils are mounted further apart with the same central axis. They each have 14 winded coils with inner radius 26 mm and outer radius 46.5 mm. They also run parallel current and produce a magnetic field in the vertical direction with smaller amplitude but larger curvature.

Figure 1.9 shows the geometry and the simulated magnetic field from both coils. Table 1.1 summarizes the estimated field and curvature at the geometric center of the coils. For Feshbach coils we have also performed calibrations on the field strength based on RF spectroscopy, as well as calibrations on the field curvature based on free-fall of the atoms.

[j] HR1064-1070 nm/45° R> 99.9%; HT671 nm R< 0.8%; HT532 nm R< 3%

[k] HT1064-1070 nm/45° R< 0.7%; HR671 nm R> 99.9%; HT532 nm R< 1.5%

	$B_z(z=0)$ (G/A)	$B_z''(z=0)$ (G/cm^2/A)
Feshbach coils	3.34	0.0188
Feshbach (measured)	3.37	0.033
Curvature coils	0.66	0.104

Table 1.1: Summary of the simulated magnetic field strength and curvature at the geometric center of the coils, and the measured value for Feshbach coils. The measured field strength by Feshbach coils is in good agreement with the simulation. The curvature shows a larger discrepancy, probably originated from the geometric size of the coils and the imperfect positioning of the atoms with respect to the coils geometric center.

The measured field strength and curvature are also recorded in the table.

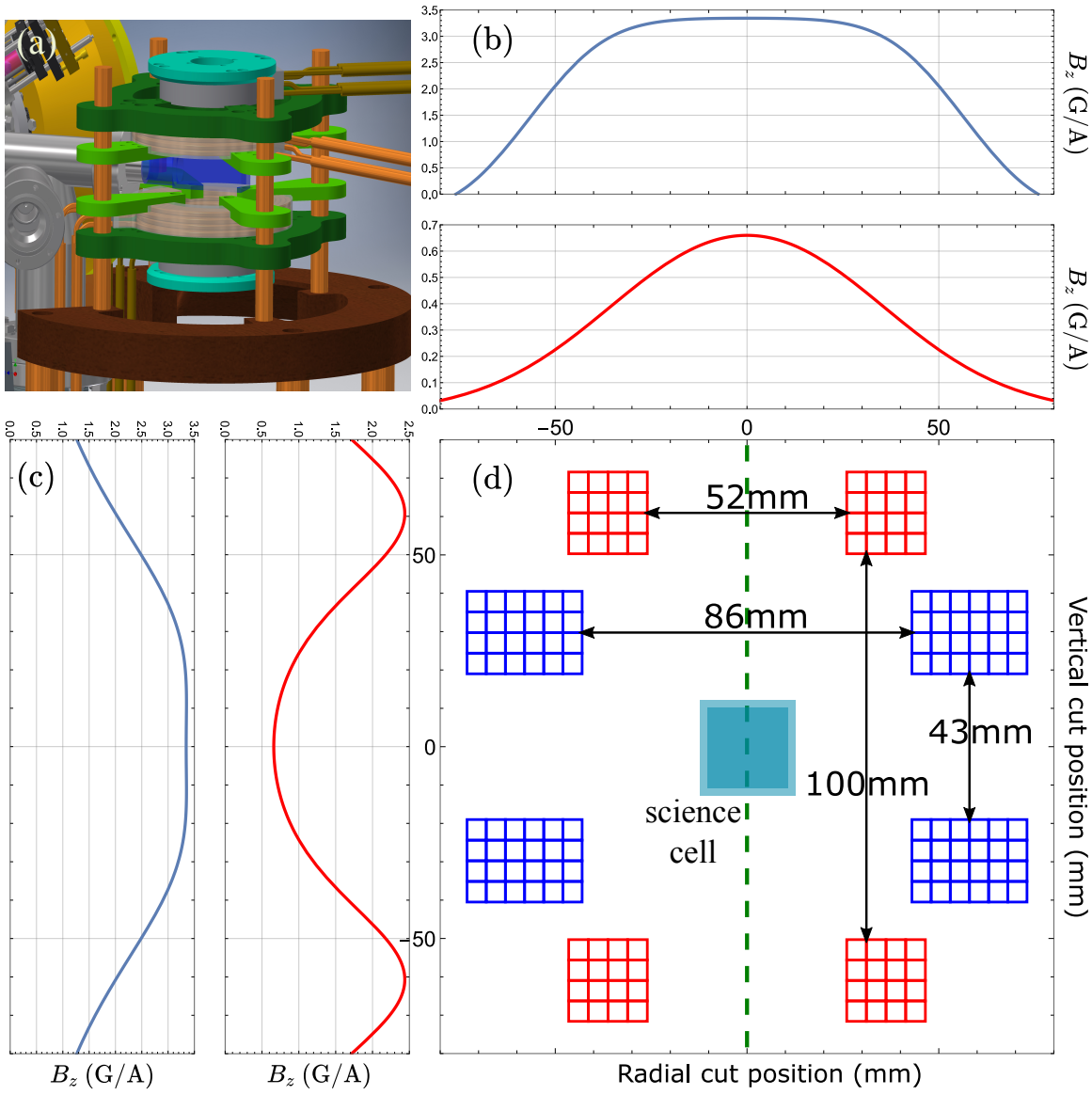

Figure 1.9: Feshbach (blue grids) and curvature (red grids) coils: (a) The coil mount around science cell. (b,c) simulated magnetic field vertical component based on the out-of-factory geometry of Feshbach and curvature coils. (d) a cross-section view showing the geometry of the coils.

CHAPTER 2
FROM LASER COOLING TO EVAPORATIVE COOLING

This chapter deals with the Doppler and molasses cooling, as well as the transfer of the atoms from the oven to the MOT chamber, then to the crossed dipole trap in science cell. Further evaporative cooling and single atom imaging will take place in the science cell.

2.1 Laser cooling

2.1.1 Zeeman slower

The Zeeman slower performs the initial cooling from the oven, so that at the end of the slower, the cloud is cold enough to be captured by the MOT. The deceleration of the atomic gas comes from the radiation pressure of the "Zeeman" light. For atoms with velocity $\mathbf{v}$ experiencing Doppler effect, the head-on collisions with photons with wave vector $\mathbf{k}$ impart a radiation force [98]

$$\mathbf{F}_{\text{abs}} = \hbar\mathbf{k}\frac{\Gamma}{2}\frac{s}{1+s}\left(1+\frac{2\mathbf{k}\cdot\mathbf{v}\Delta}{(1+s)(\Delta^2+\Gamma^2/4)}\right) = F_0 - \beta v. \tag{2.1}$$

Here $s = \dfrac{I/I_{\text{sat}}}{1+4\Delta^2/\Gamma^2} = \dfrac{2\Omega^2}{\Gamma^2+4\Delta^2}$ is the saturation parameter. Detuning $\Delta = \omega_{\text{laser}} - \omega_{\text{atom}}$ depends on the local magnetic field strength through the Zeeman shifts. With carefully designed magnetic field that decreases with the atom velocity, effective cooling will happen over the whole length of the Zeeman slower.

Our slower design has total length 60 cm. The maximal magnetic field created is about 650 G at the oven end. A spin flip point where magnetic field changes sign occurs 10 cm before the MOT end. Figure 2.1 shows the estimated and measured magnetic field, as well as the velocity curves of various velocity groups. Lithium atoms with initial velocity below 830 m/s can be captured by this slower and cooled down to less than 50 m/s before the MOT chamber. The cooling light has 80 mW power and roughly 1cm beam diameter, giving a saturation parameter $s_0 \approx 20$. The laser detuning is -300 MHz with respect to D_2 transition. A 228 MHz sideband is created from an EOM to serve as the repumper when spin flip happens.

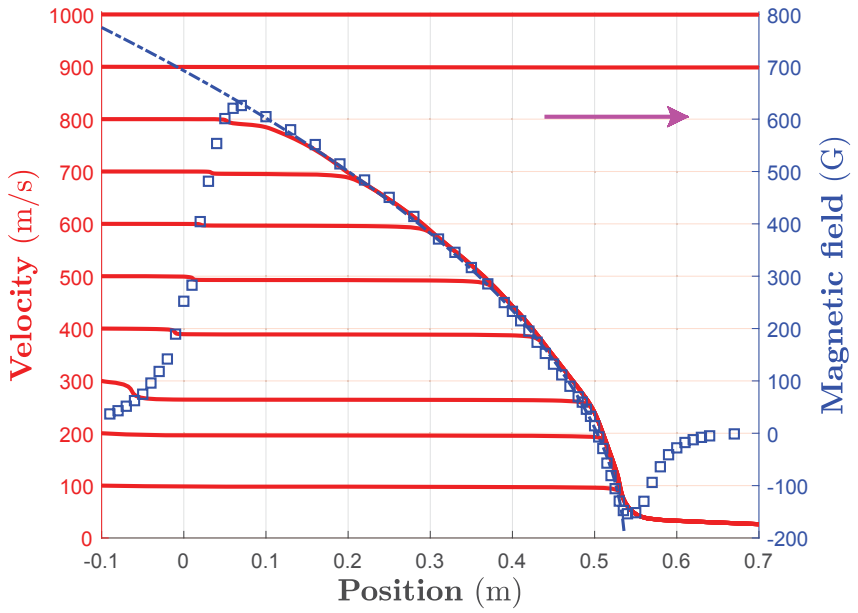

Figure 2.1: Change of Lithium gas velocity along the distance in the Zeeman slower. Dashed blue line and blue squares show the calculated and measured magnetic field respectively. Red lines denotes different velocity groups. The highest capturable velocity is 830 m/s.

2.1.2 MOT and D_2 molasses

The cooling in the MOT chamber is performed in several steps to prepare for an efficient optical transport in the later sequence. The MOT coils are turned on at 10 G/cm during the initial MOT loading time. For a 1.5 s loading sequence, we are able to capture 1×10^9 atoms in a MOT cloud of roughly 3 mm size, slightly more squeezed along the MOT coil axis. The cloud diameter is compressed to $\approx$ 2 mm in the following 50 ms magnetic gradient ramp. The cloud temperature of the compressed MOT is about 1.2 mK. Afterwards, there is an additional 3 ms D_2 molasses stage during which the magnetic field is turned off. The molasses beam intensities and detunings are changed at the same time. The intensity of each molasses arm is reduced to 25% of its initial value, and the molasses frequency approaches resonance from -3.4Γ to $-\Gamma$. By the end of this ramp, the cloud temperature goes down slightly to 900 μK without significant atom loss. This D_2 molasses stage allows the eddy current induced by the magnetic shut-off to settle down, which ensures a good field cancellation for the following D_1 cooling. Figure 2.2 describes the control sequence from MOT to D_2 molasses. In figure 2.3 two scans on the initial and final molasses detuning are shown, from which it can be understood how the values of the detunings are chosen.

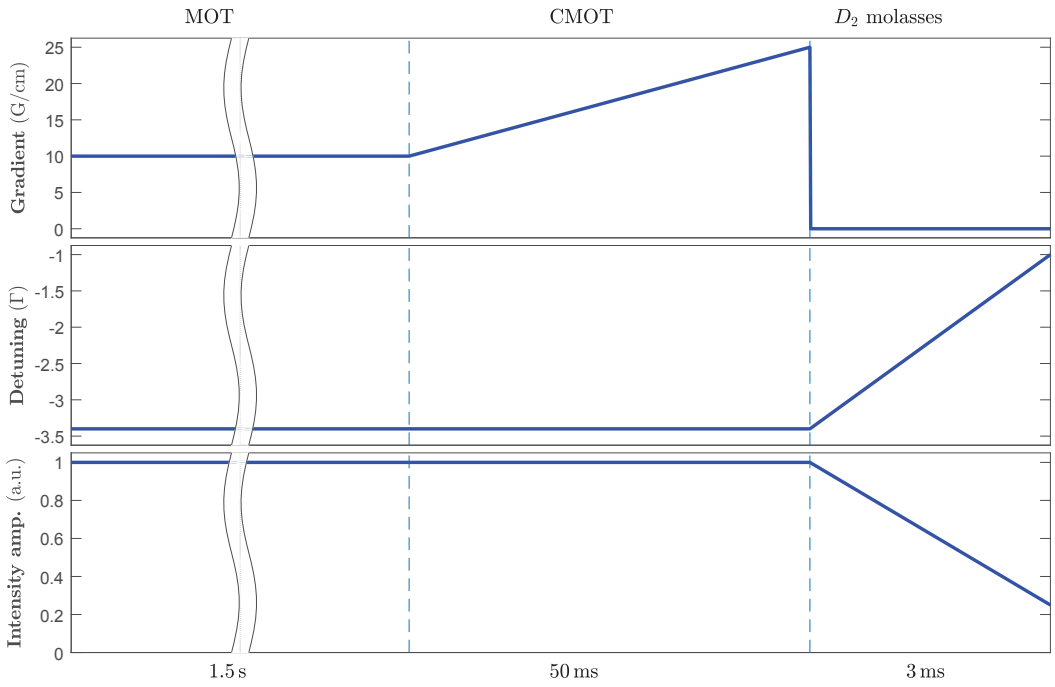

Figure 2.2: The control sequence from MOT until D_2 molasses. The compressed MOT stage contains a field gradient ramp from 10 G/cm to 25 G/cm; The D_2 molasses stage contains a detuning ramp from -3.4Γ to $-\Gamma$ and an intensity ramp to a quarter the initial intensity. Adapted from [91].

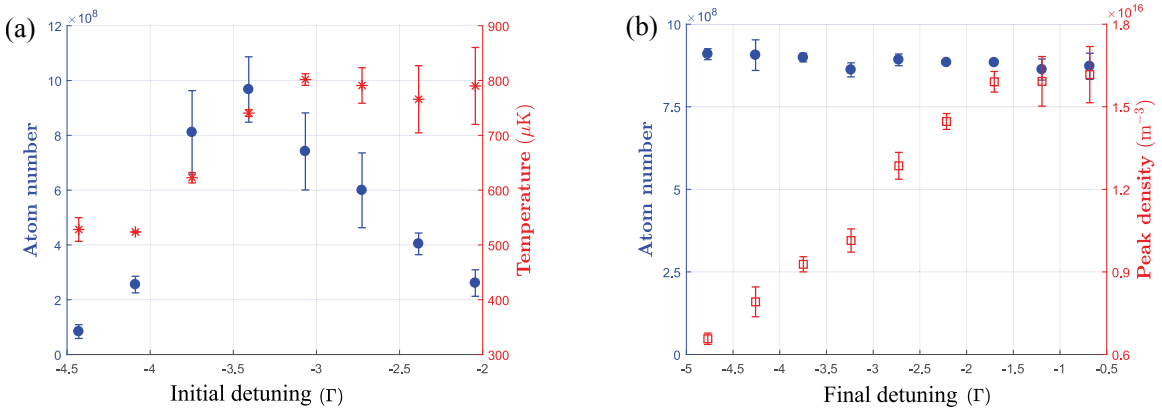

Figure 2.3: Scans on the molasses detunings. (a): Atom number in the MOT cloud versus the initial molasses beam detuning. At detuning $\Delta = -3.4\Gamma$ the most atoms are captured. (b): Atom number by the end of D2 molasses step in the experiment sequence. As final molasses frequency goes toward resonance, the cloud peak density has a rising trend. Reprinted from [91]

2.1.3 D_1 gray molasses cooling

Due to the small hyperfine splitting of ^{6}Li D_2 line, the D_2 molasses does not provide polarization gradient cooling and the cloud temperature remains above the Doppler cooling limit $T_D = \hbar\Gamma/2k_B = 140\,\mu$K. In fact, our cloud after D_2 molasses typically has temperature 800 μK and phase space density (PSD) 5.8×10^{-7}. At this PSD the cloud cannot be effectively loaded into the dipole trap. Therefore an additional cooling step using D_1 gray molasses is necessary.

Working principle

In the past decade, D_1 gray molasses cooling has gained popularity among cold atom experiments using light alkali atoms like K and Li [99, 100, 101, 102]. The cooling is based on polarization gradient and velocity-selective coherent population trapping (VSCPT). Figure 2.4 briefly describes the level diagram and the cooling process — Two counter propagating coherent beams Ω_1 and Ω_2 create a Λ-type coupling among the atomic levels. The two ground states can be projected to new basis $|\Psi_B\rangle$ and $|\Psi_D\rangle$, where the "dark state" $|\Psi_D\rangle$ is unaffected by the light field, but the "bright state" $|\Psi_B\rangle$ depends on the polarization gradient. There is a coupling between the bright and dark state, whose transition probability increases with atom's speed and decreases with the light shift of the bright state. Therefore hot atoms in dark state preferably transfer to the bright state at its potential valleys. After climbing the potential hill, atoms are most likely to be optically pumped at the top of the bright state potential, then decay into the dark state, and the cycle repeats. The equilibrium temperature after cooling is comparable to the depth of the bright state optical potential. A more thorough treatment of the cooling principle can be found in other sources [103, 104].

Cooling efficiency

Figure 2.5 shows the control sequence during D_1 molasses cooling. The D_1 molasses beams are first turned on and held at maximal intensity $20\,I_{\text{sat}}$ for 3 ms while waiting for the magnetic field to be fully compensated. Then beam intensities are decreased gradually in 2 ms, and held at half of their initial intensity for another 1 ms for thermalization. The cooling is very efficient. Figure 2.6 shows how the cloud temperature decreases during the first 3 ms capture time and how it depends on the intensity ramp. By the end of thermalization, a temperature of 50 μK is reached.

The D_1 repumping light is switched off 10 μs before the cooling light in order to depump most atoms to the two Zeeman levels within the $F = 1/2$ manifold, which will participate in the subsequent evaporative cooling. The detuning of the cooling light is also

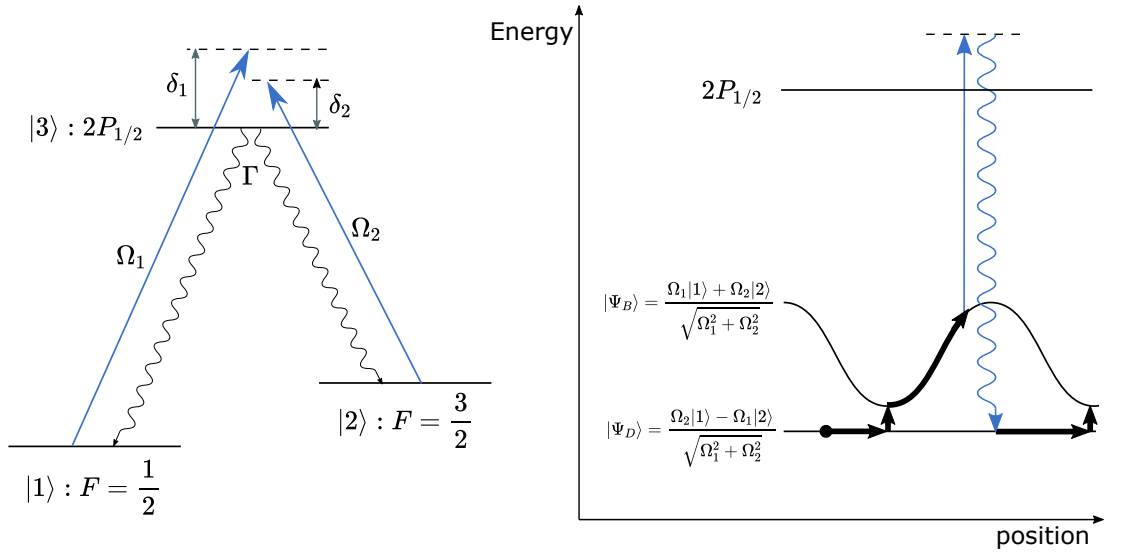

Figure 2.4: *Left*: level diagram of gray molasses cooling on lithium D_1 line. Two beams create a Λ-type coupling between the two ground state and the excited state. *Right*: In the dressed basis of the coupling hamiltonian, Sisyphus cooling happens as the atoms repeatedly climb up the potential hill in the bright state and be transferred back to the dark state.

brought to zero during this depumping time. After the entire gray molasses cooling, we reduce the cloud temperature to 70 μK, while retaining as much as 80% of the atoms from the D_2 cloud, with the peak spatial density exceeding 10^{12}/cm^3.

2.2 Optical transport

The dipole potential experienced by a two-level atom of transition ω_0 from a far-detuned laser of frequency ω and intensity $I(\mathbf{r})$ is given by [105]

$$U_{\text{dip}}(\mathbf{r}) = \frac{3\pi c^2}{2\omega_0^3}\left(\frac{\Gamma}{\omega-\omega_0} - \frac{\Gamma}{\omega+\omega_0}\right) I(\mathbf{r}). \tag{2.2}$$

This form did not use the rotating wave approximation as the detuning can be very large. A simple derivation of the dipole force is given in the appendix A, where rotating wave approximation has been used to arrive at a formula in consistency with the first term here containing $\Delta = \omega - \omega_0$. The conservative dipole force scales as $\frac{I}{\Delta}$ while the photon scattering scales as $\frac{I}{\Delta^2}$. Hence a dipole trap usually combines high intensity with large detuning to reduce heating on the trapped atoms.

When the laser is red-detuned ($\Delta < 0$), atoms will be attracted to the most negative

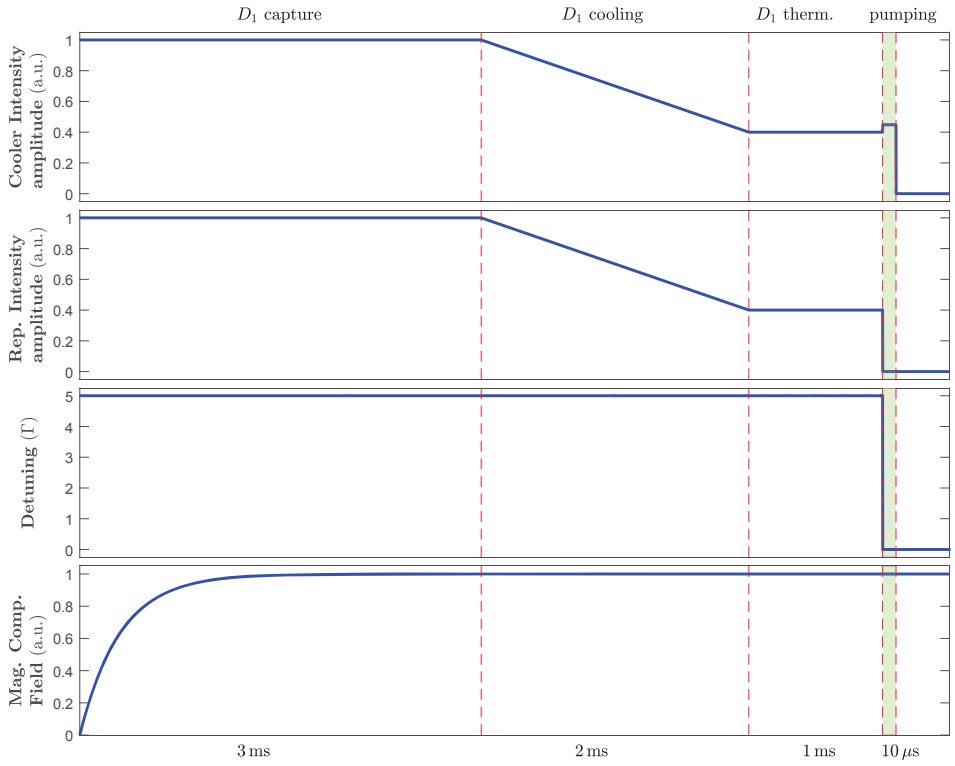

Figure 2.5: Control sequence for the D_1 molasses cooling is separated into three steps: 3 ms capture, 2 ms intensity ramp and 1 ms thermalization. The atoms are depumped to $F = 1/2$ state by switching off the sideband first and zeroing the D_1 molasses detuning. Adapted from [91].

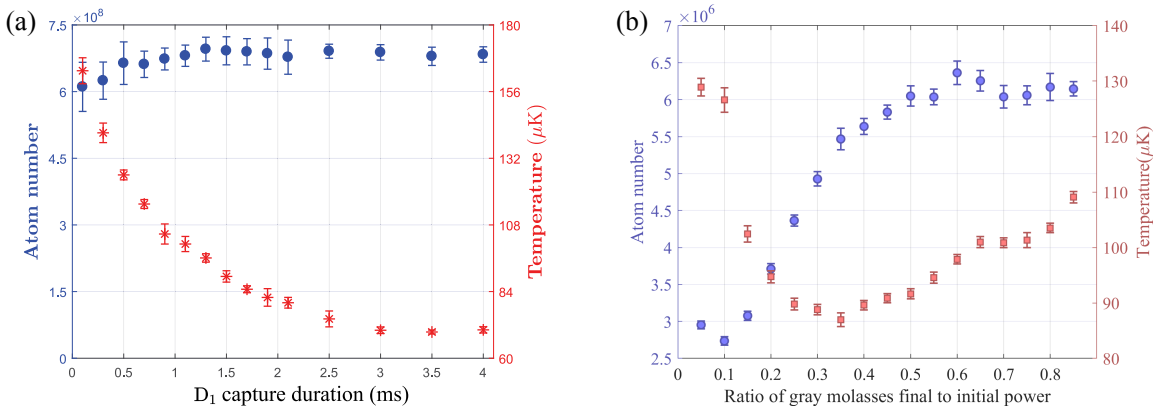

Figure 2.6: Atom number and temperature during D_1 cooling. (a): cloud temperature decreases from 800 μK to 70 μK during the first 3 ms D_1 capture. Reprinted from [91] (b): atom number and temperature dependence on the intensity ramp.

potential where the laser intensity is highest. Hence the beam can serve as an optical tweezer [106] to transport the atom cloud along with its focus position. For a focused Gaussian beam, the spatial variation of its intensity follows

$$I(r,z) = \frac{2P}{\pi w_0^2(1+z^2/z_R^2)} \exp\left[-\frac{2r^2}{w_0^2(1+z^2/z_R^2)}\right], \tag{2.3}$$

where P is the total power and w_0 is the waist. The Rayleigh length $z_R = \dfrac{\pi w_0^2}{\lambda}$ corresponds to the distance along the axial direction where the beam cross-section double in value. The trap depth is

$$U_0 \equiv U(r=0,z=0) = \frac{6c^2\Gamma P}{\omega_0^2(\omega^2-\omega_0^2)w_0^2}. \tag{2.4}$$

Treating the trap as harmonic near its bottom, the trapping frequency along radial and axial directions are respectively

$$\begin{aligned} \omega_r &\equiv \sqrt{\frac{1}{m}\frac{\partial}{\partial r^2}U(r=0,z=0)} = \sqrt{\frac{4U_0}{mw_0^2}} \\ \omega_z &\equiv \sqrt{\frac{1}{m}\frac{\partial}{\partial z^2}U(r=0,z=0)} = \sqrt{\frac{2U_0}{mz_R^2}}. \end{aligned} \tag{2.5}$$

Practically it is more convenient to find the scaling of these trap parameters in terms of laser power and waist. They follow $U_0 \propto P/w_0^2$, $\omega_r \propto \sqrt{P}/w_0^2$ and $\omega_z \propto \sqrt{P}/w_0^3$.

2.2.1 Loading performance

The dipole trap from the 160 W transport beam is turned on during the D_2 molasses stage and remains on throughout the D_1 gray molasses cooling. With 85 μm IPG waist, the trap depth estimated using equation 2.4 is $k_B \cdot 600\,\mu$K, about 12 times the temperature of the D_1 cloud. By holding the IPG with its focus well overlapped with the D_1 cloud, we are able to load up to 8×10^6 atoms into the dipole trap, and $5 \sim 7 \times 10^6$ atoms on a daily basis. Picture 2.7 shows the atoms in the dipole trap shortly after the gray molasses.

Continuously holding the IPG without D_1 cooling induces some heating in the cloud, at an initial heating rate of $16 \pm 3\,\mu$K/s. This heating effect is not a challenge as the transport can be performed within 1.2 s.

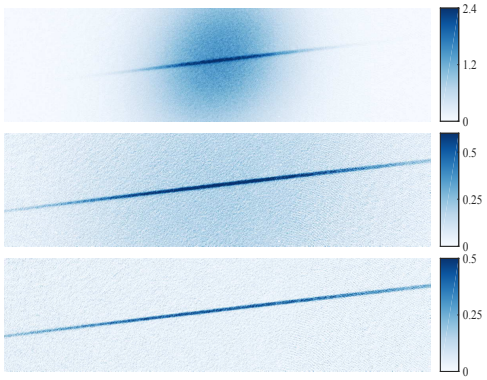

Figure 2.7: atoms loaded into the IPG single beam trap. Pictures show the cloud after turning off the D_1 molasses for 5 ms (top), 15 ms (middle), and 30 ms (bottom).

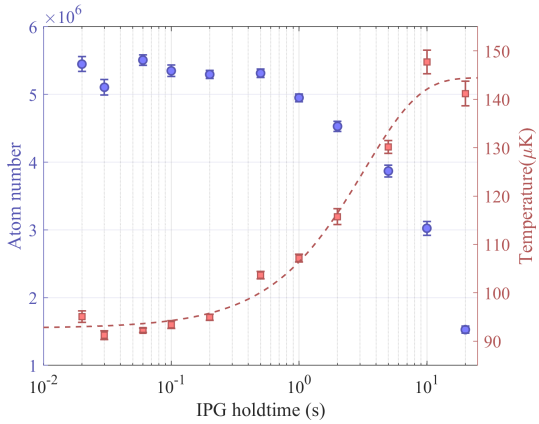

Figure 2.8: Atom number and temperature change while holding in the IPG dipole trap. Within the first few seconds the temperature rise is exponential with a heating rate of $16 \pm 3\,\mu$K/s.

2.2.2 Transport performance

After 100 ms hold in the IPG trap for thermalization, we perform an optical transport by translating the focus position of the IPG laser. The analog control for the stage displacement is programmed as a quartic spline between the initial and final position. This produces a smooth movement with zero final speed, acceleration, or change of acceleration as shown in figure 2.9, and ensures minimal sloshing of the cloud along the axial direction of the trap after transportation. The instantaneous velocity is also kept below the speed limit of the stage.

Since the magnification of the imaging in the science cell and in the MOT chamber are different, the atom numbers from absorption images before and after transport are not directly comparable. Instead, we estimated the efficiency of the transport by doing an forth and back movement, and taking the efficiency as the square root of the remaining atom number over the initial atom number. The efficiency remains above 97% for all transport distances up to 32 cm.

2.3 Preparation for evaporative cooling

To further cool down the atomic gas toward quantum degeneracy, the evaporative cooling technique [107] is used. Evaporative cooling happens when the hottest atoms escape from the trap while the remaining atoms re-thermalize. A continuous cooling to ultra low temperature can be achieved usually in two ways. For optical traps like in our experiment, the

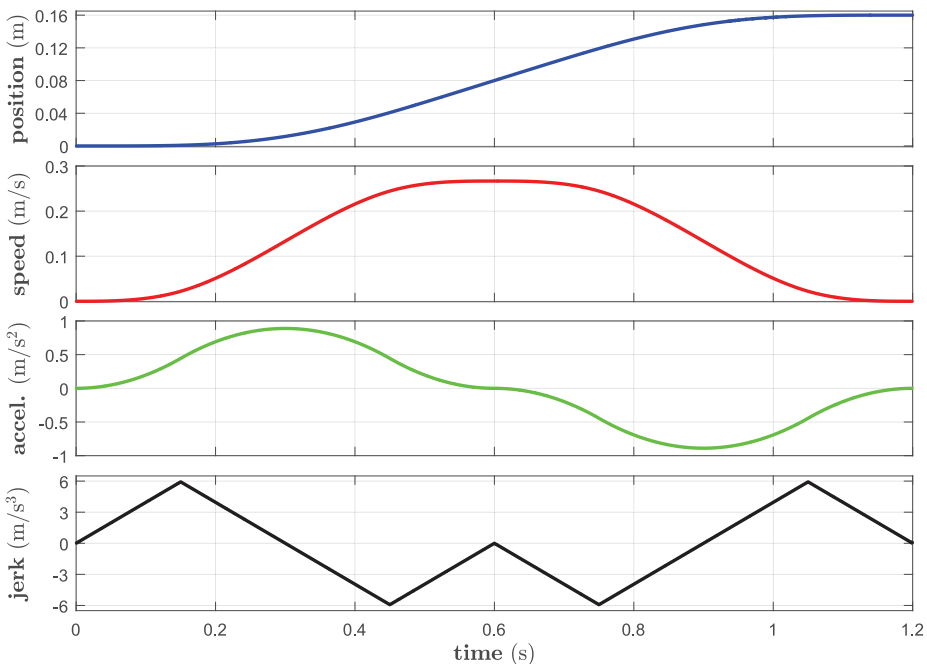

Figure 2.9: From top to bottom, the position, velocity, acceleration and the jerk (derivative of acceleration) of the translation stage.

laser power is ramped down to gradually reduce the trap depth; Alternatively in magnetic traps, RF signals can be used to flip the atom Zeeman state from a trapped one to an anti-trapped one [108, 109]. The cooling is more effective when there is a high elastic collision rate that leads to faster thermalization of the cloud.

Unfortunately, due to the anti-symmetry of two identical fermions' wavefunction, collision between them only allows odd partial waves [110]. Therefore a spin-polarized Fermi cloud in s-wave scattering regime does not thermalize. In order to perform evaporative cooling, the cloud is usually prepared near a Feshbach resonance with equal populations in two different Zeeman states, i.e., spin-balanced. With the strong interaction between the two spin components, evaporative cooling has been proven very effective.

The elastic collision rate inside a harmonic trap for spin-balanced two-species fermions at unitarity can be calculated as [111]

$$\Gamma_{\text{coll}} = \frac{2N\hbar^2\bar{\omega}^3}{\pi(k_B T)^2}, \tag{2.6}$$

where N is the atom number for each spin state and $\bar{\omega} = (\omega_x\omega_y\omega_z)^{1/3}$ is the mean trapping frequency.

2.3.1 Feshbach resonance of ^{6}Li

Feshbach resonance is a useful tool to tune inter-particle interactions on a very broad range in cold atom experiments. In the collision process between two free atoms of different spin states, they can temporarily form closed channel potential containing molecular bound states, whose energy levels can be shifted by applying magnetic fields. A Feshbach resonance occurs when a bound state energy matches the scattering state in the open channel [16], which is near zero for ultra cold atoms. As a weakly bound state disappears, the scattering length diverges and changes its sign from positive to negative. Specifically, the scattering length follows [112]

$$a(B) = a_{\text{bg}} \left(1 - \frac{\Delta_{\text{FB}}}{B - B_0}\right), \tag{2.7}$$

where a_{bg} is the background scattering length, B_0 is the resonance pole of magnetic field B, and Δ_{FB} is the resonance width.

For ^{6}Li, the Zeeman states in $2^2\text{S}_{1/2}$ were shown earlier in figure 1.4, and labeled $|1\rangle$ to $|6\rangle$ from lowest to highest energy. A typical choice of the two spin states are the two lowest states $|1\rangle$ and $|2\rangle$. In figure 2.10 we have plotted pairwise the scattering length between $|1\rangle$, $|2\rangle$ and $|3\rangle$ against the magnetic field. The curves are based on an RF spectroscopy measurement done by G Zürn et al. [113].

2.3.2 Spin population control

By the end of D_1 gray molasses cooling, atoms were depumped to the $F = 1/2$ manifold under a well-cancelled magnetic field. However, after optical transport and the turning on of the Feshbach coils, atoms do not distribute themselves equally to the two Zeeman levels within $F = 1/2$. Instead, the ratio of the atom population ending up in $|1\rangle$ to that ending up in $|2\rangle$ is roughly 6:4. This ratio has also seen drifts on a monthly basis. Without any population control, the spin imbalance becomes worse as we evaporate more, and the minor spin population runs out before we could evaporate to the lowest optical power. Therefore we perform non-adiabatic sweeps using RF pulses between $|1\rangle$ and $|2\rangle$ after optical transport to balance the spin population. The hardware we used include a high precision waveform generator[a], a 5 W RF amplifier[b], and a home-made antenna put close to the science cell with a rough distance 2.5 cm from the antenna loop center to the atoms position.

[a] Rigol DG5252
[b] ZHL-5W-1

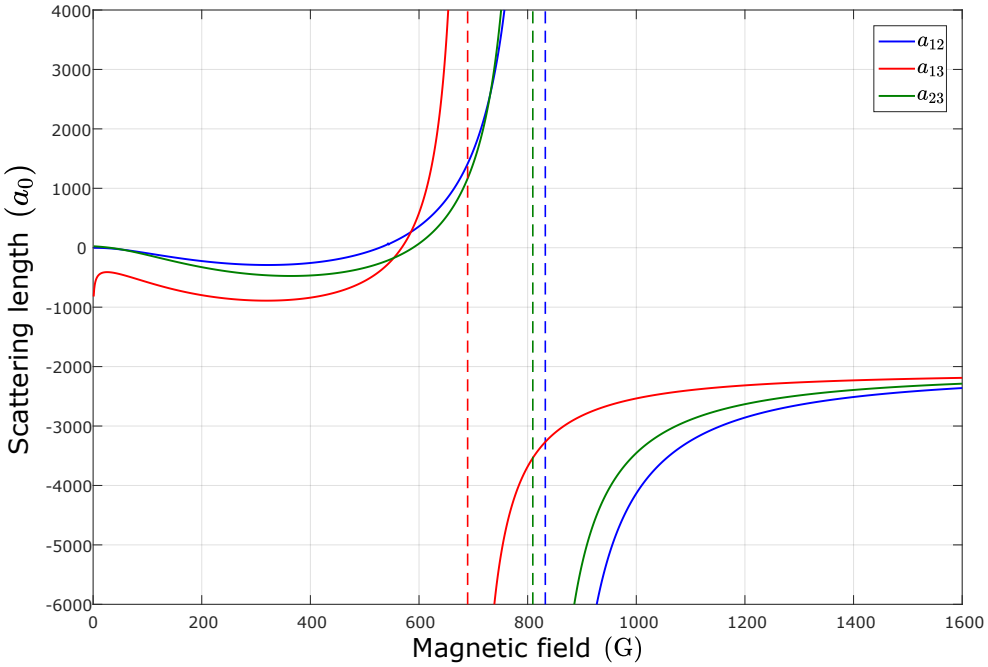

Figure 2.10: Scattering lengths between the lowest three ^{6}Li ground states. The Feshbach resonance for a_{12}, a_{13} and a_{23} are at 832 G, 689 G and 809 G respectively.

Landau-Zener sweep

Suppose the atoms start with a spin polarized population in $|1\rangle$. An adiabatic sweep of a RF signal across the resonance frequency will transfer all the atoms into $|2\rangle$. As the sweeping speed increases, the process is no longer adiabatic and transferred population decreases exponentially according to the Landau-Zener formula [114, 115]

$$P_{|1\rangle\to|2\rangle} = 1 - \exp\left(-\frac{\Omega^2}{4\dot{\Delta}}\right), \tag{2.8}$$

where Ω is the RF Rabi frequency on resonance (in unit of s^{-1}), and $\dot{\Delta} = (\nu_f - \nu_i)/t$ is the sweep speed, given that it is done within t second over the initial and final RF frequency ν_i and ν_f (in unit of Hz). The time constant for this exponential decay, or the sweeping duration at which the exponential becomes -1, can be related to the Rabi frequency by $\Omega^2 = 4(\nu_f - \nu_i)/\tau$.

In order to characterize the sweep speed for best spin balancing, we performed several measurements shown in figure 2.11. Firstly we perform a 20 ms slow sweep with narrow span 40 kHz, and scan the central frequency of this sweep around the RF resonance. This helps locate the resonance frequency to f_c = 76.263 MHz, which is in good agreement with the energy splitting under 832 Gauss from the Breit-Rabi formula 1.1. To estimate the

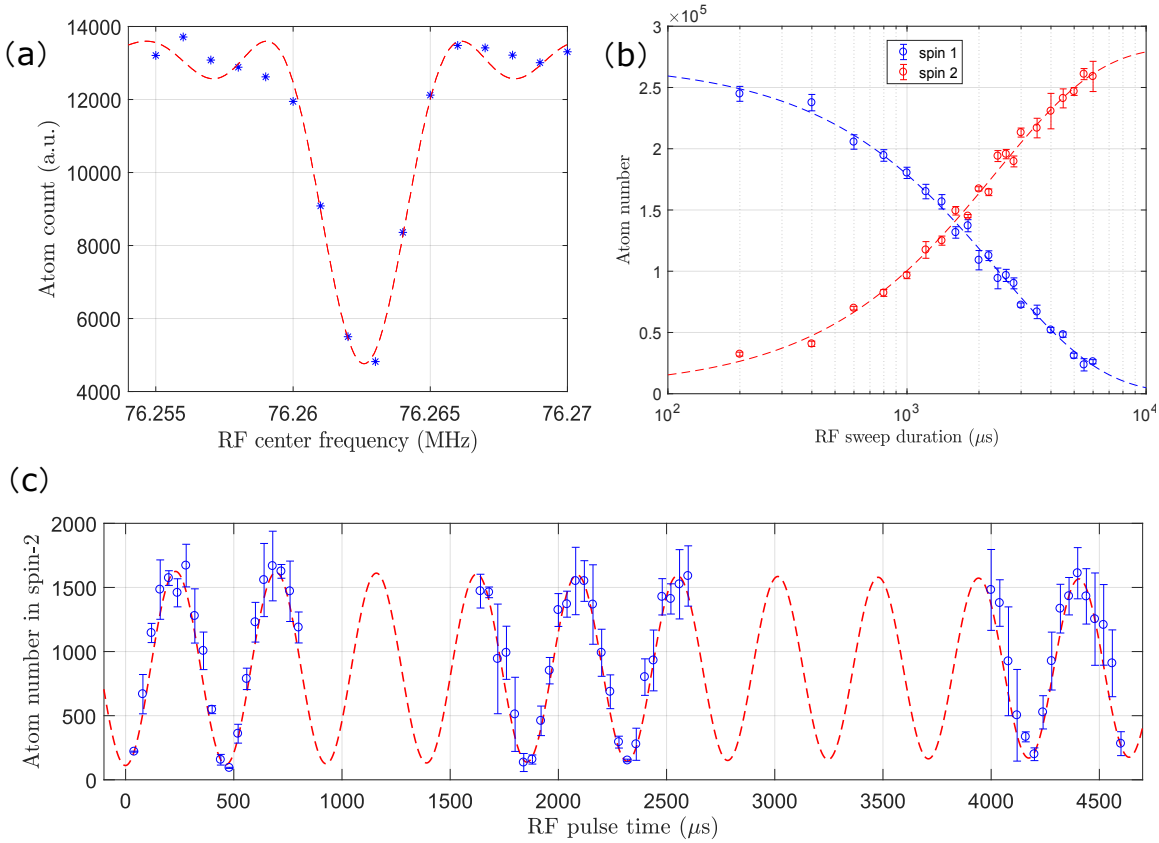

Figure 2.11: (a) A scan on the RF central frequency locates the resonance at 76.263 MHz; (b) Landau-Zener sweep with 100 kHz range for various durations. From population in $|1\rangle$ and $|2\rangle$, the time constants is estimated to be around 2.4 ms; (c) On resonance Rabi oscillation shows Rabi frequency $\Omega \approx 2\pi \times (2.155 \pm 0.009)$ kHz, corresponding to a time constant $\tau = 2.2 \pm 0.02$ ms.

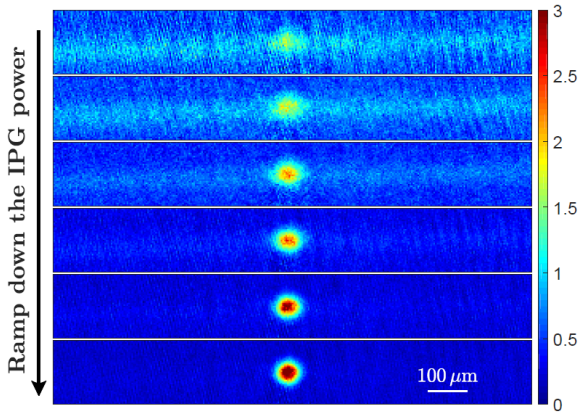

Figure 2.12: After optical transport, the atoms in the IPG transport beam are transferred into the crossed dipole trap. The power of the transport beam is reducing from the top to the bottom pictures. At final IPG power, the wings are no longer visible from the ALS axial direction (a.k.a. the cell transverse imaging direction). Reprinted from [91].

Rabi frequency of the RF transition, we sit on this center frequency and perform a wider sweep from $f_c - 50\,\text{kHz}$ to $f_c + 50\,\text{kHz}$ within various durations. The final population in both $|1\rangle$ and $|2\rangle$ are fitted with the Landau-Zener formula. The fitted time constants are $\tau_1 = 2.42 \pm 0.3\,\text{ms}$ and $\tau_2 = 2.35 \pm 0.3\,\text{ms}$. And at around $1300\,\mu\text{s}$ sweep duration, the two spin population become balanced. Finally a consistency check is done with an on-resonance Rabi oscillation. The measured Rabi frequency is $\Omega = 2\pi \times (2.15 \pm 0.03)\,\text{kHz}$, consistent with the aforementioned time constant.

In the actual experimental sequence, we perform a group of triangular waves, with each rising/falling sweep at the correct speed to balance the spin. We turn on this waveform for around 100 ms or around 40 repetitive non-adiabatic sweeps to achieve an accurate spin balancing. Although it is arguable whether there is enough decoherence time between each single sweep, we have seen this method giving more robust spin balancing result against long term drift of the Rabi frequency, which might come from unstable RF power or mechanical deformation of the antenna.

2.3.3 Loading of the crossed dipole trap

To further increase the collision rate during evaporation, the cross dipole beam (ALS) is sent from the side of the cell to cross with the transport beam (IPG). The transport beam has higher initial power 160 W during the optical transport, and creates a deeper trapping potential than the 15.5 W cross beam. By reducing the transport beam power slowly to 28.5 W, the hotter atoms gradually escape the IPG trap while the coldest fraction gather in the crossed dipole trap (CDT). The final cloud is roughly isotropic in shape. From the cell transverse imaging view, the evolution of the cloud during this process is shown in figure 2.12.

On the final cloud in CDT, we performed a calibration on the trapping frequencies of the transport beam and the cross dipole beam. This helps benchmark the harmonic trap at

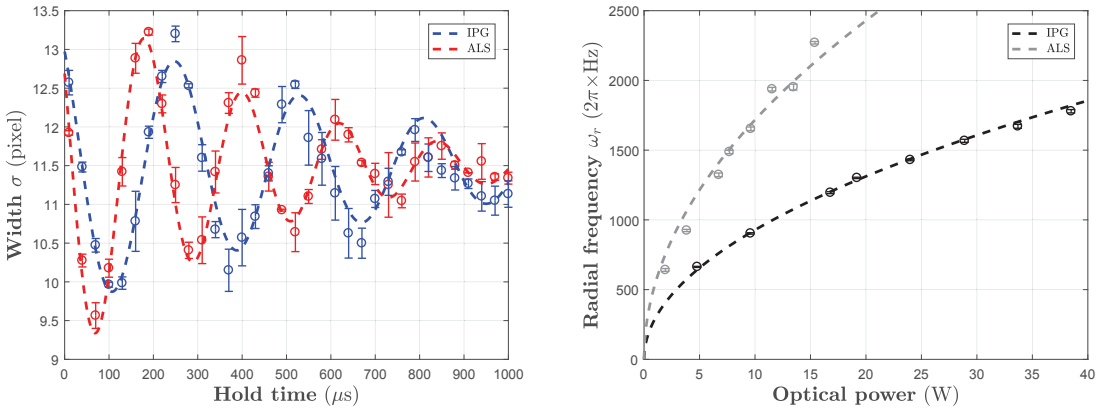

Figure 2.13: *Left*: Breathing mode induced by the temporary release of one laser beam. *Right*: Measured radial trapping frequencies of the two beams as functions of their beam power. Beam waists of the two lasers are confirmed from the fitted curve. Adapted from [91]

later evaporation stages through the scaling of the laser power.

Trapping frequency measurement

The measurement is done by releasing one of the dipole beam for a short period of 50 μs and turn it back on. This induces an oscillation on the cloud width in the crossed dipole trap (CDT). We can extract the radial an axial trapping frequencies from each beam through the breathing mode of these oscillations. The result is shown in figure 2.13. The beam waist of each laser is confirmed[c] from the $\omega \propto \sqrt{P}$ relation. A summary of parameters of the transport beam and the cross beam are listed in table 2.1. By loading the elongated cloud in the transport beam into the crossed dipole trap, we gain two orders of magnitude on the trapping frequency along the transport direction and gain a similar factor on the collision rate, from $520\,\mathrm{s}^{-1}$ to $3.8\times10^4\,\mathrm{s}^{-1}$.

We also performed a measurement on the magnetic trapping frequency within the horizontal plane. This is done inside a single laser dipole trap using the cross beam, with its power reduced to 300 mW. The beam focus is translated axially away from the magnetic center, and the Feshbach coil current is ramped down and back up within 200 ms. This creates an oscillation in the center of mass position of the cloud along the axial direction of the laser beam. The oscillation frequency is the addition between laser axial

[c] A more recent measurement shows slightly lower radial trapping in the transport beam and higher radial trapping in the cross beam comparing to figure 2.13, which was done in 2019. The reported waists and trapping frequencies in table 2.1 follows the latest measurement, therefore contains a small discrepancy to the figure.

	trap depth U_0	radial freq ω_r	axial freq ω_z
transport beam (IPG) $P = 28.5$ W, w_0 =85 μm	170 μK	1710 Hz	11.4 Hz
cross dipole beam (ALS) $P = 15.5$ W, w_0=60 μm	130 μK	2030 Hz	7.3 Hz

Table 2.1: Trapping parameters for IPG and ALS before evaporation.

frequency and magnetic trapping $\omega_{\text{CM}}^2 = \omega_{z,\text{ALS}}^2 + \omega_{\text{mag}}^2$. Subtracting the known laser axial trapping frequency, we measured a magnetic trapping frequency of $2\pi \times 10.3$ Hz at 240 A Feshbach current, corresponding to 0.0164 G/cm^2/A magnetic curvature in the horizontal plane. Therefore the anti-trapping in the vertical direction is twice this value, as reported in table 1.1

Summary on the cooling until CDT

Phase space density (PSD) is defined as $\mathcal{D} = n\lambda_{\text{dB}}^3$ and is a good indication on how significant the quantum effects are as its value approaches 1. For atom cloud in a harmonic trap, the atom density over the whole trap can be integrated to obtain an alternative expression for the PSD:

$$\mathcal{D} = N \left(\frac{\hbar\bar{\omega}}{k_B T} \right)^3 \tag{2.9}$$

Table 2.2 summarizes the atom number, temperature and PSD during all cooling steps until loading into the crossed dipole trap.

Cooling stage	Atom number	Temperature	PSD	collision rate
cMOT	$\sim 1 \times 10^9$	1.2 mK	5.5×10^{-7}	—
D_2 molasses	$\sim 1 \times 10^9$	800 μK	5.8×10^{-7}	—
D_1 molasses	$\sim 7 \times 10^8$	50 μK	5.2×10^{-5}	—
dipole trap before transport	$\sim 5 \times 10^6$	90 μK	3.4×10^{-4}	—
transported DT after RF scan	2×10^6 per spin	125 μK	5.0×10^{-5}	520 s^{-1}
crossed dipole trap	3.4×10^5 per spin	23 μK	2.0×10^{-2}	3.8×10^4 s^{-1}

Table 2.2: Atom number, temperature and phase space density of the atom cloud at each previous cooling step.

CHAPTER 3
REACHING SUPERFLUIDITY

In this chapter we report the cooling performance and the evidence for reaching superfluidity of the fermionic cloud. The prepared cloud in our setup is more dilute compared to other experiments studying lattice physics [116, 117, 118], yet our setup has been able to cool them to a lowest temperature of 15 nK, which is sufficient to study interesting phenomena across the superfluid transition. The relatively low atom density makes sure that the pinning lattice (chapter 5) can preserve the spatial distribution of the cloud well, with less escaping events. This is essential for the quality of the microscopic image (chapter 4).

3.1 Evaporation sequence

3.1.1 Power ramp

Our evaporative cooling is carried out in several steps, where the dipole trap depth is reduced at different rates. The choice of the duration and power ramp at each step is purely empirical. Figure 3.1 shows the power ramp curves. The timeline in the figure starts at the end of the optical transport. The atom cloud starts being elongated in the deeper trap of the transport IPG beam. In evaporation step 1, as mentioned before in section 2.3.3, the transport beam power is reduced to gradually gather the atoms into the crossed dipole trap (CDT). In the next two steps, the power of both beams are reduced simultaneously until a trap depth of around 15 μK, before the transport beam switches off. The following steps of the evaporation happen in the cross beam alone, with the axial trapping mainly provided by the magnetic curvature. The reason that we do not keep both beams until the end is the lack of regulation on the transport beam power at lower values. Nevertheless, this practical limitation does not hinder us since low spatial densities are actually favorable for the pinning and the fluorescence imaging. More explanations will be given in chapter 4.

3.1.2 Evaporation efficiency in the crossed dipole trap

The evaporation efficiency can be reflected from the change in the atom number, trap characteristics and the cloud temperature throughout the evaporation process. Based on the typical performance of our evaporation, during evaporation step 2 and step 3, the temperature has been cooled down to one third while there is only around 20% loss in the atom

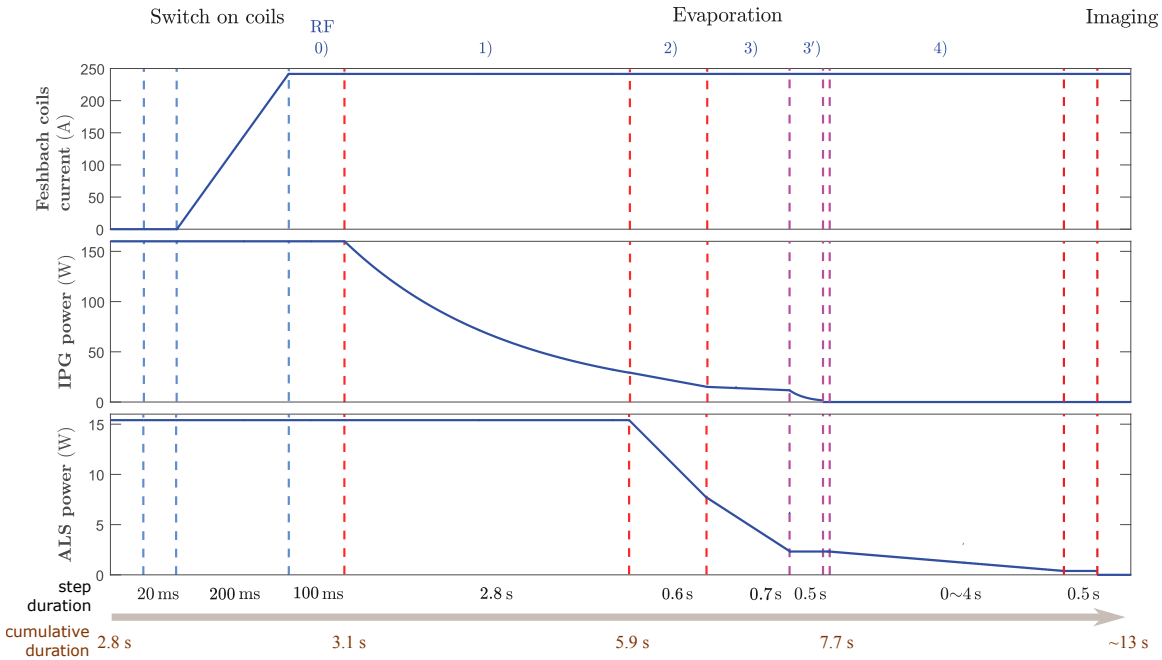

Figure 3.1: The power ramp during evaporative cooling: In evaporation step 0), the cloud is held in IPG dipole trap for 200 ms of magnetic field turn-on and 100 ms of spin-balancing RF sweep. In step 1), the IPG power is reduced exponentially from 160 W to 28.5 W and the cloud is transferred fully into the crossed dipole trap. In step 2) and 3), both beam powers are ramped down linearly to 40% and then to 12% of its starting value. Finally, the IPG is switched off in 0.5 s and the ALS power ramped down to tens of mW during step 4). The evaporation and imaging is done at 832 Gauss magnetic field. The total sequence time starting from the MOT loading to reaching superfluidity is within 13 s.

number. Between step 3 and step 4 when the IPG laser is switched off, the evaporation continues and cools the cloud temperature down by a half without significant loss in atom number. Although we lose a factor of 30 in phase space density due to the cloud spreading out along the ALS axial direction, subsequent cooling in the cross beam alone is very efficient, and the PSD quickly approaches back toward 1. To give a quantitative measure on the performance in this final step of evaporation, the evaporation efficiency defined as

$$\gamma = \left| \frac{\ln(\mathcal{D}_{\text{fin}}/\mathcal{D}_{\text{ini}})}{\ln(N_{\text{fin}}/N_{\text{ini}})} \right| \tag{3.1}$$

remains above 4.5 between the start of evap 4 to the endpoints of various trap depths.

3.2 Thermometry in axial-symmetric harmonic trap

Local density approximation (LDA)

In the literature on trapped ultracold Fermions, there are two frequently used conventions to report the reduced temperature T/T_F, depending on whether it refers to a trap average or to the local value at the center of the trap. Under the local density approximation (LDA), the Fermi energy is related to the local density according to equation B.2:

$$\varepsilon_F(\mathbf{r}) = \frac{\hbar^2}{2m}(6\pi^2 n(\mathbf{r}))^{\frac{2}{3}}, \tag{3.2}$$

where $n(\mathbf{r})$ depends on the local chemical potential $\mu(\mathbf{r}) = \mu_0 - V(\mathbf{r})$, with μ_0 the chemical potential at the trap center and $V(\mathbf{r})$ the trap potential. To access the difference between these two definitions, it is instructive to look at the non-interacting case where analytical results exist.

Using the equation of state (EoS) for atom number density for a non-interacting Fermi gas (see appendix B), we can define a local T/T_F

$$\left.\frac{T}{T_F}\right|_{\text{LDA}} = \frac{4}{\left(-6\sqrt{\pi}\text{Li}_{3/2}(-e^{\beta\mu})\right)^{2/3}}. \tag{3.3}$$

On another hand, integrating over the whole cloud, the total atom number is

$$N = \frac{1}{6}\left(\frac{E_F}{\hbar\bar{\omega}}\right)^3, \tag{3.4}$$

where E_F is the Fermi energy at the trap center. Under the Thomas-Fermi approxima-

tion, where the thermal energy of the cloud is assumed to be larger than the energy level spacings in the trap, one also has [119] $N = -\left(\frac{k_B T}{\hbar\bar{\omega}}\right)^3 \mathrm{Li}_3(-e^{\beta\mu})$. Combining both relations, one can define a T/T_F averaged over the whole harmonic trap

$$\left.\frac{T}{T_F}\right|_{\mathrm{HO}} = \left[-6\mathrm{Li}_3(-e^{\beta\mu})\right]^{1/3}. \tag{3.5}$$

The polylogarithm function $\mathrm{Li}_n(z)$ follows the definition in appendix B.

Mixing the trap-averaged value or the local value of T/T_F could give very misleading estimates on the degree of degeneracy of the cloud, as their values deviate very fast with increasing temperature, as shown in figure 3.2. In our experiment, it is meaningful to keep track on the local thermodynamic properties of the cloud, hence we will stick to the local T/T_F in this thesis unless otherwise specified.

3.2.1 Thermometry using the Equation of State

As we further reduce the ALS beam power and cool toward quantum degeneracy, the time-of-flight (TOF) method for temperature measurement loses validity. On one hand, this is because the expansion of the cloud changes from ballistic to hydrodynamic [120]. On the other hand, what TOF measures is the internal energy of the cloud, which includes strong interactions apart from the kinetic energy, which is what we want to measure to access the temperature. Instead, we adopt a thermometry based on doubly-integrated density profile of the cloud in a axial-symmetric harmonic trap [50]. From such 1D density profiles one can directly extract the equation of state (EoS) on the local pressure [121].

This extraction can be performed by considering the chemical potential, which varies with the position inside a harmonic trap as:

$$\mu(r,z) = \mu_0 - \frac{1}{2}m\omega_r^2 r^2 - \frac{1}{2}m\omega_z^2 z^2. \tag{3.6}$$

From the Gibbs-Duhem relation, the 3D density can be expressed as $n(\mathbf{r}) = \left(\frac{\partial P(\mathbf{r})}{\partial \mu(\mathbf{r})}\right)_T$. Subsequently, the 1D doubly-integrated profile along the trap axial direction is

$$\begin{aligned} n^{1\mathrm{D}}(z) &= 2\pi \int_0^\infty n(\mathbf{r}) r dr = -\frac{2\pi}{m\omega_r^2} \int_{\mu(r=0,z)}^{-\infty} \left(\frac{\partial P}{\partial \mu}\right)_T d\mu \\ &= \frac{2\pi}{m\omega_r^2} P(T, \mu(z)). \end{aligned} \tag{3.7}$$

This result shows that one density profile in the harmonic trap bears the information

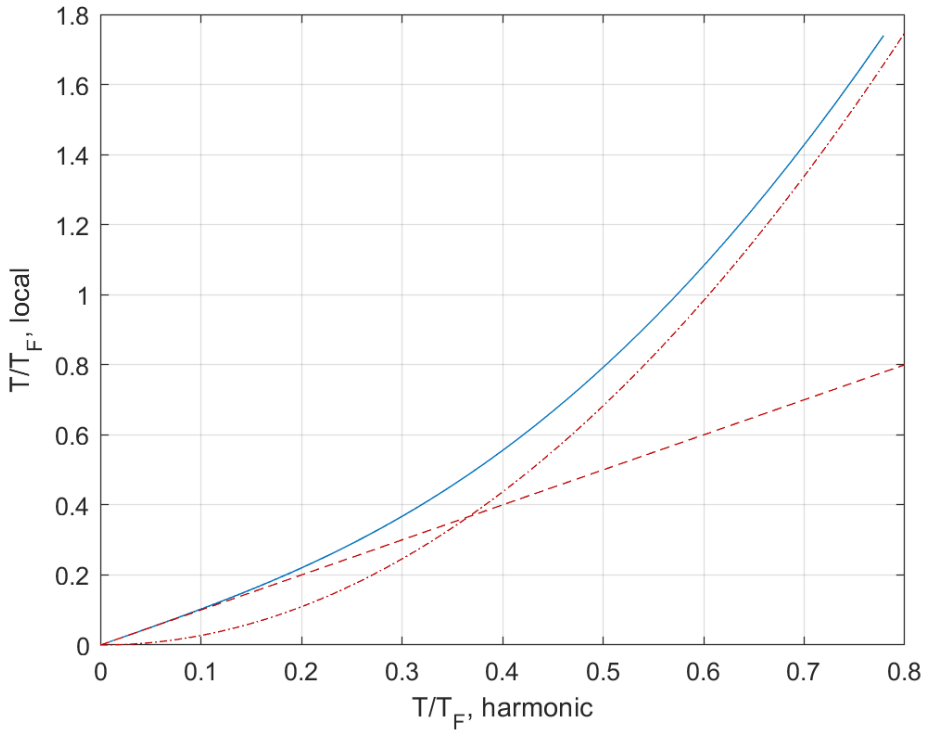

Figure 3.2: Comparing the local reduced temperature $\left.\frac{T}{T_F}\right|_{\text{LDA}}$ to the trap-averaged value $\left.\frac{T}{T_F}\right|_{\text{HO}}$. The blue curve shows that the trap-averaged value becomes much smaller than the local T/T_F at trap center as temperature goes up. The asysmptotic behaviors are shown by the red dotted lines. For very low temperature, the two definitions become equal, whereas for high temperature, $\left.\frac{T}{T_F}\right|_{\text{LDA}} \approx \frac{4}{\pi^{\frac{1}{3}}}\left(\left.\frac{T}{T_F}\right|_{\text{HO}}\right)^2$.

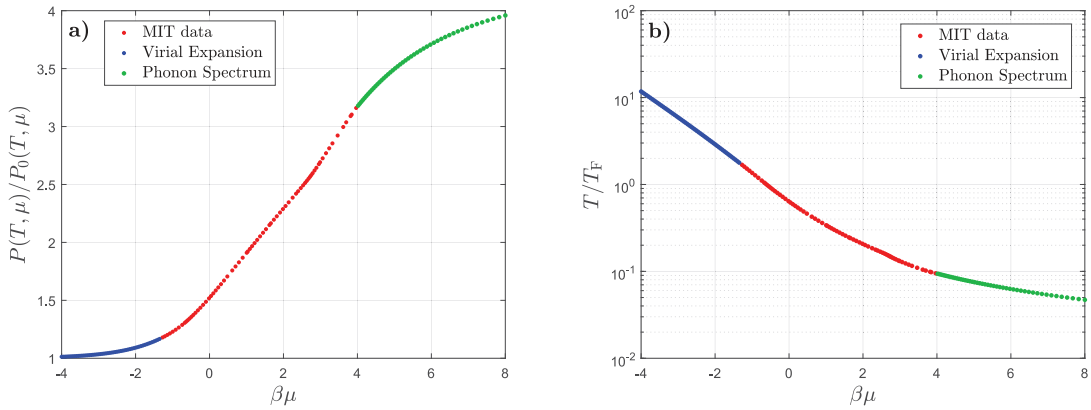

Figure 3.3: Mapping between $\beta\mu$ and (a) the correction function $\psi = P/P_0$ as well as (b) local T/T_F. In both pictures, green points are from Virial expansion until third order under high temperature limit, red points are experiment data from MIT, blue points are from excitation spectrum under low temperature limit.

of the pressure EoS at all different μ. From known asymptotic forms and previous experimental measurements [50, 51] on the EoS, as well as a precise characterization of the trap frequencies, one can fit for the two thermodynamic variables T and $\beta\mu$. Here the product $\beta\mu$ is used as a variable over μ to simplify expressions, since the EoS for pressure (per spin) of a spin-balanced unitary Fermi gas is

$$n^{1D}(z) = \frac{1}{\lambda_{dB}} \frac{2\pi k_B T}{m\omega_x\omega_y} \left[-\mathrm{Li}_{5/2}\left(-e^{\beta\mu(z)}\right)\right] \times \psi[\beta\mu(z)], \tag{3.8}$$

which is the pressure for ideal Fermi gas multiplied by a "correction function" only depending on $\beta\mu$. In addition, knowing a relation between T/T_F and $\beta\mu$ (equation B.7), the Fermi energy ε_F can easily be deduced from the fit result also.

Figure 3.3 shows $\psi = P/P_0$ and T/T_F as functions of $\beta\mu$. These curves are obtained by concatenating segments in different temperature ranges. In the high temperature limit, Virial expansion up to the third Virial coefficient is used; When $T \ll T_F$ limit, excitation energy of the Bogoliubov-Anderson phonons and quasi-particles is used to obtain the required thermodynamic relations; For intermediate temperature, we take the data from the experimentally measured EoS at MIT [51]. Some more details on the asymptotic expressions are described in appendix B.

3.2.2 Temperature fit results

Using the above mentioned fitting method based on the EoS, we analyze the evaporation results after extending our evaporation step 4 to lower trapping depths. As mentioned in

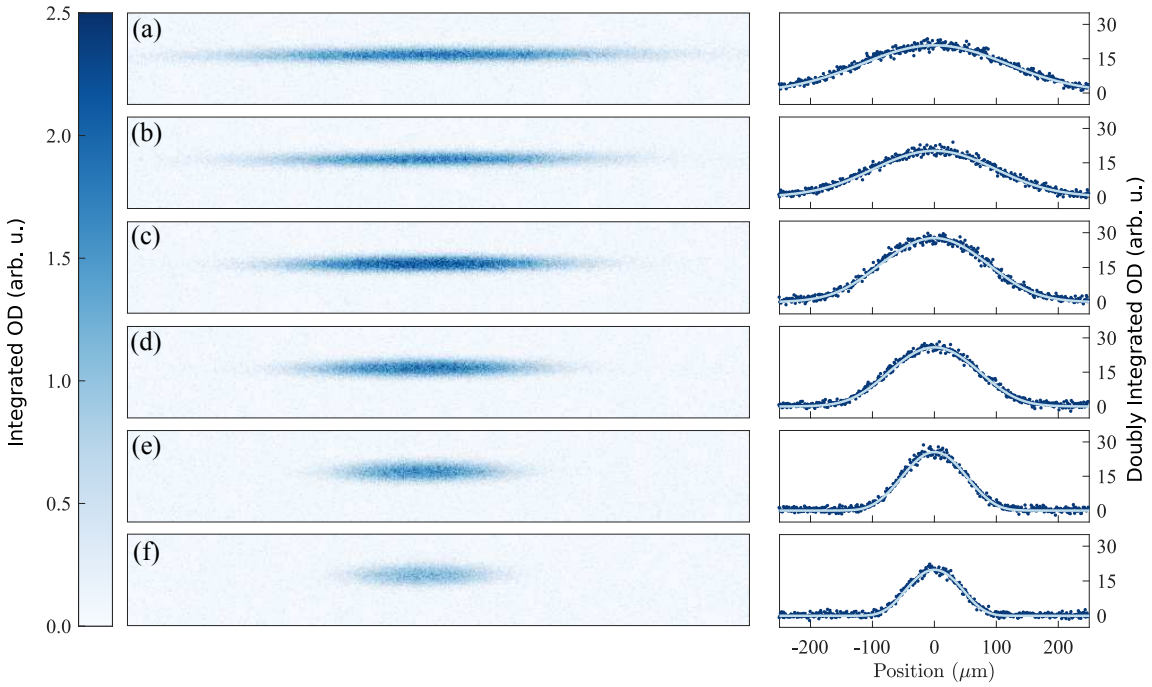

Figure 3.4: Cloud of one spin in the dipole trap of the ALS beam for various beam powers: (a) P = 300 mW; (b) P = 200 mW; (c) P = 125 mW; (d) P = 75 mW; (e) P = 30 mW; (f) P = 20 mW. The column on the right shows the corresponding 1D doubly integrated density profile (blue dots) and the fitting curve (light blue curve). The fitted temperatures are $T = \{0.66(2), 0.48(2), 0.29(1), 0.21(1), 0.099(7), 0.08(1)\}T_F$.

the earlier section 3.1, the last stage of evaporation is finished in the single cross dipole beam. The trapping frequency is the composite between the laser trapping, which follows the calibration in section 2.3.3, and a 10.3 Hz magnetic trapping in the horizontal plane. After evaporating to various optical trap depths, the local T/T_F at the trap center are extracted from the density profile of the cloud. The result is shown in figure 3.4. With lowest regulated power 17 mW of the dipole trap laser, our evaporation reaches a final temperature of 17 nK and $T/T_F = 0.076 \pm 0.013$, with about 5×10^4 atoms per spin state. This is well below the known superfluid transition temperature $T_c/T_F = 0.176$ [51]. An independent evidence of the presence of superfluid will be shown in the following section 3.3. Figure 3.5(a) and (b) summarizes the temperature, atom number and phase space density over the final evaporation process.

Total internal energy vs. kinetic energy

As mentioned earlier, the temperature measured from expansion of the cloud deviates from the real temperature as it is cooled down. However, based on the TOF measurement, one

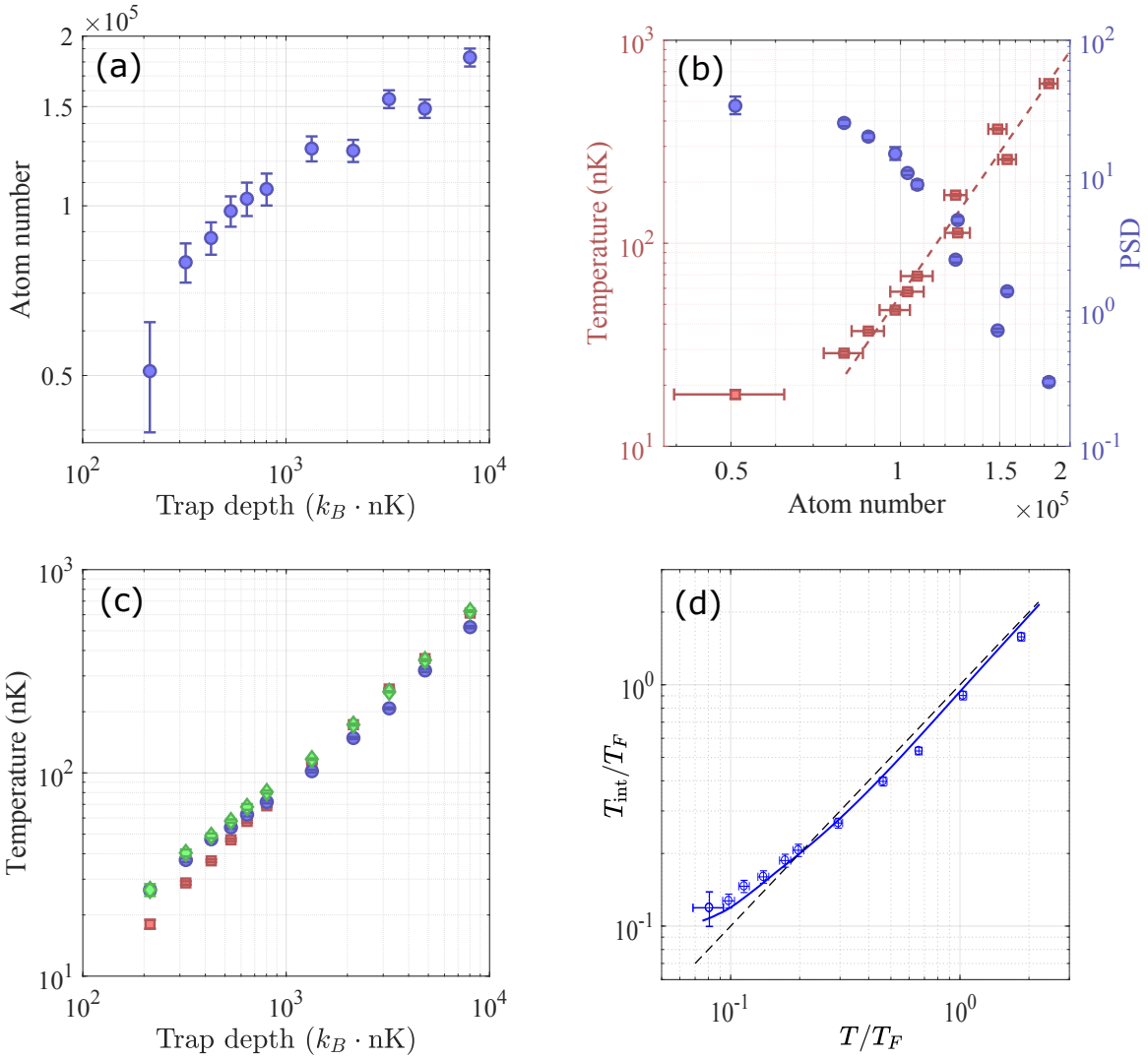

Figure 3.5: (a) Atom number against trap depth in the course of the evaporation. (b) Temperature and phase space density (PSD) as a function of atom number. Red dashed line follows $\ln(T) \simeq 4\ln(N) + b$. (c) Temperature change throughout the evaporation process. Thermometry using the EoS fit gives a measurement on temperature T (red squares); Hydrodynamic expansions from TOF measurements gives an estimate on the internal energy $T_{\rm TOF} = T_{\rm int}$ (blue circles). A naïve fit of TOF measurements with a ballistic expansion is also shown (green squares). (d) Comparing $T_{\rm int}/T_F$ to T/T_F, which is expected to follow the numeric solution for a unitary gas in 3D harmonic trap (solid blue line). Adapted from [122]

can still obtain meaningful information. In fact, according to the Virial theorem, for both non-interacting and unitary Fermi gas in harmonic trap, the internal energy equals to the trapping potential energy [123]. Therefore, knowing the trapping frequency $\omega_\perp$ and the fitted in-trap cloud size σ_0, the TOF temperature directly reflects the internal energy, which includes both the kinetic energy and the interactions:

$$T_{\text{TOF}} = T_{\text{int}} = \frac{m\omega_\perp^2\sigma_0^2}{k_B} = \frac{E_{\text{int}}}{\frac{3}{2}Nk_B}. \tag{3.9}$$

In figure 3.5(c), the real temperature from EoS fit (red squares) is compared to the TOF temperature or the "internal temperature" (blue circles). The deviation becomes obvious below 100 nK. For the unitary Fermi gas in our experiment, the expected behaviour of

$$\frac{T_{\text{int}}}{T_F} = \frac{E_{\text{int}}}{\frac{3}{2}NE_F} = \frac{P}{nE_F}$$

is solved numerically after averaging over the 3D harmonic trap. It shows a reasonable agreement with our TOF measurement in subfigure (d). A noticeable feature of this curve is that at very low T/T_F, the internal energy is dominated by Fermi pressure, and will tend to a constant instead of zero.

Notice that the in-trap cloud size σ_0 in equation 3.2.2 is determined by fitting the cloud size against TOF based on a hydrodynamic expansion. If naive ballistic expansion is used, another set of "temperature" data T' is obtained (green diamonds). For thermal cloud at high T/T_F, the naive ballistic fit of the temperature agrees with the EoS fit, and is larger than the internal temperature T_{int}, due to the negative contribution of interaction in the unitary gas.

3.3 A unitary Fermi superfluid

In 1938, bosonic superfluidity was first seen by two groups [124, 125] simultaneously on liquid ^{4}He. A phase transition is recorded at $\sim$2.17 K below which "type I helium" with zero viscosity appears. This behaviour was soon related to the Bose-Einstein condensation of bosonic ^{4}He [126, 127, 128]. For fermionic systems, the transition happens at much lower temperatures compared to the degeneracy temperature. Even though lab observation of Mercury superconductivity has been done as early as in 1911 by Dutch physicist Heike Kamerlingh Onnes, the understanding of superfluidity/superconductivity came much later with the BCS theory [20], which explains the pairing of fermionic atoms. Subsequently,

Leggett showed that the superfluid of losely bond Cooper pairs and BEC made by tightly bound molecules can be viewed in a unified way through the "BCS-BEC crossover" — They can smoothly evolve into each other as the pair size changes with respect to the interparticle distance [129].

In the crossover regime, the strongly-interacting Fermi gas system resembles high-T_c materials in the sense that the correlation length or the "pair size" is comparable to the interparticle distance. The superfluid transition temperature here in units of Fermi temperature is also higher than any other conventional fermionic system. Thermometry described above suggests that we have cooled the Fermi cloud below its superfluid critical temperature $0.176\,T_F$, therefore have obtained a superfluid of ^{6}Li. Direct observation of fermionic superfluidity is not trivial as the phase transition is not directly reflected on the cloud density profile [130], unlike in the Bose-Einstein condensation. Nonetheless, there are various experimental techniques that have been used as good indicators.

Excited vortices

Observation of vortex arrays is the most direct evidence for superfluidity. Through stirring, a non-zero curl is introduced in the velocity field of the fermionic cloud. For fermions in superfluid phase, this curl can only be carried by evenly distributed, quantized vortices. In MIT, clear observation of vortices has been shown on ^{6}Li [49]. However, since the stirring requires extra laser beams and subtle control over the motion of their foci, we did not apply this method to check whether we are creating superfluid samples.

Rapid ramp and double structure

The rapid ramp technique provides another possible indication for superfluidity. It was first developed in the JILA group [131] on ^{40}K and adapted on ^{6}Li by the MIT group [132]. By performing a magnetic field ramp from BCS to BEC side that is fast enough to preserve the momentum distribution, Cooper pairs are mapped to condensates in the molecular BEC, and can show up as a double structure in the density profile. However, the connection between superfluidity and the double structure is not trivial as it depends on the ramp parameters and for typical conditions, the condensate fraction is not conserved during the field ramp.

Superfluid plateau

Observation of a superfluid plateau for a spin-imbalanced Fermi gas is yet another way to confirm superfluidity, and can be readily tried out using our setup with a weakly spin-

polarized cloud. The superfluid plateau is a flat region in the 1D double integrated profile of the density difference between the majority and the minority Fermion species. It reflects the phase transition from pure superfluid to normal liquid when the chemical potential difference between the two spins increases to the Clogston Chandrasekhar limit [90], and a sudden jump on the local density of the minority spin $|\downarrow\rangle$ is seen. At unitarity, $\frac{n_\downarrow}{n_\uparrow} = 0.44$ at the phase separation [133]. If the cloud is trapped in a harmonic potential, it is more convenient to quantify the spin imbalance by the polarization $P = \frac{N_\uparrow - N_\downarrow}{N_\uparrow + N_\downarrow}$. There is a critical polarization above which superfluid pairing does not happen throughout the whole trap, and it is reported [133, 134] to be $P_c = 77\%$. For $0 < P < P_c$, superfluid will exist and the cloud will consists of three concentric shells of different phases:

- A fully paired superfluid core with $n_\uparrow = n_\downarrow$, where vortices can be generated [135].

- A partially polarized non-superfluid phase with $n_\uparrow > n_\downarrow$. The densities (especially for the minority spin) are discontinuous at the separation with the inner core.

- A fully polarized phase where only the majority spin exist and obeys the ideal Fermi gas laws. The densities changes continuously from the middle shell to the outermost shell.

Assuming that the length of the superfluid core is l along the major axis z, by equation 3.7, the 1D doubly integrated profile difference remains constant over l:

$$\left.\frac{\partial(n_\uparrow^{\mathrm{1D}} - n_\downarrow^{\mathrm{1D}})}{\partial z}\right|_{|z|<\frac{l}{2}} = -\frac{\omega_z^2}{\omega_r^2}\cdot 2\pi z \left.\frac{\partial(P_\uparrow - P_\downarrow)}{\partial \mu}\right|_{r=0,|z|<\frac{l}{2}} = 0. \tag{3.10}$$

Figure 3.6 shows the absorption images of the two spins, and the subtracted profiles. A plateau can be clearly seen over the 200 μm range in the middle of the cloud. The two absorption images are taken at high field using double-exposure mode on the camera and a fast switch on the imaging beam frequency. Each exposure is 7 μs long, and the two exposures are separated by 3 μs. This small delay between the two exposures guarantee that the density profile of the later-imaged spin component will not be modified by the photon kicks on the firstly-imaged spin. As a simple estimate, the collision rate between opposite spins is (by equation 2.6 and 3.4)

$$\Gamma_{\text{coll}} = \frac{1}{3\pi}\left(\frac{T_F}{T}\right)^2 \frac{E_F}{\hbar}.$$

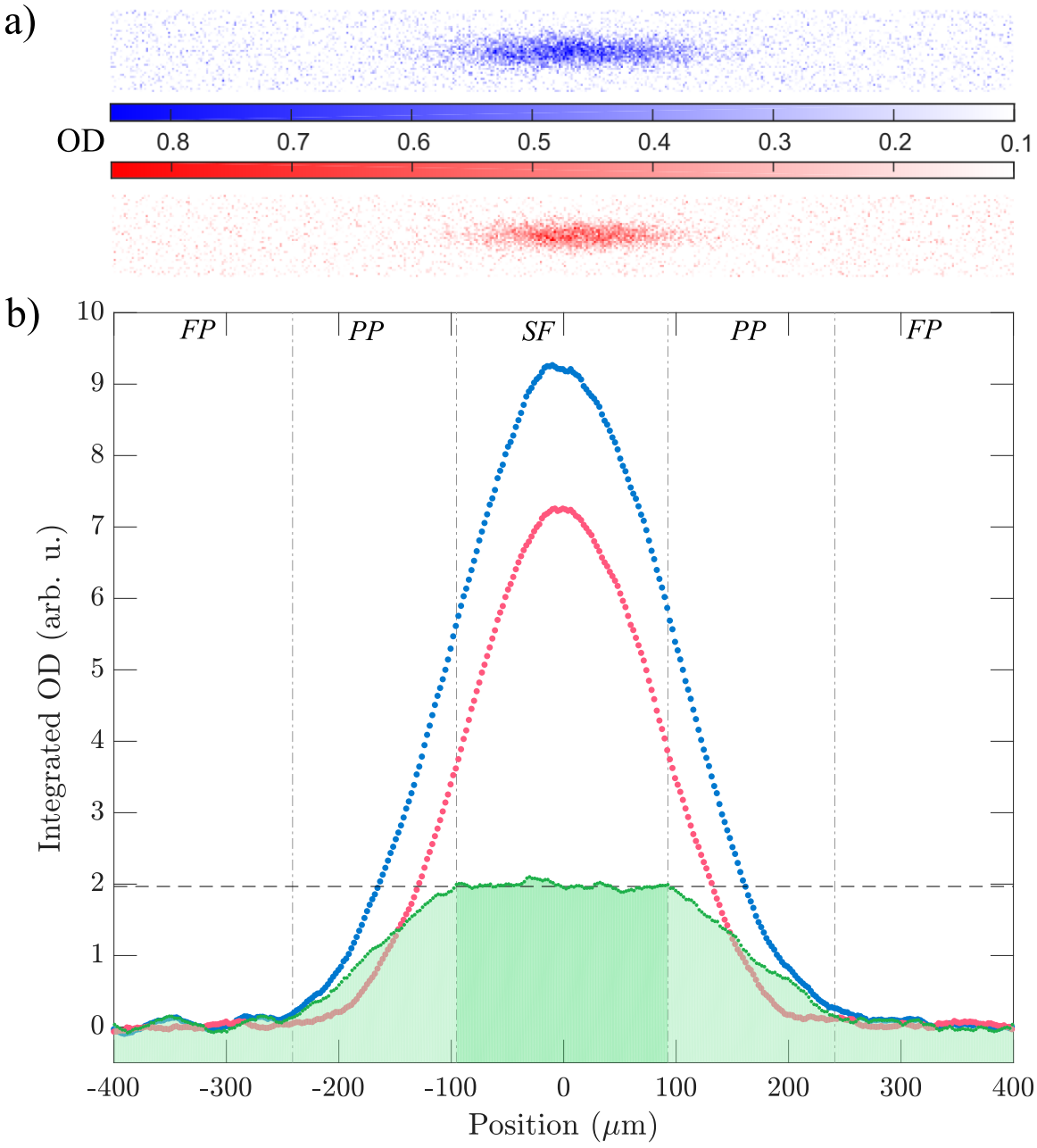

Figure 3.6: (a) Absorption images of the majority (blue OD) and the minority (red OD) spin components. (b)1D integrated profile of the majority spin (blue dots), the minority spin (red dots) and their OD difference (green dots). Savitzky-Golay filter of order 3 and frame length 29 has been applied to both density profiles to smoothen out the fringes originated from the imaging light. The vertical dotted lines mark the different phases. *SF*: superfluid, *PP*: partially polarized, *FP*: fully polarized.

For the series of final cloud temperature shown in figure 3.4, the inverse of the collision rate ranges from 80 μs to 2 μs. Therefore the double-exposure would already be completed before thermalization.

The combination of thermometry and the observation of the plateau in the density difference $n_\uparrow - n_\downarrow$ for a spin-imbalanced Fermi gas show that we are indeed able to produce unitary superfluid sample with a high degree of diluteness, which is a key step to perform single atom imaging.

Part II

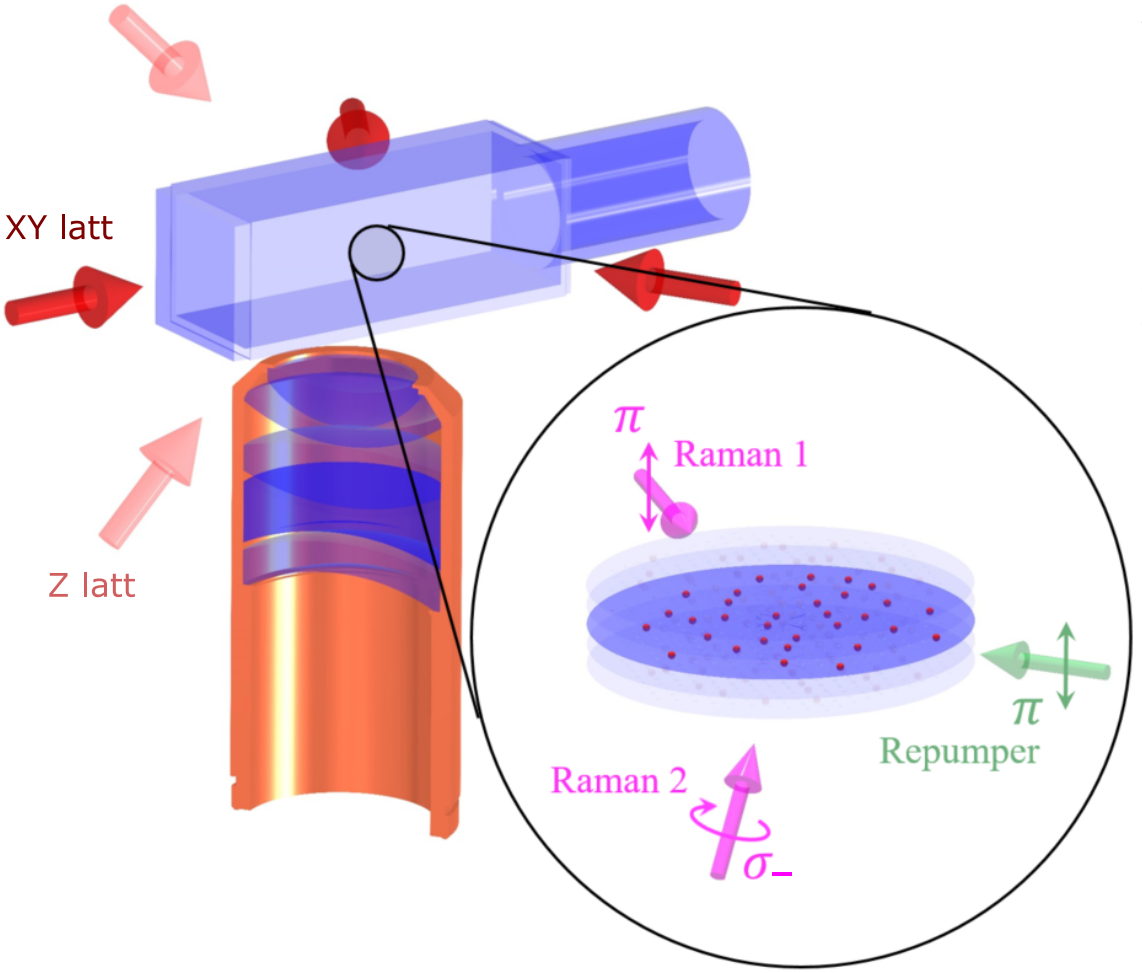

CHAPTER 4
HIGH RESOLUTION IMAGING SYSTEM

The first crucial component in building a quantum gas microscope is the high-resolution imaging system. In this chapter we report the performance of the high-NA objective and the camera in this imaging system. The magnification of the setup is carefully chosen to ensure a good signal-to-noise ratio (SNR) as well as reliable lattice reconstruction during imaging processing.

4.1 Microscope objective

The microscope objective collects the fluorescence photons during Raman sideband cooling (see chapter 6) from below the science cell. It contains a customized lens group[a] designed to provide high resolution images at $\lambda = 671\,\text{nm}$ wavelength, through a 3 mm thick glass cell wall. The objective has an effective focal length of $f = 27\,\text{mm}$ and a entrance pupil diameter of $D = 30\,\text{mm}$. The corresponding numerical aperture (NA) is 0.55. The mechanical part of the lens holder is made of polyetherimide, with an outer thread for easy mounting on controllable stages.

Resolution

The image of a spot object through the objective is described by a point spread function (PSF), whose intensity is given by an Airy disk

$$I(r) = I_0 \left[\frac{2J_1(\tilde{r})}{\tilde{r}}\right]^2, \tag{4.1}$$

where $\tilde{r} = \dfrac{\pi r D}{\lambda f}$ is a reduced quantity obtained from the radial displacement r of the image point from the principal axis. J_1 is the order 1 Bessel function of the first kind. The resolution on the focal plane can be taken as the first intensity zero of the image spot, which corresponds to $\tilde{r} \approx 3.8317$ or $\delta = \dfrac{1.22\lambda}{2\text{NA}}$. Based on the design parameters of this objective, the resolution is $\delta = 740\,\text{nm}$ for 671 nm imaging light. This is comparable to the triangular pinning lattice spacing $\frac{2}{3}\lambda_{\text{latt}} = 710\,\text{nm}$ (see chapter 5). Therefore it will be

[a] designed and manufactured by *Special Optics*

possible to reconstruct the lattice position and to determine the occupancy on each lattice site from the images.

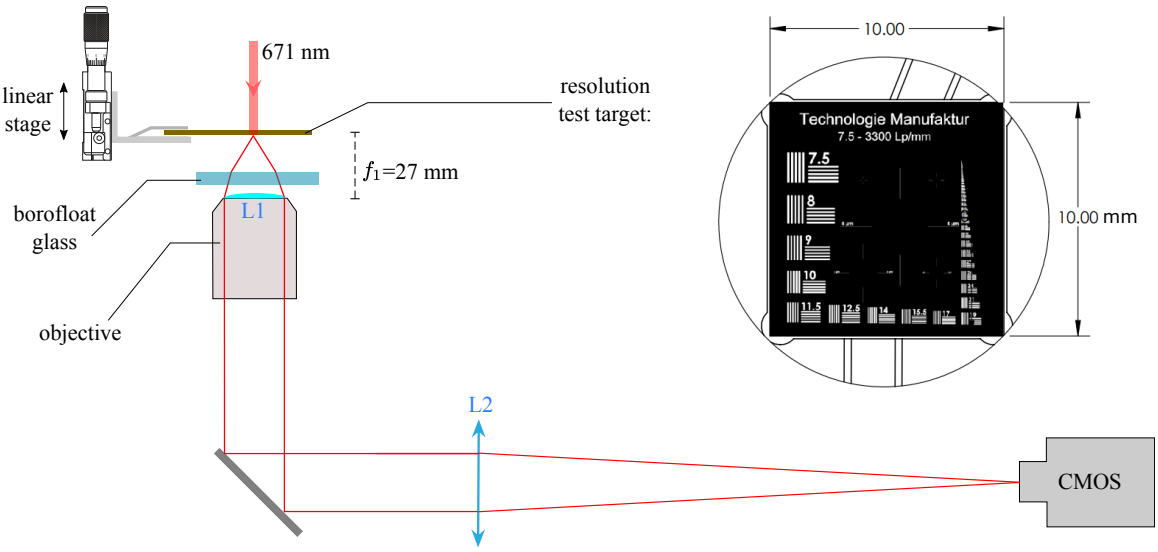

Figure 4.1: Test setup for the objective. Collimated red light is shone from the top onto the resolution target, which is positioned roughly at the working distance of the objective. The distance can be finely adjusted by a linear stage. The inset shows the patterns on the resolution test target. A 3.3 mm thick borofloat glass is put above the objective path to mimic the science cell wall.

In order to test the performance of our objective, we built a side optical setup that mimics the final imaging condition, like shown in figure 4.1. A resolution test target[b] is placed at the focus plane of the objective. Its distance from the objective can be finely controlled by a linear translation stage. The diffracted light from the target is collected and focused on a CMOS camera[c]. Between the target and the objective, a borofloat glass plate with 3.3 ± 0.2 mm thickness is inserted to mimic the wall of the science cell, which is made of the same material, but has a slightly thinner thickness of 3 mm. The glass plate is mounted on a mirror mount, so that its tilt can be adjusted to keep the normal of the plate surface in parallel with the imaging light. Using the high frequency line gratings, we are first able to determine precisely the magnification of the test setup to be $M = 45.1 \pm 0.5$. The resolution of the objective is tested from the PSF of a 0.5 μm pinhole on the target. Since the objective is designed to produce the best resolution through a 3 mm glass, in order to directly compare the designed performance with our measurement, we asked the manufacturer for a set of simulations under the modified glass thickness of 3.3 mm. Both our measured intensity profiles and the simulation are shown in figure 4.2. They are in

[b] Edmund Optics #37-539
[c] Thorlabs DCC1545M-GL

very good agreement for various pinhole target positions. When the target is at the focal point (designed for 3 mm glass), the PSF contains more power on the side peaks, deviating from an Airy function, but the first intensity minima is roughly at 750 nm, similar to the designed resolution. Moving the target about 4 μm away from the expected focal point, the PSF follows an Airy disk better, but with a worse resolution of 990 nm. Through this comparison, we are assured that when operating under the actual condition, the resolution can reach the manufacturer-specified value of 750 nm.

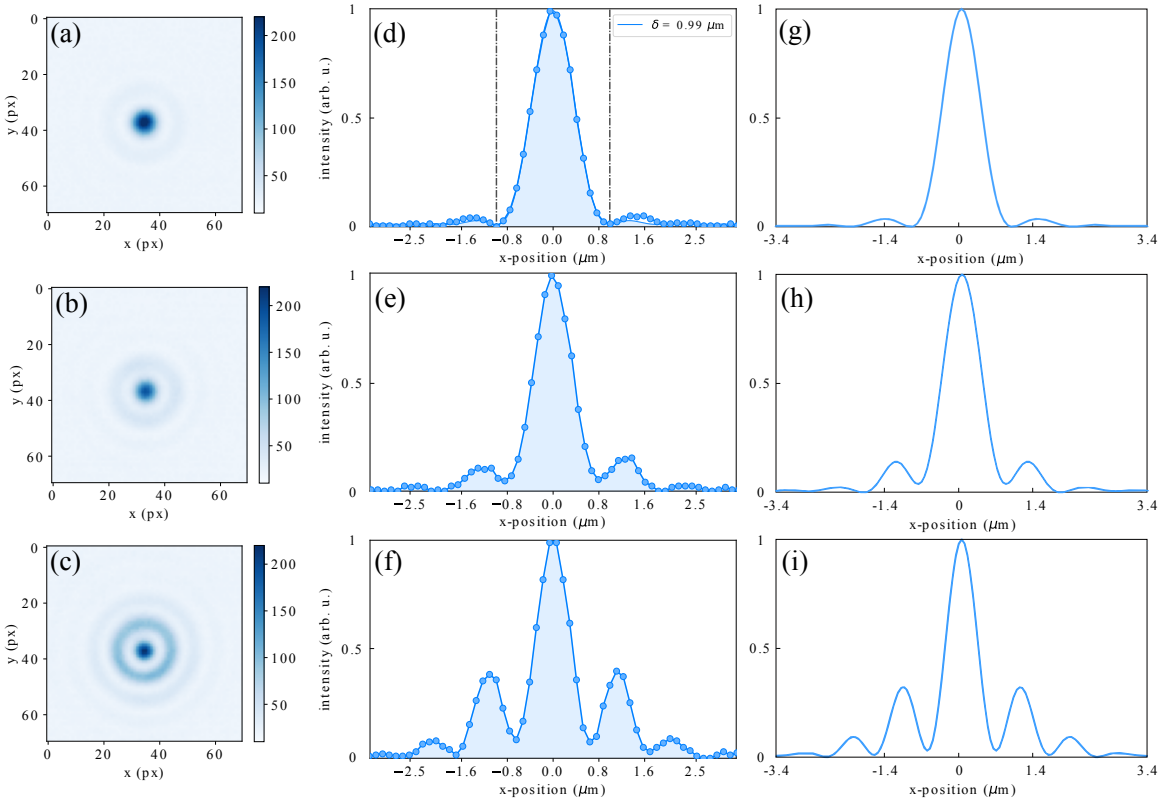

Figure 4.2: Objective point spread functions for the image of a 0.5 μm pinhole after 3.3 mm glass plate, at various distances from the focal plane. The focal plane distance is referenced based on the actual working condition when the glass thickness is 3 mm instead. This distance can be controlled with a precision of 2.5 μm on our test setup, limited by a manual translation stage. (a-c) The images of the pinhole at 4 μm, 2 μm, 0 μm from the focus, towards the objective. (d-f) Radial cuts from the pinhole images on the camera. The intensity profiles are renormalized. By fitting these profiles naively with an Airy function, the positions of the first intensity minima are found at 990 nm, 890 nm and 750 nm at respective distances. (g-i) Simulated PSF by the manufacturer at 4 μm, 2 μm, 0 μm from the focus. The measured PSFs and the simulated PSFs resembles each other at all the tested off-focus distances.

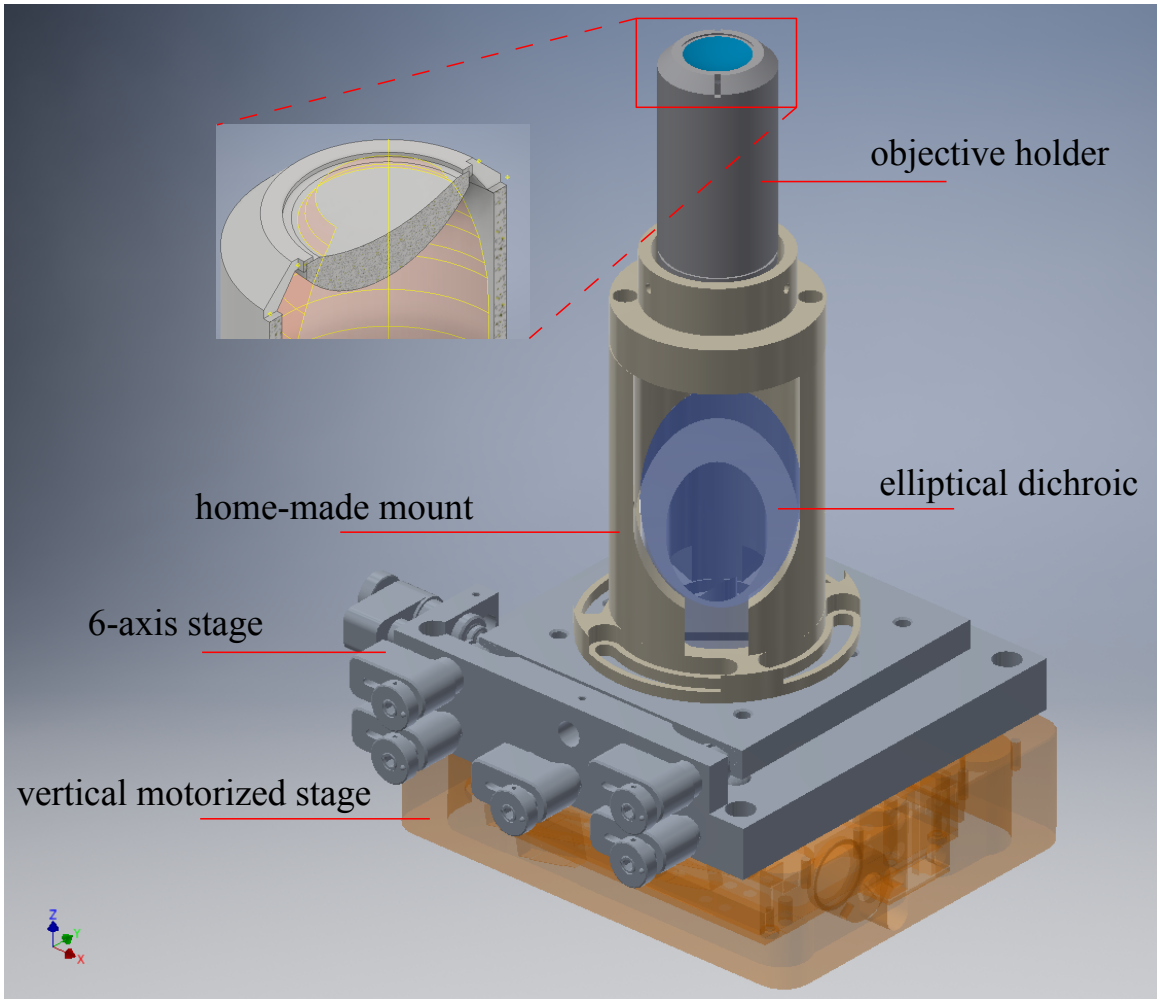

Figure 4.3: The objective mount assembly, which consists of the objective holder, a home-made mount, a 6-axis stage to control the tranlsations and tilt, and a high-precision vertical stage to focus on the atoms. The imaging light from above is reflected by the elliptical mirror.

Positioning

Since the depth of focus of the objective is only $\sim 2\,\mu$m, the focal distance must be controlled with enough precision to maintain the best resolution on the single-atom images. Also, it is necessary for the objective mount to have motorized control over its displacements and tilts. This will help re-optimizing the image quality once the objective has drifted relatively from the atoms. Figure 4.3 shows the mounting of the objective holder. The objective holder is directly screwed onto a cylindrical customized mount, with an opening on the side to fit a 45° mirror to reflect the imaging light. The mount itself sits on two motion

control units — a motorized 6-axis aligning stage[d] and a motorized vertical stage[e]. The former can control the translation along all three axes within 3 mm and the tilt in all three directions within 4°. The latter can change the objective height within 4.8 mm range by a step size of 0.06 μm.

The total height of the mounting system is about 280 mm, which brings the objective entrance pupil to the proper working distance from the cell bottom. Most length of the objective holder fits into the center hole of the bottom curvature coil. While moving closer to the cell, the top part of the objective holder enters the beam path of the Z-lattice (as suggested in figure 5.1(b)). To allow optical access for the z-lattice beams, we made two vertical cuts along the opposite walls of the holder. These cuts allow the high-power Z-lattice beams to pass through while not exposing the inner area of the objective lens system to the air. They are shown in the figure 4.3 inset.

4.2 Choice of magnification

To retrieve spatial distributions from single-atom images efficiently, the position and the orientation of the underlying lattice sites inside the camera frame is usually calibrated based on the periodic pattern of the fluorescence, in a process called lattice reconstruction. This requires there to be enough well-separated image points that can be well-fitted by the PSF. Once the lattice is reconstructed, its position should remain the same from picture to picture given a good stability of the experiment. The atoms can be then identified simply based on the fluorescence intensity on each lattice site. In the final fluorescence image, for a given number of photons that can be collected, there exists a trade-off between a higher signal-to-noise ratio (SNR) and a better resolution for the lattice sites on the camera pixels. In other words, if a higher magnification is used for the imaging system, less photons will be collected on each pixel, producing a noisier picture; Whereas if a lower magnification is used, each single-atom PSF will span over fewer pixels, making the lattice reconstruction less accurate. The stray photons or false firing on a CCD pixel is also more likely to be mistaken as an atom.

4.2.1 Simulations of fluorescence images

To determine a proper magnification for the imaging system, we performed simulations of the single-atom imaging using realistic values. The programme was written by Joris Verstraten and its procedure can be described as the following:

[d] Newport 8095-M
[e] Newport M-VP-5ZA

- Starting with an atom density n achievable in the experiment, the number of atoms is generated over a selected camera area A, or correspondingly over a real-space volume $\frac{A\lambda}{2M^2}$, where M is the magnification and $\lambda/2$ the Z-lattice spacing.
- These number of atoms are randomly placed over this area with a uniform probability (assuming no interactions). Then each atom is snapped to the nearest XY-lattice site.
- For each atom, a PSF centered on its lattice site is generated and normalized to various photon emissions per atom (50, 150 or 500). The average photons N_{pix} that end up in each pixel is calculated by integrating the PSF over the pixel area. The actual number of photons on this pixel is generated from a Poisson distribution with variance N_{pix}.
- Photon count contributions from each atom are added up. A Gaussian noise with a mean of 2 photons and a standard deviation of 2 photons is added on top for every pixel to simulate electronic and other (homogeneous) sources of noise.

Occupancies in the lattice

The first step of the simulation is to estimate the atom density, or the "diluteness" of the cloud. This not only determines the number of atoms within the picture frame, but also affects the probability of two atoms getting pinned very close to each other, either in the same lattice site or in adjacent ones. Such occurrences are not desirable for single-atom imaging, because when a double occupancy (two atoms in a single lattice site) happens, light-assisted collisions let them quickly escape from the trap. So they will not be seen on the image and the distribution of the atoms will be altered. Additionally, when two atoms occupy adjacent sites, their PSFs overlap. Lattice reconstruction will become more tedious if this happens too often.

The atom density is related to the Fermi energy via equation B.2. Our experiment typically reach 20 nK cloud temperature and $T/T_F = 0.076$ in the end of evaporative cooling. This Fermi temperature corresponds to a both-spin peak atom density of $n = n_\uparrow + n_\downarrow = \frac{1}{3\pi^2}\left(\frac{2m\varepsilon_F}{\hbar^2}\right)^{\frac{3}{2}} = 0.56\,\mu\text{m}^{-3}$, which in turn corresponds to an inter-particle distance $d = 1.2\,\mu$m. Additionally, the average cell volume $V_{\text{cell}} = \lambda^3/3\sqrt{3}$ is obtained by multiplying the Wigner-Seitz cell area $2\lambda^2/3\sqrt{3}$ of the triangular lattice with the vertical spacing $\lambda/2$ between lattice planes. Therefore we expect an average site occupancy of $nV_{\text{cell}} = 13\%$. The number of atoms that end up in a particular lattice site can be modeled by a Poissonian distribution with mean atom count $\kappa = 0.13$. This leads to an expected

single-occupancy probability $P(1) = 11.4\%$ and double-occupancy probability $P(2) = 0.74\%$. Even higher occupancy numbers are negligible. In other words, among all occupied lattice sites, the percentage of doubly-occupied sites is about $0.74/(11.4 + 0.74) \approx 6.1\%$. There is some margin to lower this occupancy further if we evaporate away more atoms at the expense of a slightly higher T/T_F. For $T_F = 100\,\text{nK}$ instead, the double-occupancy occurrence is lowered to 2%. We consider this acceptable for extracting the atoms spatial distribution.

In order to gain more insight on the atom distribution statistics, we perform over 500 iterations of the simulations described above, and look at the typical distance (in terms of lattice sites) between the nearest neighboring atoms. From the position of each atom, other lattice sites are labeled according to the straight-line distance from the central one. Sites with equal distance share the same label, as shown in figure 4.4(a). The statistics at $T_F = 100\,\text{nK}$ is shown in subfigure (b). There is no simple pattern on the probability against lattice label as each labeled group has a degeneracy. However, one can see that the probability for adjacent-occupancy to occur is slightly above 15%, while most of the atoms are spaced by over four lattice hoppings (labeled group 6 and above). This leaves enough well-separated PSFs for lattice reconstruction.

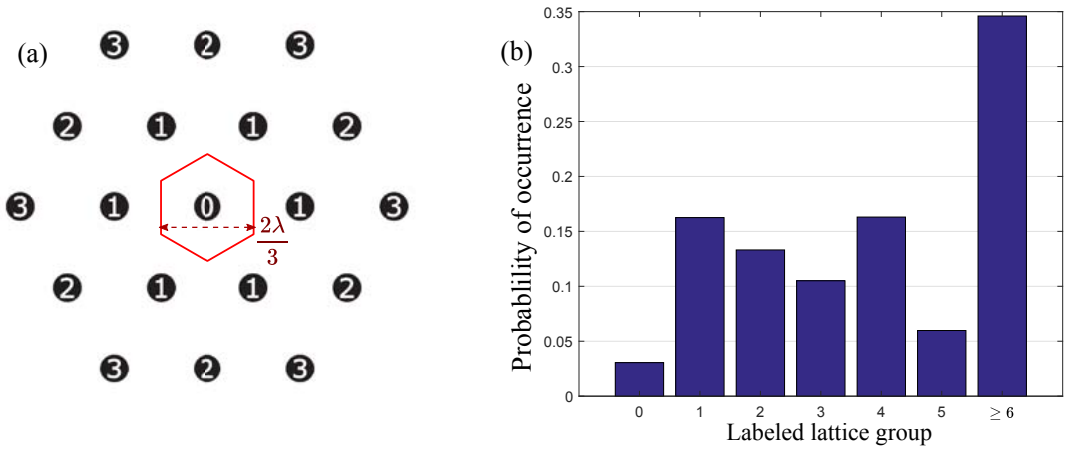

Figure 4.4: (a) Illustration on the triangular lattice sites and how they are labeled according to the distance from the central site. The red hexagon denotes a Wigner-Seitz cell. (b) Occurence frequencies of nearest-atom falling in each labeled site group. The statistics is taken with 500 simulated distributions.

Photon counts per pixel

The camera used for photon collection is a 1024 $\times$ 1024 pixels EMCCD camera[f], whose quantum efficiency over most of the visible light range is 95%. Each pixel is 13 μm by 13 μm in size.

In a rough estimate, we assume conservatively that 200 photons are collected from each atom[g], the peak intensity of an Airy disk is related to the total power by $I_0 \approx 1.17 P_0/\delta^2$, where δ is the resolution as defined earlier in equation 4.1. The spread of the PSF can be roughly taken as the area beyond which intensity drops to $0.37\, I_0$. For an Airy disk this occurs at a radius $r = \delta/2$. The photon count in the central pixel of a PSF and the spread of a PSF are listed for several magnifications in table 4.1. At $M = 50$, the central pixel photon number is 29 on average. The Poissonian standard deviation is $\sqrt{N_{\text{pix}}} = 5.4$, which is below 20% the mean photon count. This is an acceptable level of fluctuation.

Magnification	Photon # in the central pixel	PSF spread area (# pixels)
30	80	2.3
50	29	6.4
75	13	14.3

Table 4.1: Rough estimates on the peak photon counts and the PSF spread at three different magnifications. $M = 50$ seems to be a good compromise.

Simulated image at two magnifications

Figure 4.5 displays the simulated fluorescence images over a 128 $\times$ 128 pixels area of interest. The simulations compare two magnifications with photon number per atom set at 500, 150 and 50. When the photon number is low, magnifications larger than 60 will not be able to provide clear images as the fluorescence is flooded over by the noise. However, for photon number 150 and higher, magnification 40$\sim$60 give reasonable signal levels. In our actual setup, we have chosen $M = 55.6$ based on the focal lengths of our available lens sets.

[f] Andor iXon Ultra 888

[g] If we take the initial photon collection rate as measured in section 6.4, 200 photons can be collected within 300 ms.

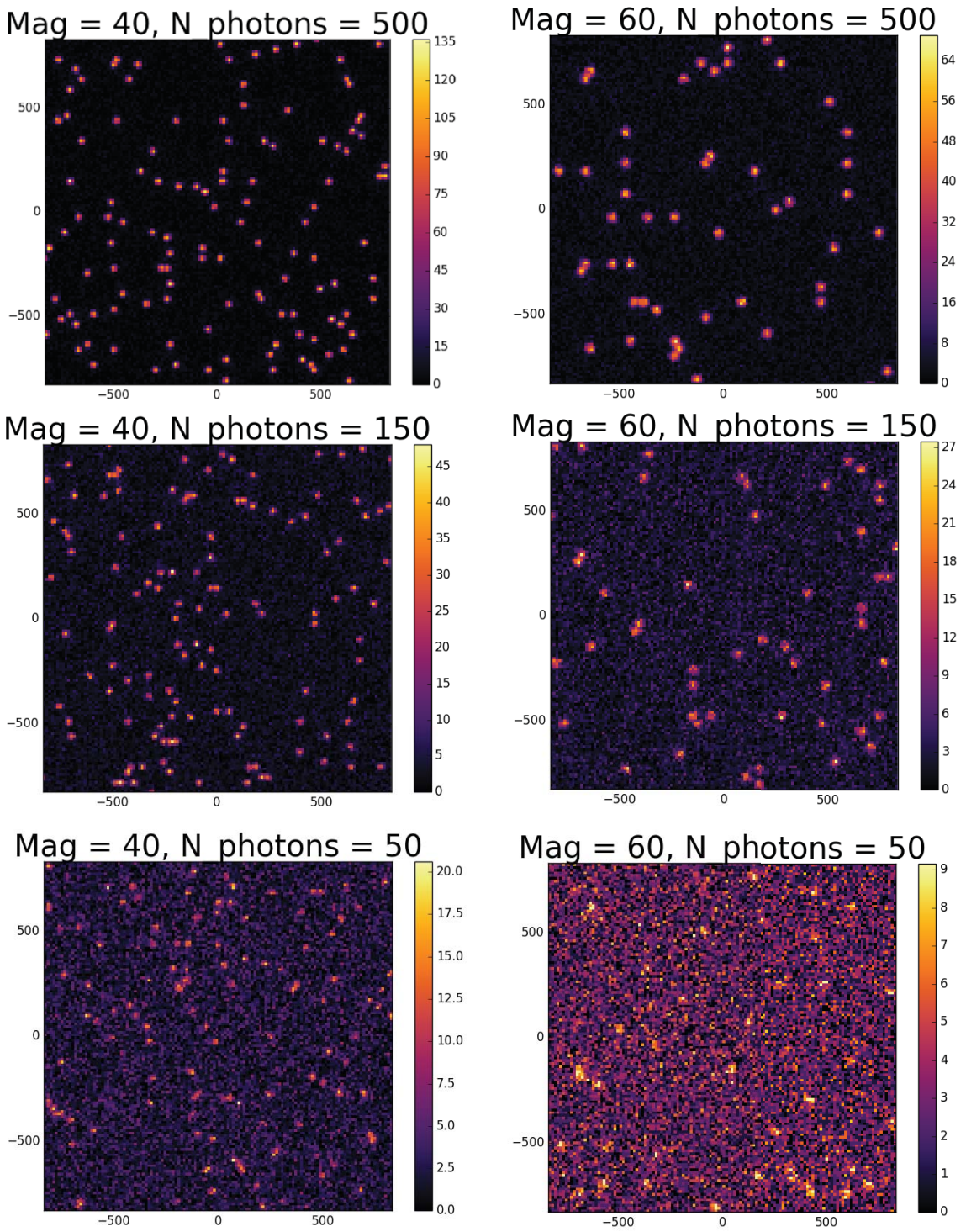

Figure 4.5: Simulated fluoresence images at two magnifications M =40 and 60, and at three different exposure conditions, where photon number per atom are 500, 150 and 50. Reprinted from [136]

4.2.2 Imaging setup

With the ideal magnification known, we implement the optics into the setup. This is done along the vertical imaging axis. The beam height of the reflected imaging light from the objective mount is about 150 mm above the table. We prepared two different 2-inch lens sets to have the option of switching between two magnifications. This is very helpful when we want to have a larger field of view when pre-aligning the objective or when the cloud position has been moved. The first configuration consists of only one converging lens with 1.5 m focal length (figure 4.6(b)). In combination with the $f = 27$ mm objective, this yields a high magnification $M = 55.6$. This is the configuration we will be using for the single-atom imaging as planned ealier. The CCD active region of 1024 by 1024 pixels will include roughly 330×330 lattice sites in the field of view, with each lattice site spanning over ~ 8 pixels. In an alternative configuration for pre-alignment and for absorption imaging, three converging lenses with focal lengths f =300 mm, f =500 mm and f =250 mm respectively are used. They work as two consecutive telescopes and give an overall magnification of 5.6. In figure 4.6(a), two different geometric beam paths are traced out. The orange rays show the atoms fluorescence, hence starts from a point-like source from the center of the cell; The purple rays shows the absorption imaging light, which comes from the top of the cell and is collimated. These lenses are mounted on magnetic bases so that they can be easily switched from the low magnification to the high magnification configuration. With the high-resolution imaging path being setup under the low magnification configuration now, we are ready to perform some preliminary measurements in the presence of a pinning lattice.

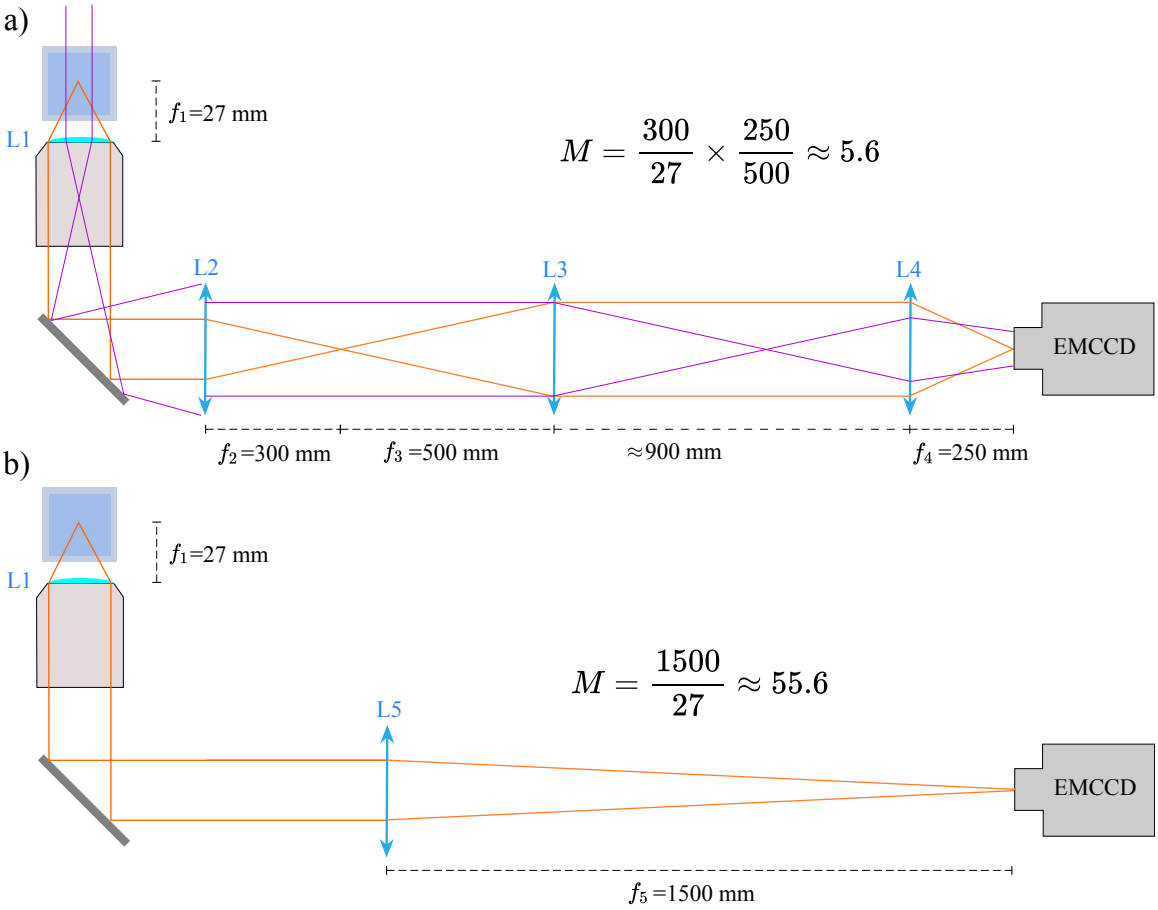

Figure 4.6: (a) Lens set for preliminary alignment on the atom cloud (orange rays) and for absorption imaging (purple rays). The magnification is 5.6. The absorption imaging beam is shone vertcially down from above the cell, and is partially clipped by the second lens L_2 due to strong divergence. (b) Lens set for high magnification single-atom fluorescence images. The magnification is 55.6.

CHAPTER 5
OPTICAL PINNING LATTICES

This chapter describes the pinning lattices used to obtain single-atom imaging. We show several measurements to characterize the lattice, and to analyze the pinning process numerically to evaluate how efficiently the atoms will end up localized in lattice sites during pinning.

5.1 Laser sources and control

5.1.1 Lattice beam configuration

Two 1064 nm 45 W ALS lasers are used to create confinement for the 3D cold atomic cloud before taking in-situ microscopic images. In the XY (horizontal) plane, one ALS laser comes with vertical linear polarization and is reflected to cross with itself twice in a butterfly pattern, as shown in figure 5.1(a). This interference creates a triangular 2D lattice. In the Z (vertical) direction, a 1D lattice is created by the interference of a single beam with its reflection in the vertical plane, with a relative angle of $\sim 90^\circ$, as shown in figure 5.1(b). The choice of this angle is restricted by the optical access through coil mounts above and below the cell. An alternative scheme would be to shine the Z-lattice beam through the microscope objective vertically and do a retro-reflection. Our current scheme leads to a lower trapping frequency for the same laser power, but has two advantages over the alternative scheme: Firstly we avoid the risk to damage the objective or to induce thermal lensing. Secondly the region on top of the cell is kept clear and can be used for other purposes. For example a second imaging setup with less magnification but larger field of view can be added from the top.

The lattices are each controlled by an AOM double pass before going to the science cell. They can be either pulsed on within a microsecond or ramped up gradually by controlling the AOM driving power. We have also observed that comparing to a single pass, the double pass in an cat eye's configuration [137] effectively suppresses the pointing orientation drift shortly after the AOM's turning on. Both XY and Z-lattices are focused to a waist of around 90 μm at the atoms position[a].

[a] based on beam caustic measurement before the science cell.

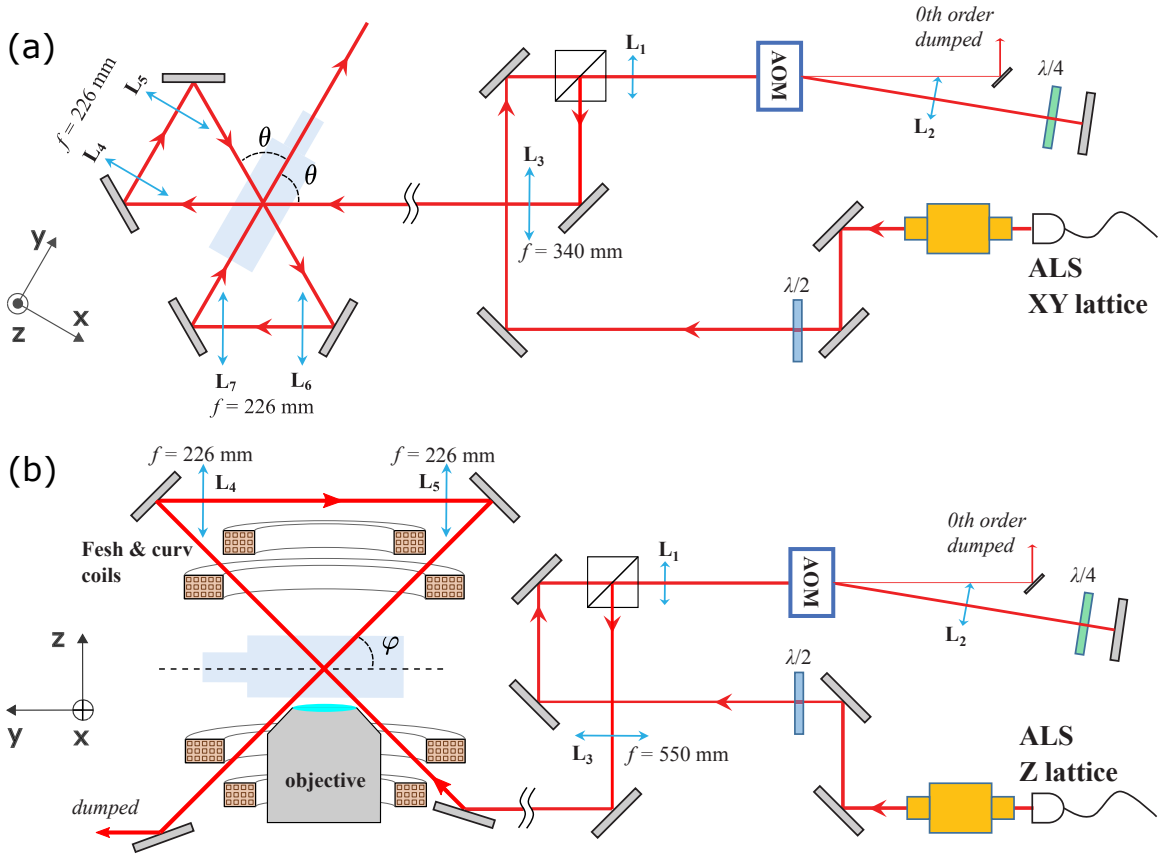

Figure 5.1: (a) Laser setup for the XY triangular lattice. The laser is reflected twice to cross at the atom position in a butterfly pattern with angle $\theta \approx 60°$. (b) Laser setup for the Z-lattice. The laser is passed between the Feshbach and curvature coils diagonally and reflected back in a symmetric manner with $\varphi \approx 45°$.

Lattice laser security lock

Since the last arm of the XY lattice shines along the transport axis in opposite direction of the transport beam, extra precautions must be taken to avoid simultaneously switching on the two high-power beams. We have chosen to add two motorized flip mirrors along the optical path to dump each beam. The choice of flip mirrors over polarizing cubes is to avoid additional thermal lensing effects and to maintain the best laser spatial modes. The flip mirror mounts[b] can provide status signals indicating the current position of the mirror, which are picked up by a home-made security interlock circuit to disable the switch-on of the wrong laser. As shown in figure 5.2, flip mirror 1 positioned before the optical transport entrance viewport is used to dump the XY lattice, and must be flipped down during the optical transport; Flip mirror 2 positioned after the science cell is used to dump the transport beam, and must be flipped down before turning on the pinning lattice. The two allowed laser configurations are described in the drawings.

5.1.2 Turn-on sequence

A series of measurements were performed to characterize the lattice. For this set of measurements, instead of studying the quantum gas in free space, we load the cloud directly from the harmonic trap into the pinning lattice. The experimental sequence is depicted in figure 5.3. After evaporation step 4 (see section 3.1), we obtain a cold cloud of roughly 600 nK. The Z-lattice is first ramped on to a low power of 1 W, giving a trap depth already much larger than the cloud temperature, and the cloud tends to be adiabatically loaded into the lowest lattice band by the end of this initial ramp. Atoms are held in the Z-lattice for 1.5 s, in which period the transport beam is switched off and the flip mirror positions inverted. Next, the XY-lattice is also ramped on to 1 W power before the magnetic field is quickly turned off and atoms are held until the field stabilizes. We can maintain as much as 80% of the atoms during this field switch-off with no sign of heating. Finally, either or both of the pinning lattices power is ramped up to the target lattice power that is being calibrated. During this power ramp, the cloud heats up in proportion to the lattice depth increase.

[b] Standa 8MFM-1

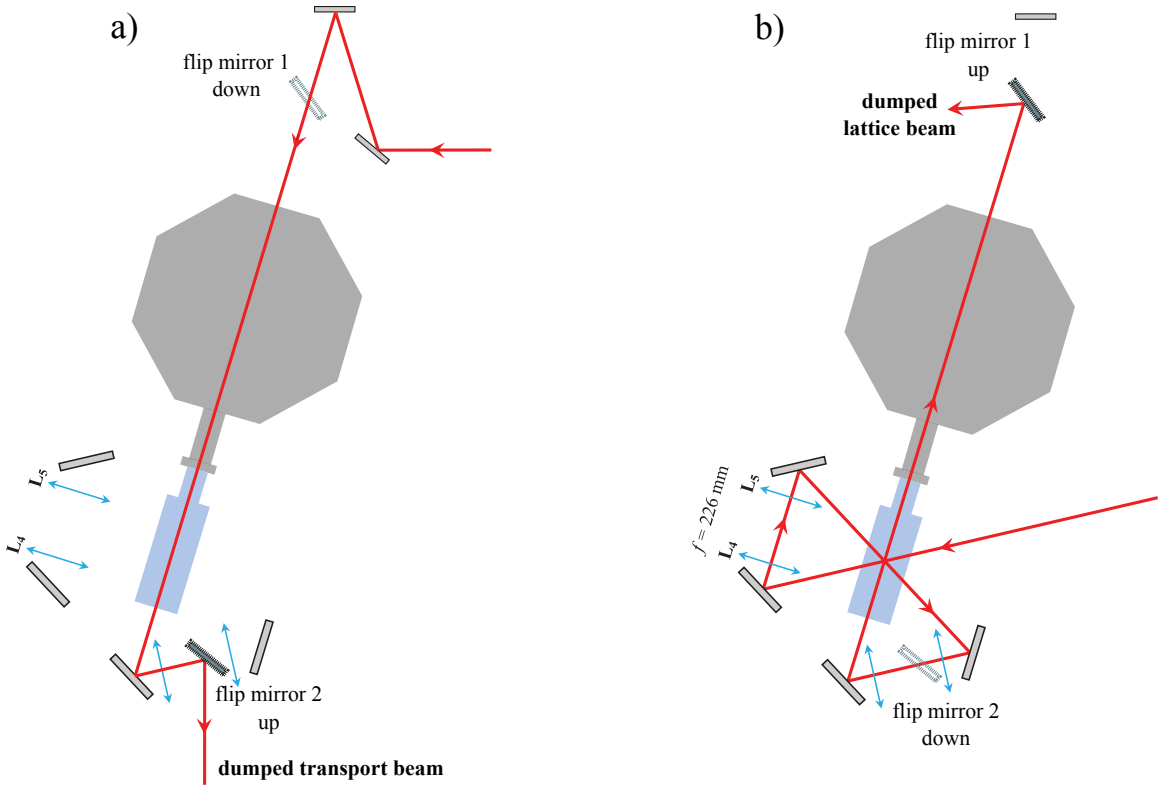

Figure 5.2: Security interlock for safely switching between the transport beam and the lattice beam. (a) During optical transport, flip mirror 1 is down and mirror 2 is upright. The transport beam is dumped after cell and lattice beam is disabled. (b) Later in the sequence, flip mirror 1 is upright and mirror 2 is flipped down. XY lattice beam is dumped before the transport viewport and the tranport beam is disabled.

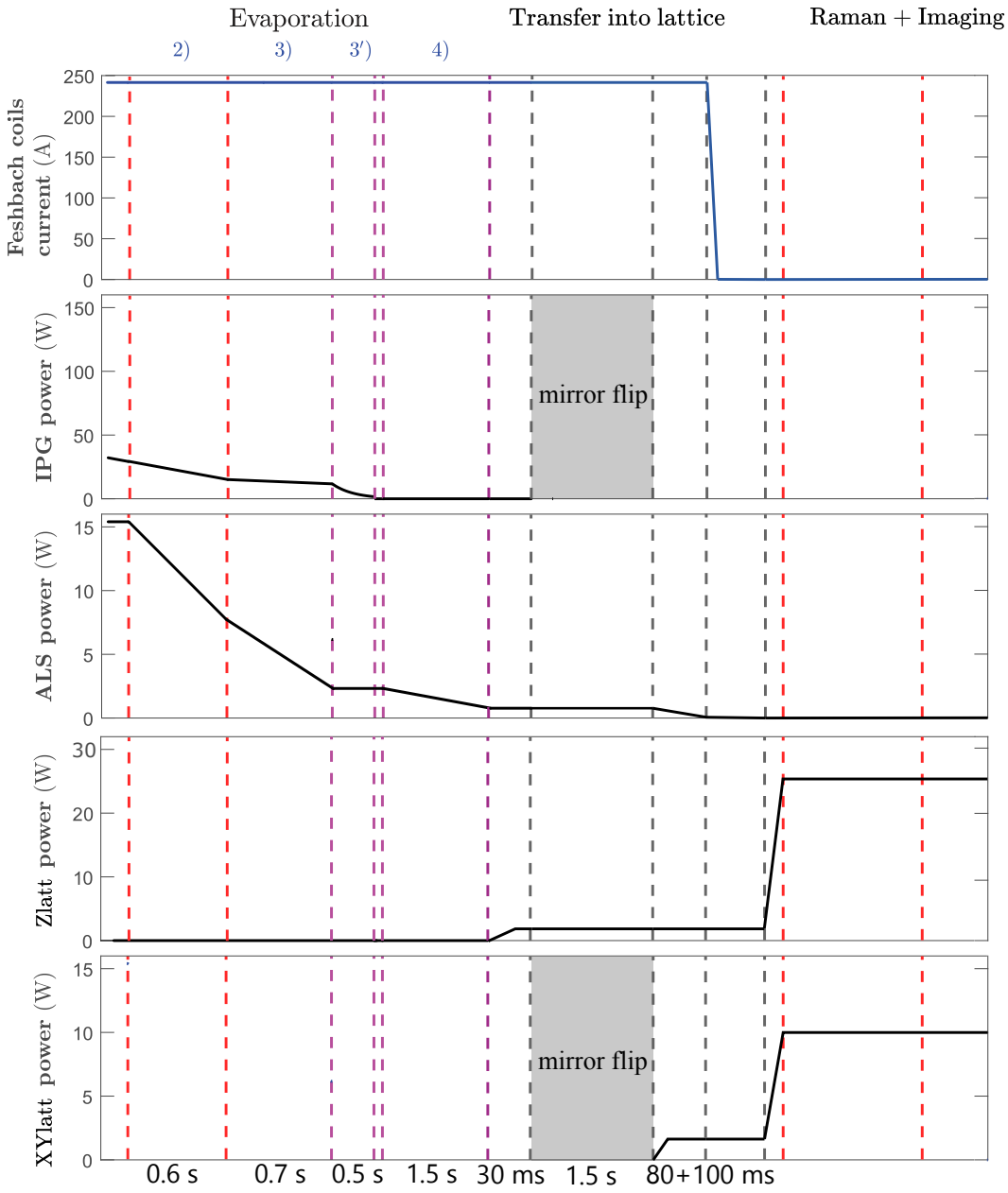

Figure 5.3: Sequence to load into the pinning lattices. After evaporation to step 4, Z-lattice is first turned on at 1 W power. It holds the cloud through a 1.5 s period of mirror flip. Then the XY lattice is turned on as well at 1 W, and the magnetic field is quickly ramped to 0. At zero field, each pinning lattice is increased to its target depth.

5.2 Characterizing the pinning lattice

5.2.1 Estimated trapping frequency

The dipole potential in the optical lattice follows $U(\mathbf{r}) = \alpha(\omega)I(\mathbf{r})$ as in equation2.2. In particular the polarizability for our 1064 nm lattices evaluates to

$$\alpha(\omega = 2\pi \times 252\text{THz}) = \frac{3\pi c^2}{2\omega_0^3}\left(\frac{\Gamma}{\omega-\omega_0} - \frac{\Gamma}{\omega+\omega_0}\right) = 8.36 \times 10^{-37}\,\text{JW}^{-1}\text{cm}^{-2}.$$

The periodicity of the lattice is known by considering the interfering electric field between lattice arms. Following the convention in appendix A, the dipole coupling strength can be directly written as $\Omega = \dfrac{-e\mathbf{E}}{\hbar}\langle e|\,\hat{\mathbf{r}}\,|g\rangle$, where

$$\mathbf{E} = \mathbf{E}_{0,1}e^{i\mathbf{k_1}\cdot\mathbf{r}} + \mathbf{E}_{0,2}e^{i\mathbf{k_2}\cdot\mathbf{r}},$$

For simplicity, we assume the interfering electric fields to have the same polarization and amplitude. Then in the case of Z-lattice, two interfering arms each with intensity I_0 intersecting at an angle 2φ (as in figure 5.1(b)) results in the standing wave intensity:

$$I(\mathbf{z}) = I_0\{2 + 2\cos(2kz\sin\varphi)\}. \tag{5.1}$$

The corresponding trapping frequency is

$$\omega_z^2 = 8\frac{k^2\alpha I_0}{m}\sin^2\varphi. \tag{5.2}$$

Similarly, for three interfering arms having angle 2θ between arms 1& 3 and between arms 2& 3 (as in figure 5.1(a)):

$$\begin{aligned} I(\mathbf{x},\mathbf{y}) &= I_0\{3 + 2\cos[(\mathbf{k_2}-\mathbf{k_1}\cdot\mathbf{r}] + 2\cos[(\mathbf{k_3}-\mathbf{k_2}\cdot\mathbf{r}] + 2\cos[(\mathbf{k_1}-\mathbf{k_3}\cdot\mathbf{r}]\} \\ &= I_0\{3 + 2\cos(4kx\sin\theta\cos\theta) + 4\cos(2kx\sin\theta\cos\theta)\cos(2ky\sin^2\theta))\}. \end{aligned} \tag{5.3}$$

Here $\mathbf{k_i}$ is the wavevector of the ith arm, and the y-axis is defined to be along arm 3. The trapping frequencies are

$$\omega_x^2 = 48\frac{k^2\alpha I_0}{m}\sin^2\theta\cos^2\theta \tag{5.4}$$

$$\omega_y^2 = 16\frac{k^2\alpha I_0}{m}\sin^4\theta. \tag{5.5}$$

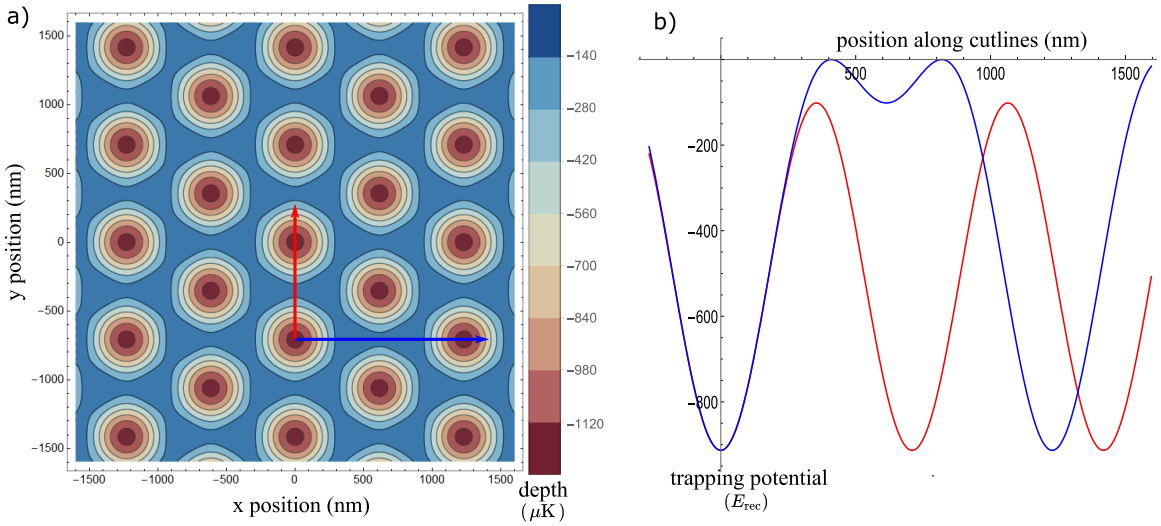

Figure 5.4: (a) A contour plot on the XY pinning lattice on a 3 μm by 3 μm area around the beam intersection, assuming 30 W laser power. The lattice is triangular with a potential minimum of -920 E_{rec} = -1.29 mK. (b) The trap potential along a cut line in the strong and weak trapping direction. The weak trapping depth is 810 E_{rec} and the strong trapping depth is 920 E_{rec}.

	30 W, $\varphi = 45^\circ$	30 W, $\theta = 60^\circ$	
	Z-lattice	XY-lattice along X (strong trapping)	XY-lattice along Y (weak trapping)
trap depth	570 μK = 408 E_r	1.29 mK = 920 E_r	1.14 mK = 810 E_r
trap frequency	0.83 MHz	1.26 MHz	1.26 MHz

Table 5.1: Trapping parameters for 30 W Z-lattice and XY triangular lattice with beam waist 90 μm.

For example, using a power of 30 W and a waist of 90 μm on the XY-lattice intersecting with $\theta = 60^\circ$, the trap depth in the interference region is drawn in a 2D contour plot in figure 5.4(a), in units of recoil energy $E_r = \dfrac{\hbar^2 k^2}{2m} = 1.4\,\mu$K. The inhomogeneity due to the Gaussian profile is ignored. The trap minimum is at -1.29 mK = 920 E_r. The resulting lattice is triangular and the trapping along Y is slightly weaker than the trapping along X, as in figure 5.4(b). The trapping periodicity is $\dfrac{2\lambda}{3}$ along Y, and $\dfrac{2\lambda}{\sqrt{3}}$ along X. Table 5.1 summarizes the relevant parameters for both the XY-lattice and the Z-lattice each with 30 W beam power. This laser power can readily be achieved on our setup after the AOM double passes, although in the following characterizations, we usually use 1/2 $\sim$ 1/3 of this value to have longer atom lifetime in the lattice.

5.2.2 Modulation measurements

Parametric heating

Despite being a very rigid structure due to the strong coherence of lasers, optical lattices are still subjected to vibrations and changing depth due to noise in the laser phase and intensity. These modulations on the lattice can cause heating effects for the trapped atoms. In particular, atoms are especially sensitive to noise of frequency exactly twice the lattice trapping frequency, which causes the "parametric heating". The heating rate in one motional direction $\langle \dot{E}_x \rangle = \Gamma_x \langle E_x \rangle$ is given by [138]

$$\Gamma_x = \pi^2 \nu_x^2 S_k(2\nu_x), \tag{5.6}$$

where $S_k(2\nu_x)$ is the intensity noise spectrum at frequency $2\nu_x$.

Although the parametric heating is usually unwanted, and usually suppressed by PID regulations on the laser intensity, it can also be used as an effective calibration tool.

Amplitude and phase modulation

We performed both amplitude modulation (AM) and frequency modulation (FM) measurements on the XY pinning lattice laser at a final lattice power 10 W in the sequence ramp. Amplitude modulation is done by adding a sinusoidal signal to a DC voltage controlling the lattice AOM driving power; Frequency modulation is applied on the AOM driving frequency using an auxiliary waveform generator. The atom cloud is first held in the lattice for 20 ms for thermalization before a modulation period of 10$\sim$20 ms. after which we probe the cloud density profile where the heating can be seen as a broadening of the cloud size or a loss in atom number.

For AM, a heating peak is present at $2\nu_{\text{tr}}$ as expected, whereas in FM modulation, heating effect is observed both at ν_{tr} and $2\nu_{\text{tr}}$. This is because a FM of the form $A\cos[2\pi f_c t + \beta \sin(2\pi f_{\text{mod}} t)]$ also contains a $2f_{\text{mod}}$ amplitude modulating component:

$$[1 - \frac{\beta^2}{2}\sin^2(2\pi f_{\text{mod}} t)] A\cos(2\pi f_c t).$$

In figure 5.5, we emphasize on the FM calibration results. Subfigures (a) and (b) shows the cloud width and atom count after 200 μs time-of-flight respectively. From the cloud width, two heating peaks are seen at 532 ± 5.5 kHz and 1025 ± 12.5 kHz. From the atom number, two heating peaks are seen at 538 ± 5.5 kHz and 969 ± 13 kHz. In either case, the peak frequencies are not exactly a factor 2 different. This is probably due to anharmonicity

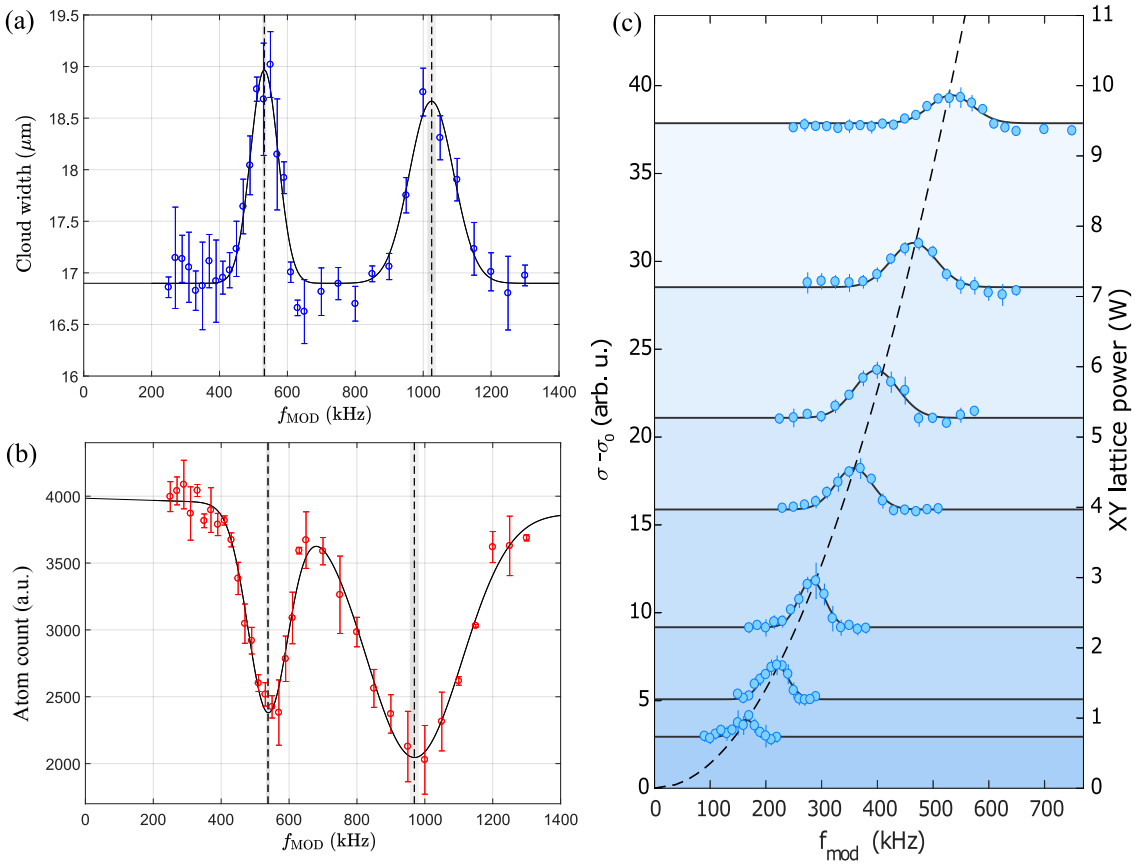

Figure 5.5: Parametric heating induced by modulations on lattices. (a) Cloud width after 200 μs TOF after 10 ms lattice frequency modulation at 10 W laser power. Strong heating effect is observed at 532 and 1025 kHz, roughly corresponding to f_{mod} and $2f_{\mathrm{mod}}$. (b) Atom number count under the same modulation condition. Strong heating effect is observed at 538 and 969 kHz. (c) The first heating peak (blue dots) due to frequency modulation is plotted against XY-lattice power. The peak frequency is proportional to $\sqrt{P}$ (dashed parabola).

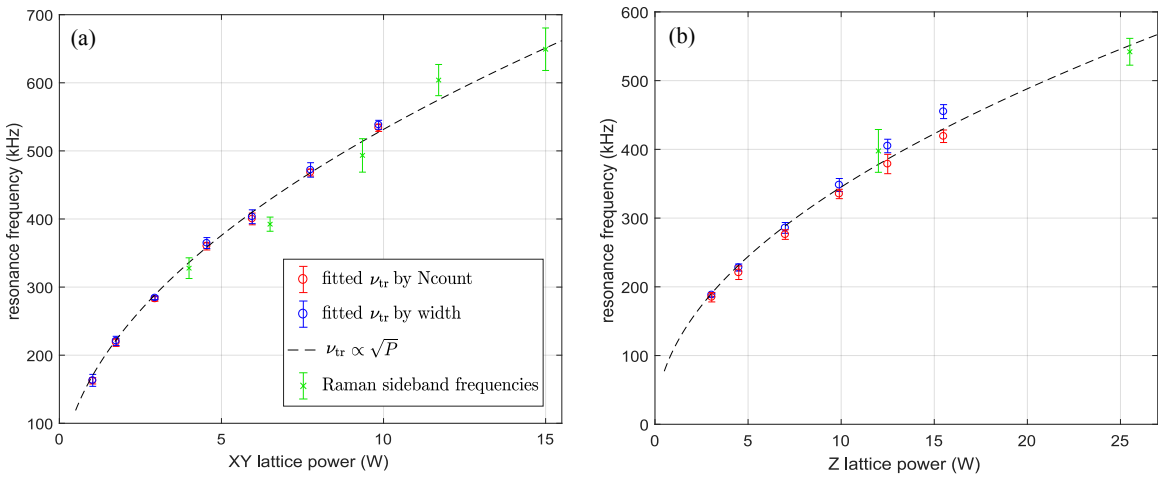

Figure 5.6: *Left*: Power scaling curve for XY-lattice based on various trapping freuqency measurements. Blue dots: heating peaks fitted from maximum cloud widths in FM, same as in subfigure 5.5(a). Red dots: heating peaks fitted from minimum remaining atom count in FM. Green dots: Raman sideband frequencies as measured in section 6.4. *Right*: Power scaling curve for Z-lattice.

of the trap[c].

Repeating such measurements for several XY-lattice and Z-lattice powers, and focusing only on the first peak corresponding to ν_{tr}, we see the resonance of heating follows nicely to the theoretical $\nu_{tr} \propto \sqrt{P}$ scaling law (figure 5.5 (c) and figure 5.6). The scaling constant is $168\,\mathrm{kHz}\cdot\mathrm{W}^{-\frac{1}{2}}$ for the XY-lattice and $109\,\mathrm{kHz}\cdot\mathrm{W}^{-\frac{1}{2}}$ for the Z-lattice. Both values are about 25% lower than our earlier estimate based on a beam waist of $90\,\mu$m. We suspect that the actual beam waist at the atom position deviates from the caustic measurement due to the thermal lensing from glass cell walls. Since the parametric heating result is a more direct measurement on the trapping frequencies, we determine the actual beam waist to be around $120\,\mu$m. Additional trapping frequency data from Raman sideband transitions also (see section 6.4) agree pretty well with the lattice modulation result.

5.2.3 Kapitza-Dirac scattering

One way to check the periodic pattern of the lattice is through Kapitza-Dirac scattering, first predicted by Paul Dirac and Pyotr Kapitza in 1933 [139]. This scattering effect can be described by a stimulated Compton scattering of the cold atoms by the standing wave of the lattice within a short period of time with respect to the kinetic energy of the atoms (i.e. in the Raman-Nath regime). Thus the kinetic terms in the interaction Hamiltonian can be

[c] In our calculation, only 6 bound states are present in a 9 W lattice. The assumption of deep trapping is partially inaccurate even though the most atoms are expected to be in the lowest band.

neglected.

Following the mathematical description by Gupta et al. [140], but keeping the notations in consistent with our convention in appendix A, the standing wave potential can be expressed as

$$U(\mathbf{r},t) = -\frac{\hbar\Omega^2}{4\Delta} f^2(t) \left| \sum_{\mathbf{k}} e^{i\mathbf{k}\cdot\mathbf{r}} \right|^2 .$$

Here Ω and Δ are the coupling strength and detuning of each individual lattice beam as defined in appendix A. The detuning is assumed to be large: $\Delta \gg \Gamma^2/4$. $f(t)$ is the time-varying part of the electric field. The last factor in modulus square contains the spatial interference between all lattice arms, and can be identified with the expressions in equation 5.1 and 5.3.

Given an initial wavefunction $|\psi_0\rangle = |g,0\rangle$ in the ground internal state and carrying zero momentum, the wavefunction after scattering is

$$|\psi\rangle = |\psi_0\rangle \exp\left\{ -\frac{i}{\hbar} \int dt' U(\mathbf{r},t') \right\} = |\psi_0\rangle \exp\left\{ \frac{i\Omega^2\tau}{4\Delta} \left| \sum_{\mathbf{k}} e^{i\mathbf{k}\cdot\mathbf{r}} \right|^2 \right\}, \tag{5.7}$$

where $\tau = \int dt' f^2(t')$. For simplicity, we replace the quantity $\dfrac{\Omega^2\tau}{2\Delta}$ by the notation θ_{KD}, which represents the pulse area of the Kapitza-Dirac scattering. Then the scattered wave function by our triangular lattice can be written as:

$$\begin{aligned}
|\psi\rangle &= e^{i\frac{3}{2}\theta_{\text{KD}}} e^{i\theta_{\text{KD}}[\cos(\mathbf{b_1}\cdot\mathbf{r})+\cos(\mathbf{b_2}\cdot\mathbf{r})+\cos(\mathbf{b_3}\cdot\mathbf{r})]} |\psi_0\rangle \\
&= e^{i\frac{3}{2}\theta_{\text{KD}}} \sum_{n_1,n_2,n_3} i^{n_1+n_2+n_3} J_{n_1}(\theta_{\text{KD}}) J_{n_2}(\theta_{\text{KD}}) J_{n_3}(\theta_{\text{KD}}) e^{i(n_1\mathbf{b_1}+n_2\mathbf{b_2}+n_3\mathbf{b_3})\cdot\mathbf{r}} |\psi_0\rangle \\
&\propto \sum_{n_1,n_2,n_3} i^{n_1+n_2+n_3} J_{n_1}(\theta_{\text{KD}}) J_{n_2}(\theta_{\text{KD}}) J_{n_3}(\theta_{\text{KD}}) |g, (n_1-n_3)\hbar\mathbf{b_1} + (n_2-n_3)\hbar\mathbf{b_2}\rangle .
\end{aligned} \tag{5.8}$$

Here we have defined $\mathbf{b_1} = \mathbf{k_3} - \mathbf{k_2}$, $\mathbf{b_2} = \mathbf{k_1} - \mathbf{k_3}$ and $\mathbf{b_3} = -\mathbf{b_1} - \mathbf{b_2}$ in a cyclic way. J_n is the order n Bessel function of the first kind, which follows the identity $e^{i\alpha\cos(\beta)} = \sum_{n=-\infty}^{\infty} i^n J_n(\alpha) e^{in\beta}$. The atom cloud has been scattered into states of discrete momenta, quantized by $\hbar\mathbf{b_1}$ and $\hbar\mathbf{b_2}$.

We have performed Kapitza-Dirac diffraction on a molecular BEC cloud, which is obtained by evaporating near 665 Gauss on the BEC side of the Feshbach resonance[d]. The

[d]The actual sequence is more complicated as the evaporation and magnetic field ramp are interspersed. This is to optimize the number and lifetime of the molecules. Details of the sequence is omitted.

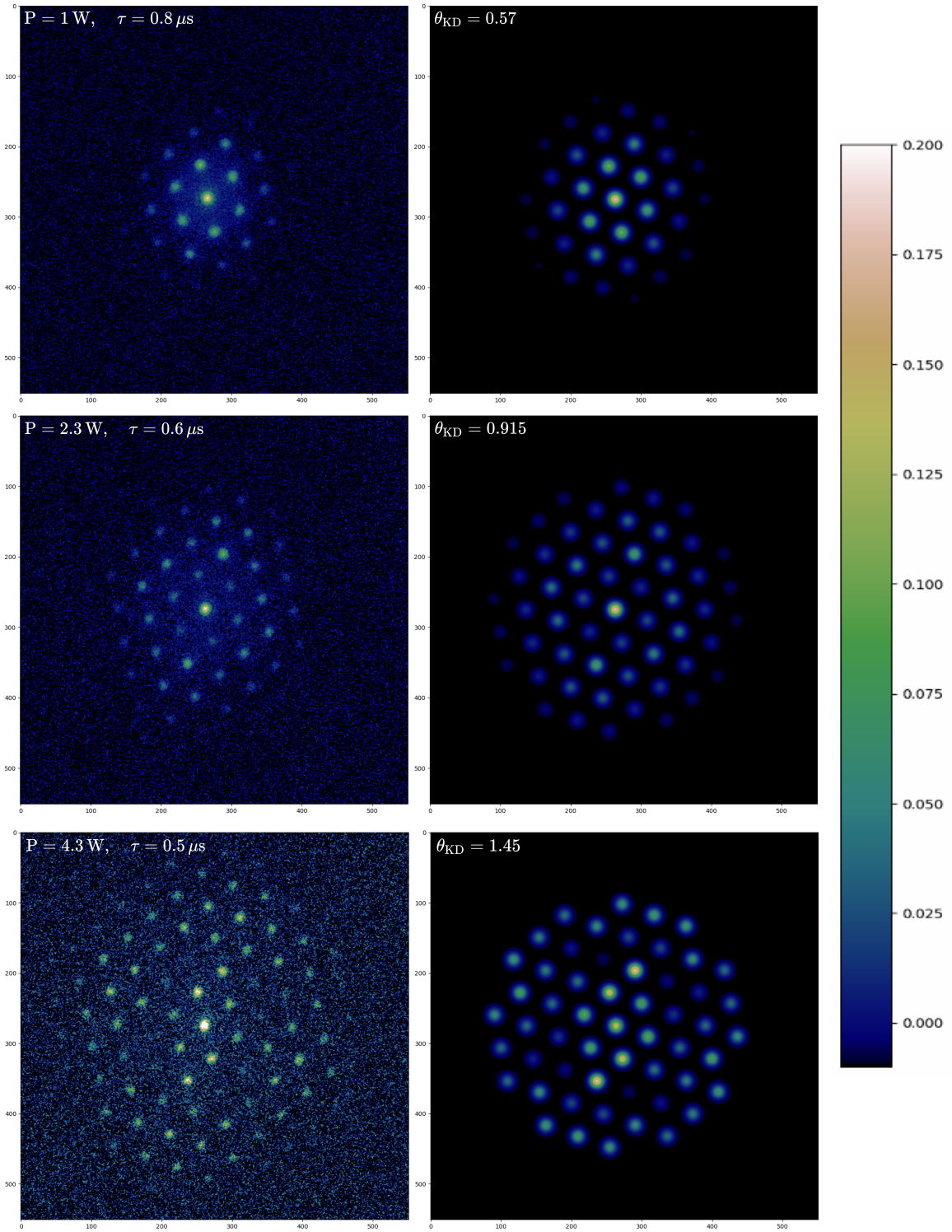

Figure 5.7: Kapitza-Dirac scattering result. Average of 60 absorption pictures after 2 ms TOF is shown in the left column. For the given lattice power P and pulse time τ, simulations with the corresponding pulse area θ_{KD} are shown on the right column. The free fitting parameters for the simulations are the "fudge factors" on the single beam electric field amplitudes.

XY-lattice is pulsed on for various duration and at various power. For each resulted pulse area θ_{KD}, we took 60 absorption images with 2 ms TOF. Taking the average of these images, we observed clear diffraction pattern in which the peaks are spaced by 50 pixels $\approx 115\,\mu$m (figure 5.7). For molecules of mass twice that of a lithium atom, the expected diffraction peak spacing is $\dfrac{\hbar|\mathbf{b}|}{2m_{\text{Li}}}t_{\text{TOF}} = 108\,\mu$m, very close to what we saw. In addition, we made simulations on the diffraction pattern with three tuning factors $\alpha_{\{1,2,3\}}$, to account for possible intensity imbalance on the three lattice arms. For example, the electric field strength on the ith lattice arm is modified to $\Omega_i' = \alpha_i\Omega_i$. Subsequently, the Bessel functions' contribution in equation 5.8 is modified to $J_{n_1}(\alpha_2\alpha_3\theta_{\text{KD}})J_{n_2}(\alpha_3\alpha_1\theta_{\text{KD}})J_{n_3}(\alpha_1\alpha_2\theta_{\text{KD}})$. Using fitted fudge factors $\alpha_{\{1,2,3\}} = \{1.18, 0.92, 0.86\}$, the simulation reproduces most features on the measurements at every pulse area, showing very good agreement on the weights of the diffraction peaks.

5.2.4 Band mapping

In cold atom experiments, a commonly used method to directly visualize lattice band structure occupation is band mapping. It is done by adiabatically closing the band gap, so that an atom in the n$^{\text{th}}$ band with quasi-momentum q will evolve into the momentum state $p = q \pm 2nk_L$ after the band unfolds. In a time-of-flight image, a group of atoms starting with momentum $\hbar\mathbf{k}$ expands freely and asymptotically to a distance $\mathbf{r} = \dfrac{\hbar\mathbf{k}}{m}t_{\text{TOF}}$. The final cloud density in space therefore reveals the initial momentum distribution, which in turn reveals the structure of the filled bands before ramp-off. Figure 5.8 shows the shape of the first four Brillouin zones for a square lattice and a triangular lattice.

For adiabatic following to happen during lattice ramp, the probability of inter-band transition must remain low when the lattice depth is reduced at a rate $\dot{V}_0$ [141, 142]

$$|\langle\psi_{n,q}|\dot{V}_0|\psi_{m,q}\rangle| \ll \frac{(E_{m,q} - E_{n,q})^2}{\hbar}. \tag{5.9}$$

Assuming a linear ramp in lattice power, this requires the ramping time to be on the order of $t_{\text{ramp}} \gg \dfrac{\hbar V_0}{16E_r^2}$ in a 1D lattice.

XY-lattice mapping result

We performed a band mapping with the cloud starting in 1.5 W XY-lattice, whose trapping frequency is roughly 200 kHz. The lattice is ramped off in 600 μs before a 1.5 ms TOF. The cloud optical density after TOF is shown in figure 5.9, where a Gaussian filter has been applied to emphasize the cloud from the background noise. The hexagonal shape of

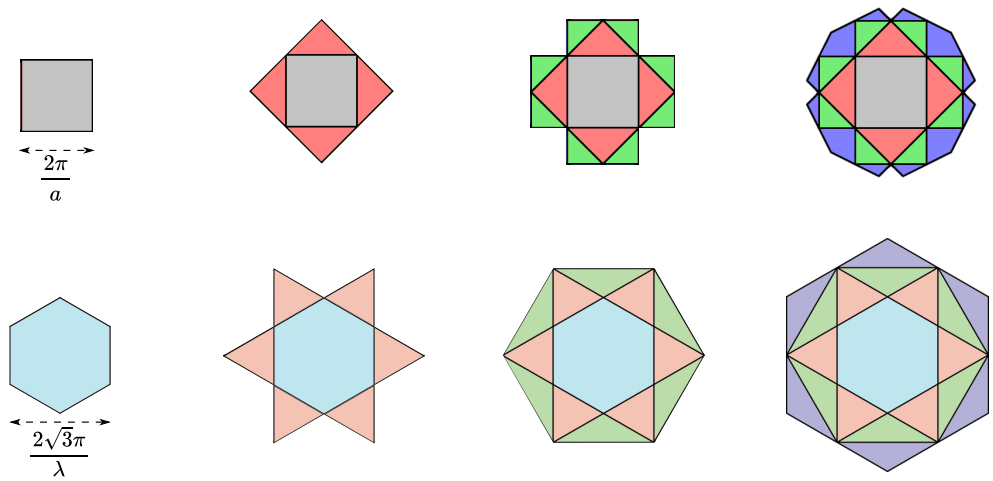

Figure 5.8: *Top row*: Filling up the square lattice Brillouin zones 1 to 4 from left to right. *Bottom row*: Filling up the triangular lattice Brillouin zones 1 to 4 from left to right.

the first Brillouin zone can be clearly seen. From the XY-lattice spacing $2\lambda/3$, the first Brillouin zone is a hexagon with width $2\pi \cdot \sqrt{3}/\lambda$, whose corresponding size at 1.5 ms TOF is marked by the red dotted line. The small discrepancy between it and the size of our cloud could be a combined result of the uncertainty in exposure timing, the initial spread in the atoms momentum, and the limited focus depth of the objective.

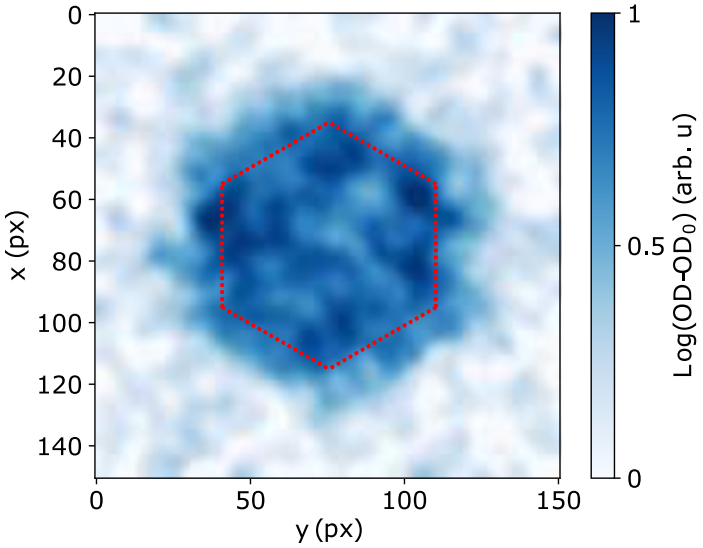

Figure 5.9: Band mapping for XY-lattice at 1.5 W. The lattice is ramped off in 600 μs and the cloud expanded for 1.5 ms. The expanded cloud shows the hexagonal shape of the first Brillouin zone. The expected size of first Brillouin zone is indicated by the red dashed hexagon.

5.3 Evaluating the pinning efficiency

Imaging the atoms in situ requires them to be well localized inside the lattice sites with low probability of escaping or tunneling. We have investigated certain aspects of the pinning

process numerically based on the band structure of our pinning lattices. In particular, we estimated the occupation of energy bands as the lattice is initially ramped on, which reflects how accurately can the atom distribution be preserved during pinning.

5.3.1 A quick reminder on lattice band theory

For simplicity we recapitulate on the general treatment for 1D lattice. Generalization to a 3D Bravais lattice is straightforward by finding the primitive cell and the corresponding reciprocal lattice.

Bloch's theorem

Within a periodic potential $V(x)$ with period a equal to the lattice parameter, the stationary Schrödinger equation is given by

$$\left(\frac{\hat{p}^2}{2m} + \hat{V}(\hat{x})\right)\psi_{n,q} = E_{n,q}\psi_{n,q}. \tag{5.10}$$

The eigenstate $\psi_{n,q}$ are called the Bloch waves with band index n and quasi-momentum q. It has the form of

$$\psi_{n,q}(x) = e^{iqx}u_{n,q}(x), \tag{5.11}$$

where $u_{n,q}(x+a) = u_{n,q}(x)$ has the same periodicity as the lattice potential. Therefore the Bloch wave gains only a phase factor after translation by a. Restricting this phase within 2π range, the quasi-momentum is limited to the first Brillouin zone, $q \in [-\frac{\pi}{a}, \frac{\pi}{a})$.

If the lattice has finite length $L = N_s a$, the quasi-momentum will be discretized by [143]

$$q = \frac{2\pi n}{L}, \qquad \text{with} -\frac{N_s}{2} < n < \frac{N_s}{2} - 1.$$

Therefore N_s is also the number of quasi-momenta within the first Brillouin zone.

Band structure calculation

Plugging the Bloch wave equation 5.11 back into the Schrödinger equation 5.10, one can find numerical solutions for the band structure in the optical lattice potential of the form $V_{\text{latt}}(x) = V_0 \sin^2(\frac{k_L x}{2})$. Both the lattice potential and the amplitude of the Bloch wave have periodicity $a = \frac{2\pi}{k_L}$. Expanding the equation in Fourier components with wavevector[e]

[e] Here we have introduced a "lattice wavevector" k_L that differs from the single beam wavevector k. For a 1D lattice created by two counter-propagating beams, $k_L = 2k$.

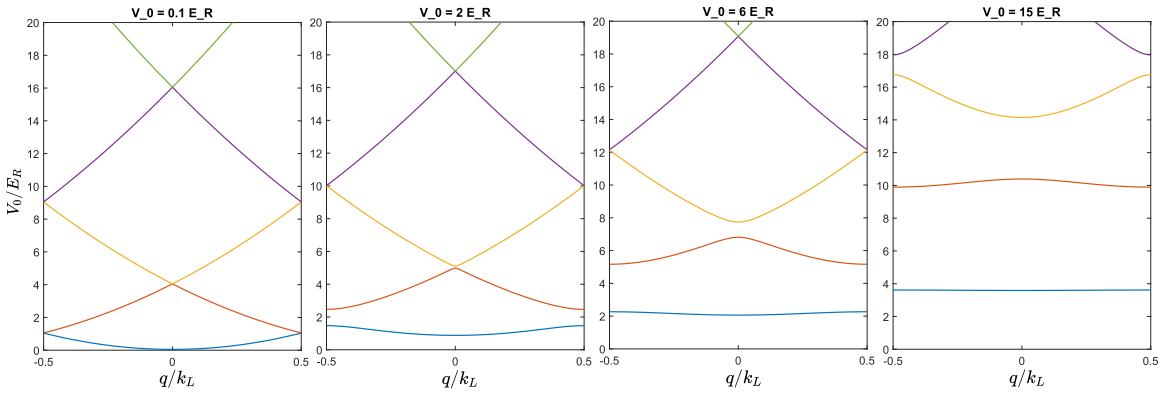

Figure 5.10: Numerical calculation on the band structure of a toy 1D lattice at various trap depths. V_0 = 0.1, 2, 6 and 15 E_r from left to right.

at multiples of k_L, the eigen equation can be rewritten as

$$C_j^{n,q}\left[\frac{\hbar^2(q+jk_L)^2}{2m}+\frac{V_0}{2}\right]-\frac{V_0}{4}\left(C_{j-1}^{n,q}+C_{j+1}^{n,q}\right)=E_{n,q}C_j^{n,q}, \tag{5.12}$$

where $C_j^{n,q}$ is the coefficient for Bloch wave amplitudes $u_{n,q}=\sum_{j\in\mathbb{Z}}C_j^{n,q}e^{ijk_Lx}$.

This eigen equation can be solved by diagonalizing a matrix with truncated terms of C_j. For example in figure 5.10, the structure of the lowest band at several $V_0 < 15\,E_r$ are calculated with $|j|<5$. For deeper lattice, the rank of the matrix must be increased accordingly. A reasonable truncation for $V_0/E_r = 50$ is $|j|<20$ [144].

Wannier functions

When studying systems with strong lattice potential, it is more natural to use eigenbasis localized in space, such a basis is given by the Wannier functions, which can be obtained from the delocalized Bloch waves through discrete Fourier transform [141]

$$w_{n,j}(x)=w_n(x-x_j)=\frac{1}{\sqrt{N_s}}\sum_{q\in\mathrm{BZ1}}\psi_{n,q}(x)e^{-iqx_j}, \tag{5.13}$$

and follows the orthogonality condition

$$\int w_m^*(x-x_i)w_n(x-x_j)dx=\delta_{m,n}\delta_{i,j}.$$

In second quantization, the Hamiltonian can be rewritten as [144]

$$\hat{H}=\sum_{n,q\in\mathrm{BZ1}}E_{n,q}\hat{b}_{n,q}^\dagger\hat{b}_{n,q}=-\sum_{n,i,j}J_n(x_i-x_j)\hat{a}_{n,i}^\dagger\hat{a}_{n,j} \tag{5.14}$$

using the Bloch state creation operator $\hat{b}^\dagger$ or the Wannier state creation operator $\hat{a}^\dagger$. From the definition of Wannier states, it follows that

$$J_n(x_i - x_j) = -\frac{1}{N_s} \sum_{q \in \mathrm{BZ1}} E_{n,q} e^{iq(x_i - x_j)}, \tag{5.15}$$

which represents the hopping amplitude from site x_j to site x_i within the nth band. Conversely, the dispersion relation in the n$^{\text{th}}$ band can be expressed as

$$E_{n,q} = -\sum_{i-j} J_n(x_i - x_j) e^{-iq(x_i - x_j)} = -\sum_{j=1}^{\infty} 2\cos(jaq) J_n(ja). \tag{5.16}$$

Tight binding limit

Under the tight-binding limit, where lattice depth is much larger than the recoil energy, hopping beyond the nearest neighboring site is strongly suppressed. Consider only the average energy in site $\bar{E}_n = \frac{1}{N_s}\sum_q E_{n,q} = -J_n(0)$, and the neareat-neighbor hopping [144]

$$J_n = J_n(a) \approx \frac{4E_r}{\sqrt{\pi}} \left(\frac{V_0}{E_r}\right)^{\frac{3}{4}} \exp\left(-2\sqrt{\frac{V_0}{E_r}}\right),$$

the Hamiltonian can be simplified to

$$\hat{H} \approx \sum_{n,j} \left[\bar{E}_n \hat{a}^\dagger_{n,j} \hat{a}_{n,j} - J_n \hat{a}^\dagger_{n,j+1} \hat{a}_{n,j}\right]. \tag{5.17}$$

5.3.2 Calculated structure for the pinning lattice

We numerically calculated the band structure for our Z-lattice and XY-lattice. Since these calculations are done in prior to our experimental calibrations on the lattices, we have assumed the trap depths optimistically based on a smaller beam waist. Still, the discussion here is good for illustrative purpose, and future improvements on the lattice beam focusing could make these trapping conditions practically achievable.

For the Z-lattice, we assumed a trap depth of $V_0 \approx 1.1\,\mathrm{mK} \approx 780\,E_r$. At this trap depth, the Z-lattice holds 24 trapped bands. Even just below the top of the trap potential, these trapped bands appear quite flat, although there is obvious anharmonicity from the unequal band gaps. The cacluated band structure near the top of the trapping potential is shown in figure 5.11 (a). Subfigure (b) shows the energy difference between successive bands against the band index, taken at the center of the Bruillouin zone. The gap between

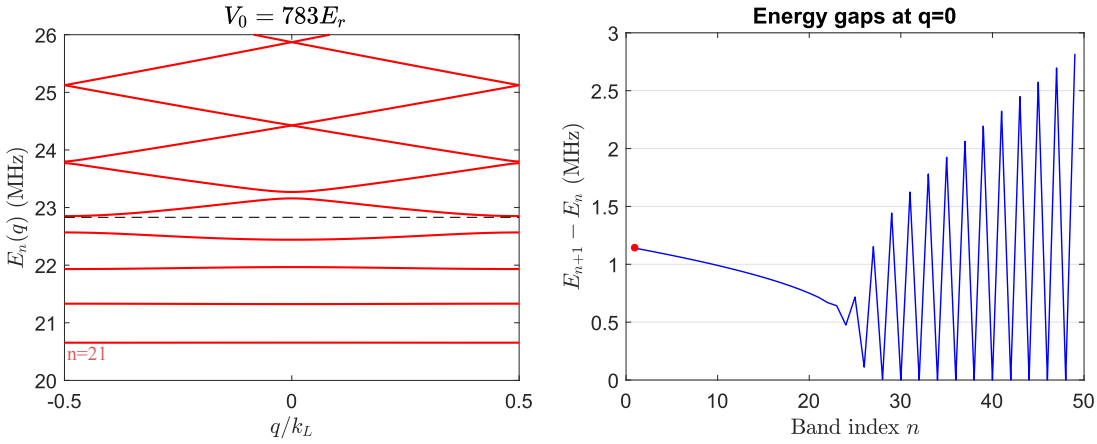

Figure 5.11: Calculated band structures. (a) Zoom on the band structure near the top of the trapping potential, which is denoted by the horizontal dashed line. (b) The energy difference between adjacent bands measured at zero quasi-momentum. The fundamental trapping freuquency is 1.14 MHz, and the highest bound state has index $n = 24$. For higher bands, the band gap at the center of the Brillouin zone is closing up as seen from the zigzaging shape of the plot.

the lowest band and the next lowest is 1.14 MHz. The gap gets smaller for higher bands as expected, and decreases to roughly 0.5 MHz just before a free state. For index 24 and higher, the dispersion relation is very similar to that of a free particle.

Repeating similar calculation for the XY-lattice assuming 2.5 mK trap depth, we find the first transition at 1.8 MHz. This transition frequency between non-degenerate levels decreases to around 0.4 MHz just below the open levels. We observe a non-negligible anharmonicity, which encourages us to add a controlled frequency sweep for Raman sideband cooling at the initial turn-on of the lattice. More discussions on the Raman sideband cooling will take place in chapter 6.

Pinning of atoms

Knowing the band structure of the lattices, we can now estimate how the wavefunction of an atom is loaded into the energy bands during pinning. A program written by Bruno Peaudecerf calculates the projection of a Gaussian wavepacket onto the Wannier functions corresponding to the lowest bands. The width σ of the wave packet is taken as the correlation length, which is typically also the inter-partical spacing $\sigma \approx k_F^{-1} \approx n^{-\frac{1}{3}}$. This gives $\sigma/d \approx 2.6$, using $d = \dfrac{\lambda}{\sqrt{2}}$ based on the Z-lattice spacing. The result in figure 5.12 shows that all the even-number trapped band are occupied. The occupation probability does not decrease with the band number, although the lowest band being slightly more favored. This distribution is insensitive to the off-centering of the wave packet from the trap center

(subfigure (a)∼(c)). If the wavepacket carries a momentum on the order of k_F (subfigure (d)∼(f)), the overall occupation probability is not significantly modified, except that odd-number bands are also filled now. For an even broader wave packet, the band occupation remains similar.

Since plenty of higher bands will be populated, some atoms may in fact tunnel out of their initial positions, unless we manage to cool them down efficiently and quickly. However, because the way that atoms are projected in the bands does not very much depend on their initial position, the loss of atoms from higher bands is unlikely to distort the overall spatial distribution. By summing the projection on all the Wannier states within a lattice site, the projection probability against site vicinity is calculated. The result in subfigure (g) shows that the total weight on each site follows a Gaussian distribution. One-sigma width of this distribution roughly corresponds to the central 5 sites around the atom. Given this span and the diluteness of the cloud, the tunneling events mentioned above will be tolerable. Finally, as we will show in the later chapter 4.1, the point spread function of the atom fluorescence is on the same order of the lattice spacing, and will not limit the precision of the reconstructed atom distribution. Therefore, our planned pinning protocol seems promising to render the initial atom positions with good fidelity.

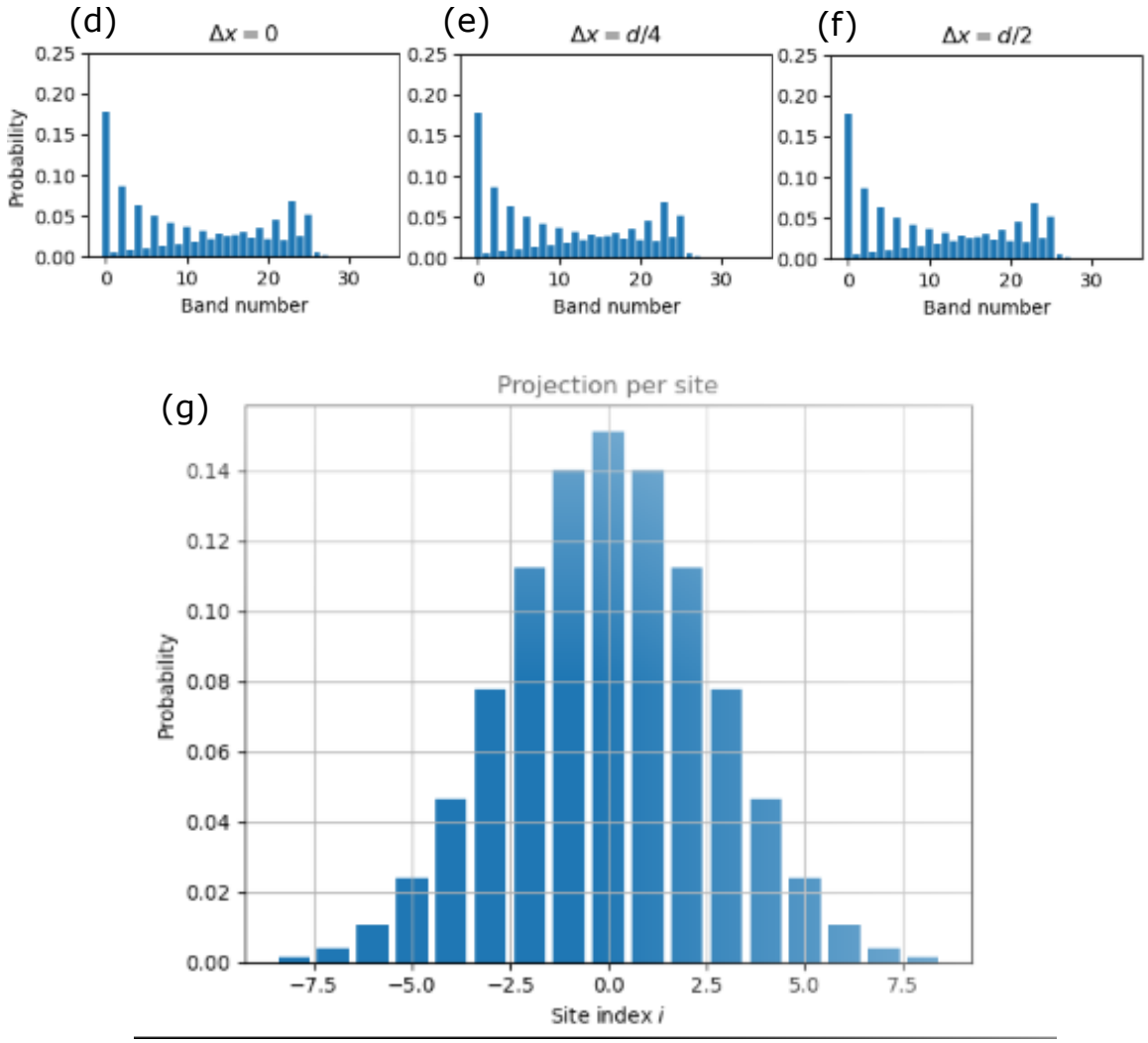

Figure 5.12: Projection of a Gaussian wave packet onto the lattice Wannier states. (a-c) Occupation number versus band index for a static wave packet, with various position offset Δx from the trap center. (d-f) Occupation number for a moving wave packet carrying momentum $k \sim k_F$. (g) Summing over the occupation number within each lattice site, the wave packet is normally distributed over several lattice sites, with a width of roughly 5 sites.

CHAPTER 6
TOWARD SINGLE ATOM IMAGING

Atoms in the pinning lattice are subjected to heating effects from lattice intensity noise and from photon scattering. To keep atoms at lower vibrational levels in the lattice sites, two-photon cooling techniques are used. The most common methods are EIT cooling [145, 146] and Raman sideband cooling [79, 78, 77]. In this chapter we describe the scheme and setup for the Raman sideband cooling in our experiment. The Raman two photon transition has been tested in the lattice. The obtained spectrum shows clearly resolved sidebands and provides an additional confirmation on our previous lattice calibrations. We have also observed promising images of atom fluorescence.

6.1 Cooling scheme

Figure 6.1 shows the level diagram for Raman sideband cooling: Two lasers are used to couple two target ground states — $|g_1\rangle$ in the $F = 1/2$ manifold and $|g_2\rangle$ in the $F = 3/2$ manifold, via a virtual excited state that is never populated during this two-photon process. Both Raman beams are chosen to be $5.5\,\mathrm{GHz}$ red detuned from the D_1 line. Their frequency difference matches the Zeeman splitting between $|g_1\rangle$ and $|g_2\rangle$, minus a vibrational sideband frequency of the lattice. The decomposition of $|g_1\rangle$ and $|g_2\rangle$ into the "good" basis of Zeeman states will depend on the magnetic field, as seen in the Breit-Rabi formula 1.1, and on the polarizations of the two Raman beams, which determines the allowed angular momentum addition during this two-photon process. We have chosen to use π and σ_- polarizations on Raman beams 1 & 2 respectively, they will coherently drive an oscillation between n^{th} vibrational state of $|g_1\rangle$ internal state and the $n-1^{\text{th}}$ vibrational state of $|g_2\rangle$, with a +1 change in the magnetic quantum number. A repumper in resonance with D_1 line brings back the atom in $|g_2\rangle$ to the excited state $|p\rangle$, so that effectively the Raman coupling preferably drives transitions from $|g_1\rangle$ to $|g_2\rangle$. When the atom decays from the excited state, its internal state goes back to $|g_1\rangle$ or $|g_2\rangle$ according to the braching ratio, which is $4/9$ and $5/9$ at zero magnetic field. The vibrational state remains in $n-1$ since single photon recoil energy is small compared to the lattice trapping frequency. When the atom eventually goes back to $|g_1\rangle$, one Raman cycle is completed and the vibrational level has gone down by one. Given the numerical aperture of the microscope objective, the photons released in the spontaneous decay from $|p\rangle$ have a 8.2% chance to be collected,

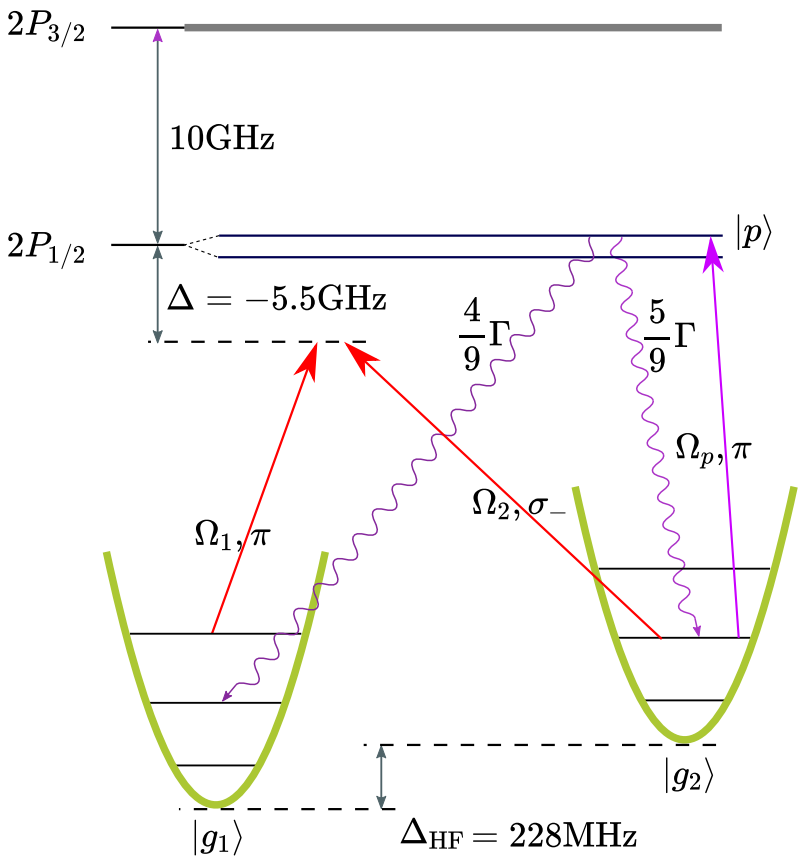

Figure 6.1: Level diagram of Raman sideband cooling. Raman beams Ω_1 and Ω_2 (with π and σ_- polarization respectively) induce two-photon transition from $|g_1, n\rangle$ to $|g_2\rangle, n-1$. The repumper recycles the transition and spontaneous decay from $|p\rangle$ back to either ground state provides photons for fluorescence imaging.

thereby contribute to the fluorescence imaging of the atoms in-situ.

Although we currently perform Raman sideband cooling at zero field, the cooling scheme described above is also valid under strong magnetic field with some adjustments.

6.2 Laser setup

6.2.1 Laser source preparation

Figure 6.2 shows the laser table for the two Raman beams. The two beams are generated from a single ECDL source amplified by a TA. The output of the TA is split and passed through two acoustic optical modulators (AOM) to keep the two Raman beams in coherence. Currently the Raman 1 & 2 are shifted by +131.2 MHz and -97 MHz respectively

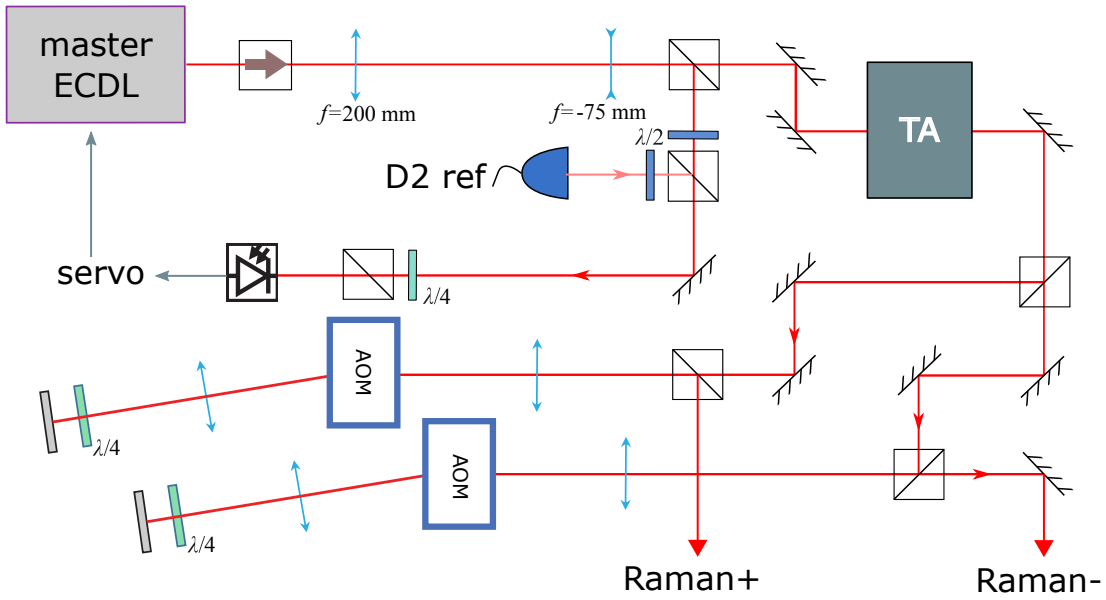

Figure 6.2: Laser source for Raman sideband cooling.

from the master frequency, The relative laser detuning between them thus is controlled at 228.2 MHz with sub kHz precision, which is suitable for Raman transition under a well cancelled magnetic field. The AOMs also allow an accurate and fast control over the detuning to match the sideband frequency. In addition, frequency modulations can easily be applied on the AOMs in case there is a need to compensate for anharmonicity of the trap. In the future it will be possible to perform Raman sideband cooling also under high magnetic field, by keeping the same optics and only substituting the AOMs to models giving larger frequency shifts[a].

The overal detuning Δ with respect to D_1 line is less crucial for the performance of the Raman cooling and we have chosen to park at -5.5 GHz offset from the D_1 line. This choice is to a large part arbitrary, but is in line with three considerations — Firstly the detuning should be large enough from an atomic line to reduce off-resonance scattering from each single Raman beam which heats up the cloud; Secondly the detuning cannot be too large compare to the fine structure splitting, which must remain resolved for Raman transitions to happen with a reasonable probability. Thirdly, we avoided shining light on the D_2 transition in order to reduce tensor Stark shifts. This frequency offset lock uses the same side-of-filter method [97] as we have used for the high field imaging light earlier in section 1.2.2. The offset frequency is controlled by a local RF source[b]. This offset lock is

[a] for example, AOM model BRI-GPF-650 under double pass can provide 2.5 GHz detuning between Raman + and -, which is enough for Raman cooling under 832 Gauss.

[b] DS instrument SG6600L

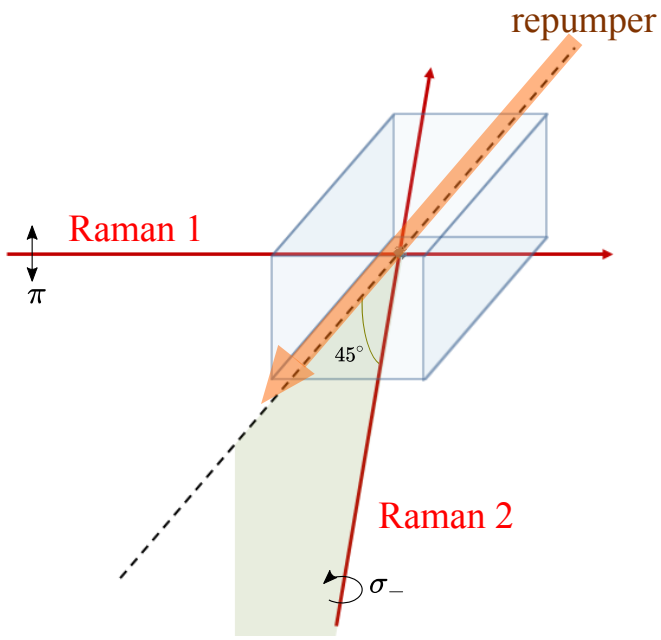

Figure 6.3: Orientations of the Raman beams and the repumper beam

able to stabilize Δ below 5 MHz and prevents day-to-day drifts.

The master laser uses a 15 mW 671 nm laser diode installed on a homemade mount. A tapered amplifier is added to get enough power on each of the Raman beams, typically 7 mW for Raman 1 and 3.5 mW for Raman 2 after fibers. Raman 1 has a beam waist of 420 μm on the atoms, which leads to a max intensity $I_1 \approx 2.52\,\mathrm{W/cm^2} = 990\,I_{\mathrm{sat}}(D_2)$. Raman 2 has a beam waist of 280 μm on the atoms, giving $I_2 \approx 2.8\,\mathrm{W/cm^2} = 1120\,I_{\mathrm{sat}}(D_2)$. The repumper is on D_1 line, and requires only hundreds of microwatt power. It is directly taken from a branch on the D_1 laser table.

6.2.2 Laser orientations

The geometry of the Raman lasers is depicted in figure 6.3. Raman 1 shines from the side of the cell, and shares the same axis as the cell transverse imaging light (as in fig 1.8). Its polarization is linear in the vertical direction, driving π transitions in the magnetic field of the coils. Raman 2 is overlapped onto the upcoming arm of the Z-lattice using a dichroic mirror, and intended to have an anti-clockwise circular polarization to drive σ_- transitions. Nonetheless, the polarization is not as well controlled on Raman 2 because it is last reflected at a 22.5° incident angle on a 45° mirror, which introduces ellipticity. Still, overlapping the Raman 2 with the Z-lattice turned out to have some practical advantages. By collecting the transmitted red Raman 2 light on a camera behind a Z-lattice mirror above the cell

(see figure 5.1), we could regulate its orientation to prevent day-to-day drifts. On the same camera, pre-alignment of the Raman 2 beam was done by creating an absorption image of the atoms while sending a resonant light through the Raman 2 fiber.

The repumper is shined within the horizontal plane due to two main concerns — Firstly our triangular lattice is deeper than the vertical 1D lattice, it is therefore favorable to keep the repumper light wave vector also in the horizontal plane. Secondly this beam orientation leaks less stray light into the microscope objective.

6.3 Estimated cooling rate

6.3.1 Raman coupling strength

The coupling created by two Raman beams can be modeled by a three level system in Λ-type configuration, involving the two ground levels $|g_1\rangle$ and $|g_2\rangle$, and an intermediate excited level $|e\rangle$. Since both the Raman beams are far detuned by Δ from the excited level, it does not get populated during the Raman transition. The hamiltonian for this three-level system can be written as

$$\hat{H} = \frac{\hbar}{2}\begin{pmatrix} E_e & \frac{\hbar\Omega_2^*}{2}e^{-i\omega_{L_2}t} & \frac{\hbar\Omega_1^*}{2}e^{-i\omega_{L_2}t} \\ \frac{\hbar\Omega_2}{2}e^{-i\omega_{L_2}t} & E_{g_2} & 0 \\ \frac{\hbar\Omega_1}{2}e^{-i\omega_{L_1}t} & 0 & E_{g_1} \end{pmatrix}.$$

The detuning of each Raman laser can be denoted as $\Delta_1 = \omega_{L_1} - \frac{1}{\hbar}(E_e - E_{g_1})$, $\Delta_2 = \omega_{L_2} - \frac{1}{\hbar}(E_e - E_{g_2})$. But it is more convenient to work with the global detuning $\Delta = \frac{\Delta_1 + \Delta_2}{2}$ and the two-photon detuning $\delta = \Delta_2 - \Delta_1 = \omega_{L_2} - \omega_{L_1} + \Delta_{\text{HF}}$, where Δ_{HF} is the hyperfine splitting between the two ground levels, as shown in figure 6.1.

Under such notation, and assuming that population changes in the excited state $|e\rangle$ is always slow compared to the dynamics in the ground states, also known as the adiabatic elimination, the three level system can be simplified to a two level system. In the dressed states basis which is to first order the basis $|g_1\rangle$ and $|g_2\rangle$, its hamiltonian is [147]:

$$H_{I,\text{Raman}} = \frac{\hbar}{2}\begin{pmatrix} -\delta + \frac{|\Omega_2|^2}{2\Delta} & \frac{\Omega_1^*\Omega_2}{2\Delta} \\ \frac{\Omega_1^*\Omega_2}{2\Delta} & \delta + \frac{|\Omega_1|^2}{2\Delta} \end{pmatrix} = \frac{\hbar(|\Omega_1|^2 + |\Omega_2|^2)}{8\Delta}\mathbb{1} + \begin{pmatrix} -\Delta_R & \Omega_R^* \\ \Omega_R & \Delta_R \end{pmatrix}. \quad (6.1)$$

Here $\mathbb{1}$ is the identity matrix, and we have defined the Raman coupling strength $\Omega_R =$

$\frac{\Omega_2^*\Omega_1}{2\Delta}$, and the "effective Raman detuning" $\Delta_R = \delta + \frac{|\Omega_1|^2 - |\Omega_2|^2}{4\Delta}$. This effective detuning can be seen as subtracting the light shift on $|g_1\rangle$ caused by Ω_1 and the light shift on $|g_2\rangle$ caused by Ω_2, compensated by the two photon detuning δ. In the experiment, it could be fully compensated by adjusting δ. Then the Raman Rabi frequency is maximized to $\Omega_{\text{Rabi}} = \Omega_R$.

From the expression of Ω_R, it is clear that the coupling strength scales as the geometric mean intensity of the two Raman beams. On top of this, if we consider realistic situations, the dipole matrix element products contain contributions from both the motional degrees of freedom and the internal degrees of freedom. The former gives the lamb-Dicke parameter and the latter is an angular momentum addition depending on the virtual excited state. Considering a transition from vibrational number m to n, and multiple excited states $|e\rangle$, the Raman frequency may be written as:

$$\begin{aligned}\Omega_R \propto & \frac{\sqrt{I_1 I_2}}{\hbar^2} \langle g_2, n| \, e^{-i\mathbf{k_2}\cdot\hat{\mathbf{x}}} \hat{\epsilon_2}\cdot\hat{\mu} \left(\sum_{e,m'} |e,m'\rangle\langle e,m'| \right) e^{i\mathbf{k_1}\cdot\hat{\mathbf{x}}} \hat{\epsilon_1}\cdot\hat{\mu} \, |g_1, m\rangle \\ \propto & \sqrt{I_1 I_2} \, \langle n| \, e^{i\Delta\mathbf{k}\cdot\hat{\mathbf{x}}} \, |m\rangle \sum_e \langle g_2| \, \hat{\epsilon_2}\cdot\hat{\mu} \, |e\rangle\langle e| \, \hat{\epsilon_1}\cdot\hat{\mu} \, |g_1\rangle .\end{aligned} \tag{6.2}$$

Lamb-Dicke parameter

The Lamb-Dicke parameter is defined as the square root of the ratio between the recoil energy in the two photon process to the level spacing in the harmonic trap:

$$\eta_x = \sqrt{\frac{E_r}{\hbar\omega_{\text{tr}}}} = \sqrt{\frac{\hbar(\Delta\mathbf{k}\cdot\hat{\mathbf{x}})^2}{2m\omega_{\text{tr}}}} = |\Delta k_x| x_0, \tag{6.3}$$

where x_0 is the harmonic oscillator length. The Lamb-Dicke parameter (along one vibrational axis) arises when expanding the spatial term in the dipole matrix element in terms of ladder operators

$$\begin{aligned}\langle n| \, e^{i\Delta\mathbf{k}\cdot\hat{\mathbf{x}}} \, |m\rangle &\approx \langle n| \, 1 + i\Delta k_x x_0 (\hat{a} + \hat{a}^\dagger) \, |m\rangle \\ &= \delta_{n,m} + i\eta_x\sqrt{m}\delta_{n,m-1} + i\eta_x\sqrt{m+1}\delta_{n,m+1}.\end{aligned} \tag{6.4}$$

When $\eta_x \ll 1$, transitions that changes the vibrational mode by more than one are strongly suppressed.

Based on the previous lattice calibrations, the lattice frequency we will be able to obtain with 35 W XY-lattice power is around 1 MHz. Considering the angle between the

two Raman beams, the momentum kick in a two-photon process is $|\Delta k| = \sqrt{2}k_0 = \frac{2\sqrt{2}\pi}{\lambda}$ giving the Lamb-Dicke parameters along three directions respectively as $\eta_{\{x,y,z\}} = \{0.27, 0.19, 0.19\}$, and their geometric mean is $\bar{\eta} \approx 0.21$. The width of the sideband for about one quantum of vibration is $\eta\Omega$, which is small compared to the trapping frequency. We can expect to obtain a well resolved Raman spectrum, which is displayed in the following section 6.4.

Matrix element

To calculate the Raman coupling strength, contributions from all possible intermediate excited level are summed. Given the two ground states and the polarization of the Raman beams, we see that in ^{6}Li case there is one allowed two-photon coupling via $2P_{3/2}$ and one via $2P_{1/2}$. Eventually the carrier Raman coupling strength can be written as

$$\begin{aligned}\Omega_{R,\text{carrier}} &= \kappa\frac{\Omega_1^*\Omega_2}{2}\left(\frac{1}{\Delta_{1/2}} - \frac{1}{\Delta_{3/2}}\right) \\ &= \kappa\frac{3\pi c^2\Gamma}{\hbar\omega^3}\sqrt{I_{\sigma_-}I_\pi}\left(\frac{1}{\Delta_{1/2}} - \frac{1}{\Delta_{3/2}}\right),\end{aligned} \tag{6.5}$$

where $\Delta_{1/2}$, $\Delta_{3/2}$ are respectively the global detuning with respect to $2P_{1/2}$ and $2P_{3/2}$ fine structures, and differ by 10 GHz fine structure splitting. κ comes from the Clebsch-Gordan coefficient in the dipole transitions. At high magnetic field (Paschen-Back regime), one can directly work with m_j basis [c] and find $\kappa = -\frac{\sqrt{2}}{3}$. Whereas under zero magnetic field, Raman transition $|F = \frac{1}{2}, m_F = -\frac{1}{2}\rangle \leftrightarrow |F = \frac{3}{2}, m_F = \frac{1}{2}\rangle$ occurs simultaneously with transition $|F = \frac{1}{2}, m_F = \frac{1}{2}\rangle \leftrightarrow |F = \frac{3}{2}, m_F = \frac{3}{2}\rangle$. The overall κ is $\frac{2+2\sqrt{3}}{9} \approx 0.61$.

The actual Raman beam powers I_{σ_-}, I_π projecting on the correct polarization under the atom quantization axis is smaller than the full beam power I_1, I_2. At zero magnetic field the basis is not well defined, for a rough estimate we assume vertical quantization axis, which leads to a projection factor $I_{\sigma_-} = 75\%I_2$ for the desired polarization.

6.3.2 Estimated photon count

In order to estimate the repumper intensity needed and the fluorescence photon number we can get, we made a numerical simulation on the dynamics between three atomic levels —

[c] e.g. $|g_1\rangle \xrightarrow{\pi} |L = 1, m_L = 0, S = \frac{1}{2}, m_s = -\frac{1}{2}\rangle = \sqrt{\frac{2}{3}}|\frac{3}{2}, -\frac{1}{2}\rangle + \sqrt{\frac{1}{3}}|\frac{1}{2}, -\frac{1}{2}\rangle$

$|g_2\rangle \xrightarrow{\sigma_-} |L = 1, m_L = -1, S = \frac{1}{2}, m_s = \frac{1}{2}\rangle = \sqrt{\frac{1}{3}}|\frac{3}{2}, -\frac{1}{2}\rangle - \sqrt{\frac{2}{3}}|\frac{1}{2}, -\frac{1}{2}\rangle$

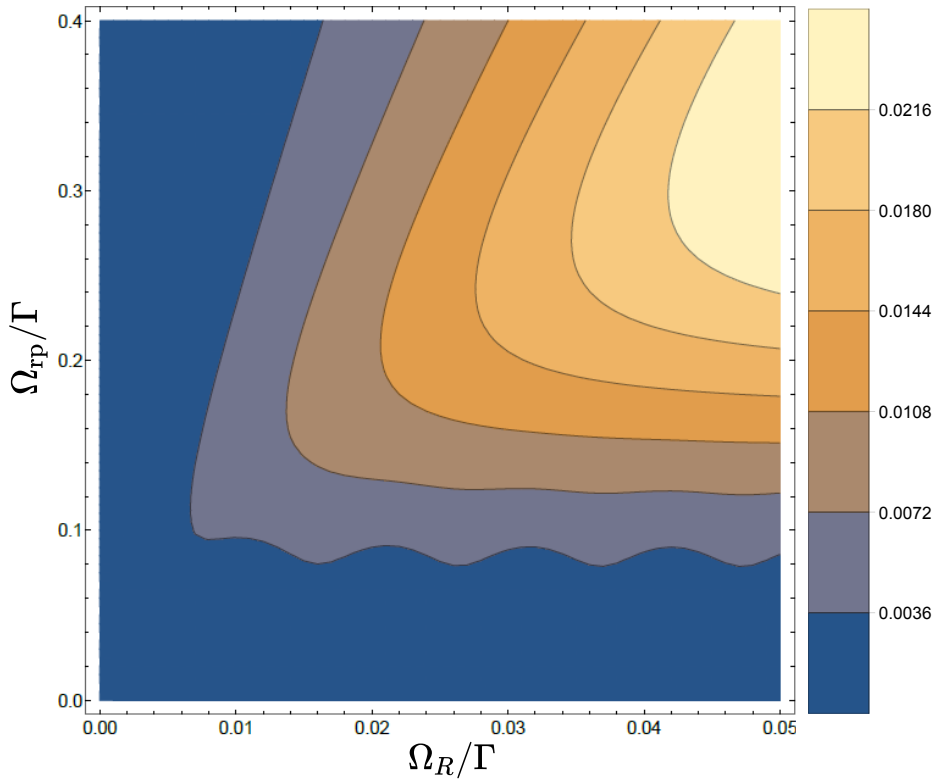

Figure 6.4: A numerical solution for the three level system consisting of Raman ground states $|g_1\rangle$, $|g_2\rangle$ and the excited level for optical pumping $|p\rangle$. The coupling between $|g_1\rangle$ and $|g_2\rangle$ is simplified to a coherent driving with strength Ω_R, the Raman Rabi frequency. $|g_2\rangle$ and $|p\rangle$ are coupled by the repumper with strength $\Omega_{\rm rp}$. The contour plot shows the steady state occupation number in $|p\rangle$. From which we estimated the fluorescence photon emission rate.

the two Raman ground states $|g_1\rangle$, $|g_2\rangle$ and the excited level for optical pumping $|p\rangle$. The effect of the Raman beams are further simplified to a single coherent driving with coupling strength Ω_R. The repumper couples state $|g_2\rangle$ to $|p\rangle$ with strength $\Omega_{\rm rp}$. Assuming both drivings to be on resonance by careful tuning the Raman and repumper frequencies, and taking the branching ratio of spontaneous decay to $|g_1\rangle$, $|g_2\rangle$ to be $\frac{4}{9}$, $\frac{5}{9}$ respectively, we plot the steady state solution of the excited state occupation number as a function of Ω_R and $\Omega_{\rm rp}$ in figure 6.4. For a rough estimate[d] we take the Raman Rabi frequency to be $\Omega_R = 0.025\,\Gamma$. There seems to be an optimal repumper power around $\Omega_{\rm rp} = 0.2\,\Gamma$ or $I_{\rm rp} = 0.08\,I_{\rm sat}$. And the fluorescence photon emission rate can be expected to reach $0.01\,\Gamma = 3.7 \times 10^5\,{\rm s}^{-1}$ per atom, which is quite abundant.

[d] This estimate is based on the typical Raman power we have on each arm with the correct polarization $\Omega_1 = \Omega_2 \approx 20\,\Gamma$, plugged in to equation 6.5, multiplied by $\sqrt{2}\bar{\eta}$. The $\sqrt{2}$ here is assuming a red sideband transition from vibrational state m=2 to n=1.

Numerical aperture of the objective

The microscope objective has a numerical aperture 0.55, which corresponds to a half-angle of $\theta = 33^\circ$ for light collected from the object. The subtended solid angle is

$$\Omega_{\text{objective}} = \int_0^{2\pi} d\phi \int_0^{\theta} \sin\theta' d\theta' = 2\pi(1 - \cos\theta) = 1.036. \tag{6.6}$$

The fraction of photons collected is $\frac{1.036}{4\pi} = 8.2\%$. We have shown in chapter 4.2 that with the planned 55$\times$ magnification imaging scheme, a very good signal-to-noise ratio (>9 dB) can be obtained if 500 photons are collected from each atom. Under the ideal scenario of $3.7 \times 10^5\,\text{s}^{-1}$ photons per atom, this condition can be easily met within 20 ms exposure time.

6.4 Raman sideband cooling result

Measured Rabi frequency

We calibrate the Raman carrier transition rate by detecting the Rabi oscillations on the atom number in the ground state $F = 3/2$ hyperfine manifold. The atoms are cooled and loaded into the lattice according to the aforementioned sequence, and the XY pinning lattice is ramped up to a final power 10 W for this measurement. During the magnetic field ramp-down, both spin states adiabatically go to the $F = 1/2$ manifold, which is seen as the $|g_1\rangle$ in the Raman scheme. We shine the two Raman lasers on simultaneously, with the Raman 2 laser AOM driver triggered in a burst mode. The length of the burst corresponds to the duration for which both Raman beams are present, and can be controlled at 100 ns precision. The resonance for the Raman transition is found when the two beams have 228.255 MHz frequency difference, which slightly deviates from the ground state hyperfine splitting 228.205 MHz. This discrepancy might comes from the Doppler effect due to the recoil of the atoms in the weakly confined Z-direction. An absorption imaging is then performed on the ground state $F = 3/2$ manifold, namely $|g_2\rangle$ in the Raman scheme. Scanning the Raman pulse duration, we observe a Rabi oscillations in the $|g_2\rangle$ population.

The measured Rabi carrier frequency is $2\pi \times 325$ kHz for 6.5 mW and 3.3 mW power on Raman 1 & 2, or equivalently for $\Omega_1 = \Omega_2 \approx 20\,\Gamma$. Our measured Raman Rabi frequency is on the same order of magnitude as the estimated Rabi frequency of 490 kHz based on equation 6.5.

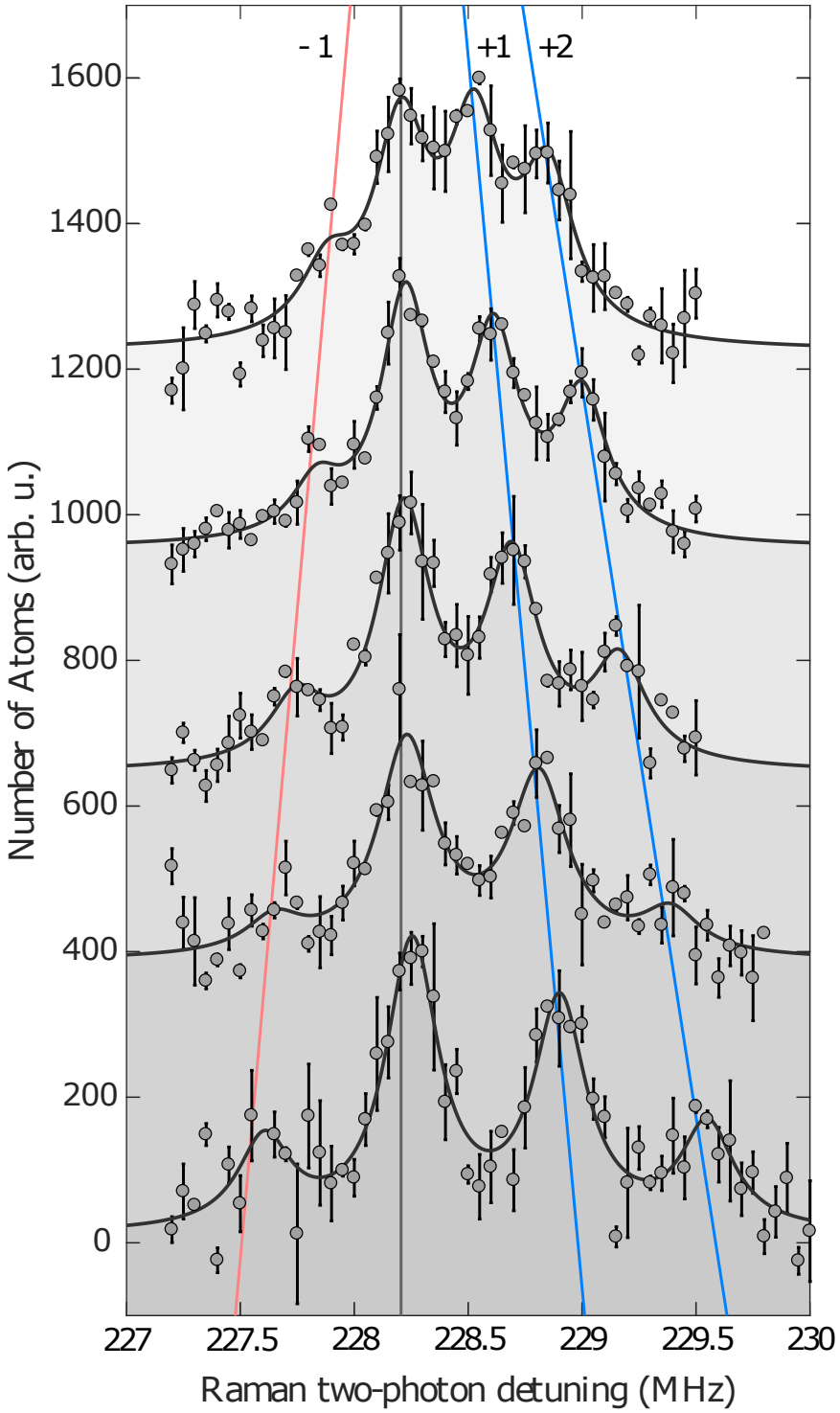

Figure 6.5: Spectrums of a scan on the Raman two-photon detuning δ on atoms trapped in XY-lattice. Gray dots and black curves show the atom count in $F = 3/2$ states and the fitted Lorentzians; Black vertical line at 228.2 MHz is the expected position for the carrier Raman frequency ignoring any light shift; Blue and red lines traces out the shift in sideband frequencies versus lattice power. From top to bottom, the spectra are taken at XY-lattice power 4 W, 6.5 W, 9.35 W, 11.7 W, and 15 W.

We have also checked that the off-resonance scattering rate of each single Raman beam is on the order of $2\pi \times 3\,\mathrm{kHz}$, much smaller than the Raman Rabi frequency. This ensures that the sideband cooling dominates and can keep the atoms in a low vibrational state during the collection of fluorescence photons.

Resolved sidebands

Using the above measured π time of the Raman pulse, the Raman cooling sidebands are observed in XY-lattice and in Z-lattice independently. In figure 6.5 we measure the atom number transferred from $F = 1/2$ to $F = 3/2$ via the Raman two-photon coupling, when the Raman two-photon detuning is scanned around the carrier frequency 228.2 MHz. The pulse duration is $1.5\,\mu$s, corresponding to a π-pulse on the carrier transition. A series of Raman spectra at various XY-lattice power ranging from 4 W to 15 W are shown. We can see clearly resolved red and blue sidebands. The sideband frequencies follows the $\sqrt{P}$ scaling law nicely for the selected XY-lattice power. This serves as a confirmation on the previously calibrated lattice frequency based on lattice modulation in section 5.2.2. Similar measurements are done for the Z-lattice at two lattice powers 12 W and 25.5 W.

First fluorescence signal

With the Raman beams well characterized, we have also tried to test the performance of the Raman cooling and check the photon collection rate by turning on the repumper simultaneously. Firstly a measurement is done on the whole cloud using a low magnification of 5.6 for the imaging system. The Raman two-photon detuning is fixed on the peak of the red sideband, the fluorescence from the whole cloud is collected for various cooling durations ranging from tens of milliseconds to several seconds. In addition, an absorption image is also taken at the end of each cooling duration to count the atom number left. In figure 6.6(a), the fluorescence photon collection rate against number of atoms left is plotted in a scatter plot, from which we estimate 10^5 photons/atom/s emission rate from the Raman sideband cooling process. This is on the same order of magnitude as our previous estimate in section 6.3.2.

Another measurement on the atom lifetime inside the pinning lattices with or without the presence of Raman cooling beams confirms the effectiveness of our Raman sideband cooling. Figure 6.6(b) shows that Raman cooling is capable of extending the atoms lifetime by more than a factor of 100, keeping the atoms in the lattice for more than 7 seconds.

Finally after switching to the higher magnification of 55 times on the imaging system, we have obtained a raw image of single atoms in the center of the pinning lattice, as seen

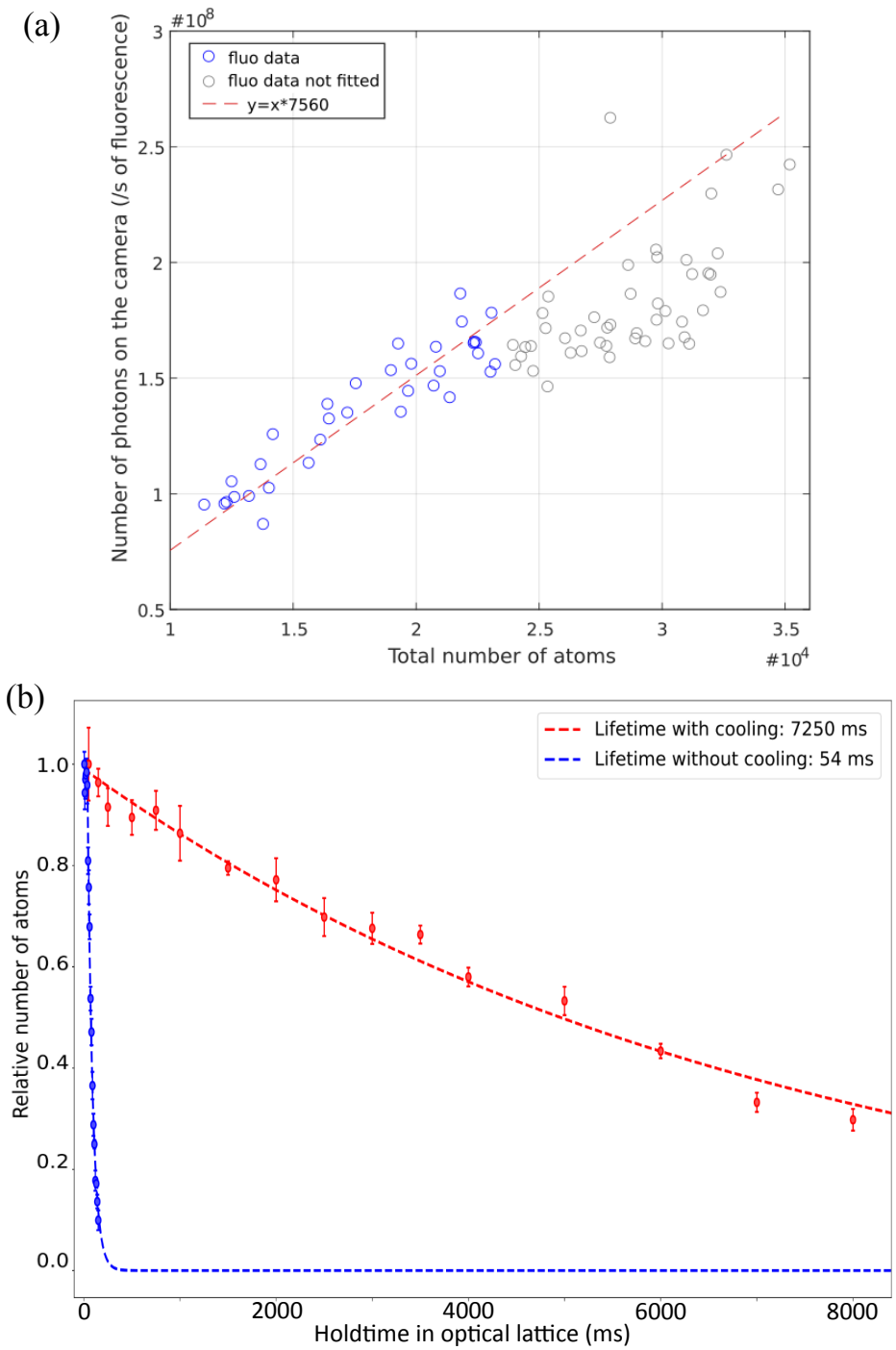

Figure 6.6: (a) Raman fluorescence photon rate after various cooling time, plotted against the corresponding atom number at the end of the cooling process. The linear fit extracts the photon emission rate per atom per second. (b) Lifetime of the atoms inside pinning lattices is significantly extended from 50 ms to 7200 ms by applying Raman sideband cooling.

in figure 6.7. Already from this preliminary result, traces of single-atom-like fluorescence spots can be recognized. The quality of such a single-atom image can potentially be improved significantly after reducing stray lights from the background or from atoms outside the focal plane. This can be achieved by optically blowing away atoms in off-focused lattice planes with the help of a magnetic gradient and RF pulses.

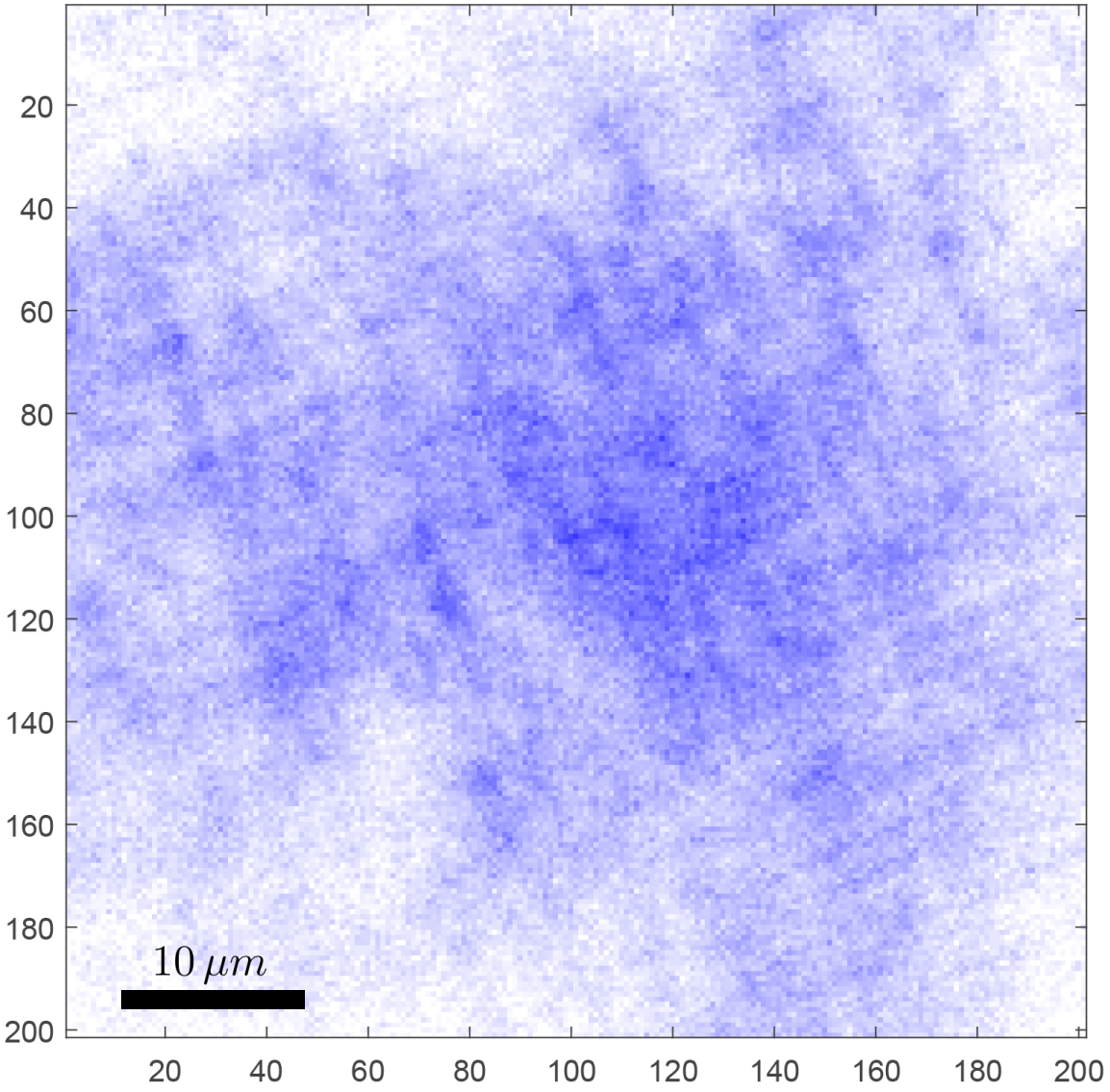

Figure 6.7: An example of the single-atom fluorescence image within 500 ms exposure time. The cloud is first released to expand for 10 ms, and then recaptured by the pinning lattice for fluorescence imaging.

CONCLUSION

This thesis has presented the design and performance of our new quantum simulation setup based on ^{6}Li atoms, with which we are able to obtain degenerate Fermi gas under the strongly-interacting regime, having a temperature well below the superfluid transition temperature. The capability of obtaining single-atom resolved images through quantum gas microscopy is ready to be demonstrated.

In chapter 1 and 2 we have explained the overall structure of our setup and quantitatively assessed the performance of the laser cooling in the MOT chamber. The MOT loading and gray molasses cooling are both fast and effective, giving us a cloud containing several 10^8 atoms at 50 μK within the first 2 s of the experiment sequence. The optical setup for two high power infrared lasers were illustrated, one of them can transport the atoms cloud optically with an efficiency as high as 97%, and bring them to the science cell with a wide optical access. The second IR laser provides extra confinement for the cloud there and helps to increase the opposite-spin collision rate by 70 times. The imbalance in the spin populations can be reliably controlled by a non-adiabatic RF sweep. The sweeping speed has been well calibrated at a magnetic field of 832 G. Before further evaporation in the crossed dipole trap, we can typically have 3×10^5 atoms in each spin, with a collision rate of $3.8 \times 10^4\,\mathrm{s}^{-1}$.

In chapter 3 the evaporative cooling sequence and result are presented. We adapted a thermometry method based on the equation of states of a unitary Fermi gas in a harmonic trap, which can be directly extracted from the cloud's doubly integrated profile. Using this thermometry, we report a final temperature of 17 nK and $T/T_F = 0.076$ at the end of evaporation, much lower than the superfluid transition temperature $T_c/T_F = 0.176$ at unitarity. An extra evidence of superfluidity was given by the direct observation of the "superfluid plateau" in a spin imbalanced cloud.

In chapter 4, the high-resolution imaging setup is explained. The microscope objective gives a resolution of 750 nm under actual working condition for 671 nm imaging wavelength. Through simulations of the fluorescence picture, we chose to use 55.6$\times$ magnification for the single-atom imaging, which both save enough sampling points for each atom's PSF, and allows for a high signal-to-noise ratio. An alternative lower magnification of 5.6 is also setup, giving a suitable field of view for the preliminary measurements in the lattice.

In chapter 5 we have shown the geometry of the 2D triangular lattice in the horizontal plane and the 1D vertical lattice. Both lattices have been carefully characterized using para-

metric heating effects from controlled modulations on the lattice laser amplitude/frequency. The lattice periodicity and its first Brillouin zone are revealed by Kapitza-Dirac scattering and band mapping respectively. Using numerical calculations on the band structure, we have evaluated that each atom can be reliably pinned on lattice sites at its vicinity.

Finally, in chapter 6 the Raman sideband cooling scheme is explained. Two-photon transitions induced by a pair of Raman beams have been observed. While scanning the two-photon detuning, we have obtained spectra showing transitions at the carrier frequency and at numerous blue and red sidebands. The sideband frequencies measured this way agree with the earlier lattice calibration very well. With the presence of a repumper light, a cooling effect is clearly seen on the red sideband, where more photons are collected when holding atoms in the lattice. The quantum gas microscope is now ready to start taking our first fluorescence images.

Possible upgrades on the experiment

Although we have achieved on our setup a stable and fast operation that routinely produces a degenerate Fermi gas, there are modifications that can be carried out to simplify the sequence significantly or to bring further improvements on the stability.

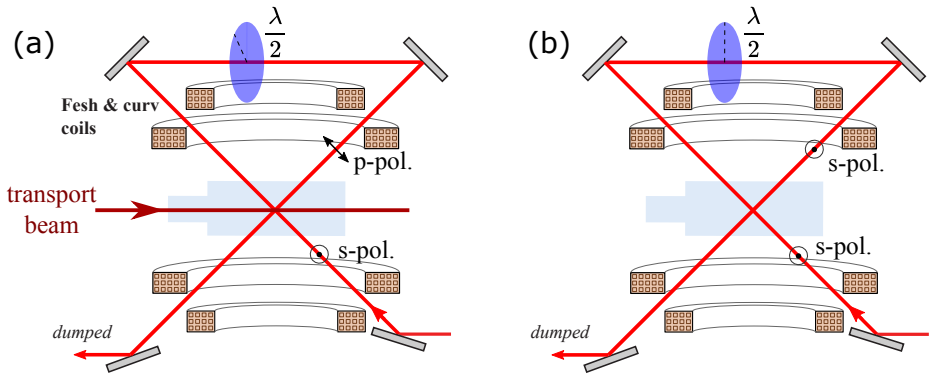

Figure 7.1: A possible modification on the Z-lattice, where a half-wave plate is placed between the two lattice arms, to control the depth of interference. (a) During evaporation, the polarization of the reflected lattice arm is rotated 90° with respect to the incoming lattice arm. There is no interference where the beams cross. (b) After evaporation, the Z-lattice is ramped up by turning the waveplate, to align the polarizations of the lattice arms.

Evaporation sequence

The sequence can be greatly simplified if the final steps of the evaporation can be done in the Z-lattice instead of in the cross dipole beam. This modification can be realized

by adding a similar intensity PID control circuit on the Z-lattice as we used for the cross dipole beam, plus a half-wave plate on a rotational mount in between the two Z-lattice arms. By motorizing the half-wave plate angle one can control the depth of interference for the Z-lattice, keeping it non-interfering during the evaporation and fully interfering during pinning. Such change will have two advantages — Firstly the cross dipole beam can be taken out to give more optical access around the cell, and the control sequence for the evaporation will be simplified; Secondly the collision rate in the later evaporation steps will be higher and the evaporation duration can be shortened.

Gravity compensation

In the future implementations, our setup should be able to simulate fermions in free space following a single equation of state. This relies on creating a homogeneous potential using repulsive dipole force. We have prepared a 532 nm green light field with linear intensity gradient along the vertical direction. This provides a constant upward force that can compensate for gravity. The beam intensity is tailored by a digital micromirror device (DMD). A real-time feedback program controls the micromirror positions to produce the tailored linear potential. The performance of this servo system has been tested on a side setup by Tim de Jongh. More details about this setup are shown in appendix D. To integrate this setup on the main experiment, we can shine the green laser along the transverse imaging axis with the help of dichroic mirrors as planned in figure 1.8.

Outlooks

Here we suggest several research subjects that can be studied on our machine in the near future.

Spatial dependence of correlations

As discussed in the introduction, our understanding on the correlations in the BEC-BCS crossover, especially near unitarity, is still insufficient. In overall, there is a lack of both theoretical models and direct experimental measurements on the onset of strong correlations as the temperature of the system is lowered. Some of the latest progress in characterizing the correlations at unitarity relies on probing the contact C, and revealed a sudden increase in C across the normal-to-superfluid transition [58, 60]. However the change is only 30% from the high temperature ($T \sim T_F$) normal phase to the deep superfluid regime, not fully reflecting the building up of the correlations. After all, the contact C is only a par-

tial measurement on the second order density-density correlation $g^{(2)}(r) = \langle n_\uparrow(0) n_\downarrow(r) \rangle$ at its short-range limit.

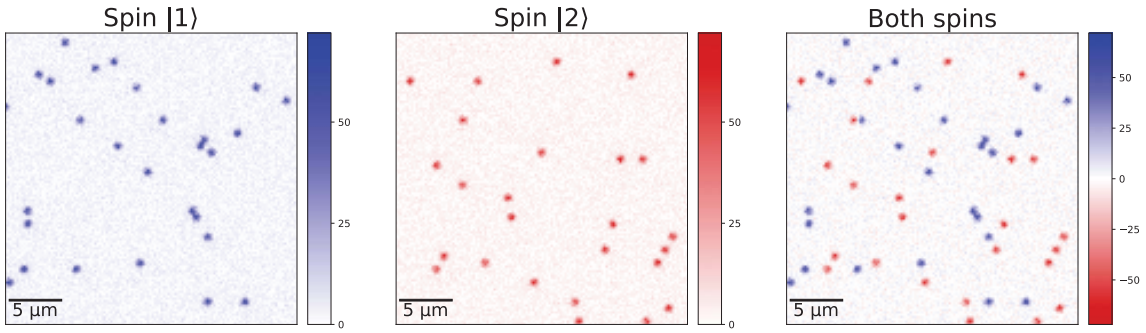

Figure 7.2: Spin-resolved single-atom fluorescence images (Simulation). Distribution of each spin component in a homogenous cloud will be detected non-destructively from the fluorescence of Raman sideband cooling. Each bright spot in this simulation signals the presence of an atom with a fidelity >99%. Reprinted from [136]

With a quantum gas microscope, however, we can aim to access density correlation functions at any order, beyond the short range behavior. In addition, with carefully designed Raman cooling scheme that works independently for each spin state (as suggested in section 6.1), our machine has the potential to yield spin-resolved fluorescence images, contemplated to look like figure 7.2. This will give us extra freedom in playing with the spin-imbalance of the system, and extracting both the single-spin correlations $g_{\uparrow\uparrow}, g_{\downarrow\downarrow}$, and the inter-spin correlations $g_{\uparrow\downarrow}$. This opens up many interesting directions, one of them being the study of Fermi polarons.

A Fermi polaron can be created for example by flipping the spin of one atom within a spin-polarized Fermi sea. This spin impurity dressed by the majority spins around it forms a quasiparticle — a Fermi polaron. Earlier studies [148] have measured contact in such highly spin-imbalanced clouds. Our quantum gas microscope image will be a good complement to the existing results by providing more information on the spatial variation of the correlation. The change in correlations as a function of the spin imbalance can also be explored.

Critical temperature and dynamics

Another of our research interests is the critical temperature T_c for the normal to superfluid transition. Previously, T_c has only been measured at unitarity [50, 51]. There is no concensus about the exact trace of the T_c line elsewhere throughout the BEC-BCS crossover even for spin-balanced Fermi gases.

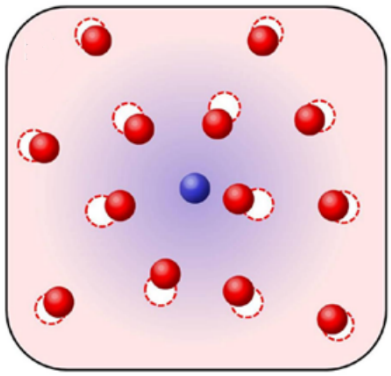

Figure 7.3: An illustration of a Fermi polaron, realized by making a spin $|\downarrow\rangle$ impurity in a Fermi sea of $|\uparrow\rangle$. Reprinted from [149].

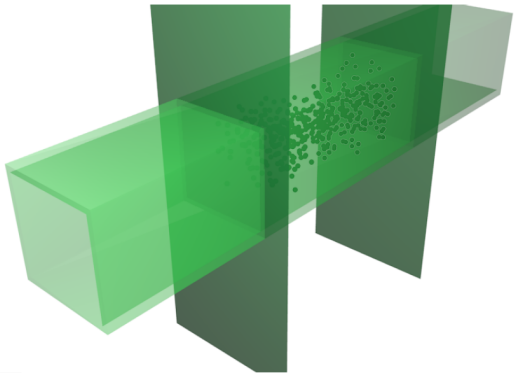

Figure 7.4: 3D render of a box potential. Reprinted from [91]

Finding the critical temperature of an atomic cloud at unitarity relied on its universality, whereby the thermodynamic quantities of the cloud become functions of a single parameter T/T_F. The aforementioned works therefore conducted their measurements in an inhomogeneous potential and their methodology remained in the LDA framework. Moving away from unitarity, as a new interaction parameter $1/(k_F a)$ enters the equation of state. These methods break down or are at least severely complicated.

To generalize the T_c measurement throughout the crossover, we propose to work with a homogeneous potential enclosed by a light box, as illustrated by figure 7.4. At the superfluid transition, the onset of a long-range order coincides with a sharp zero-momentum peak in the momentum distribution of fermion pairs $n_p(k)$. Our strategy to reveal the pair momentum distribution is through the rapid-ramp technique, which was invented in JILA [42] and further developed at MIT [132, 150]. A rapid ramp in the magnetic field from the BCS side to the BEC side creates diatomic molecules from two fermions of opposite spins that were physically nearby. The molecules will have a momentum distribution $n_m(k)$ that is related to $n_p(k)$ before the ramp. The exact relation between $n_m(k)$ and $n_p(k)$ has not been demonstrated in any existing literatures. However, the recent progress from our colleague Felix Werner [151] will help us make this link.

Appendices

APPENDIX A
ELECTRIC DIPOLE FORCE ON A TWO-LEVEL ATOM

A textbook semi-classical approach on atom-light interaction considers a driving electric field of the form

$$\mathbf{E}(\mathbf{r},t) = \mathbf{E}_0(\mathbf{r})\cos(\phi(\mathbf{r}) - \omega t) = \frac{\mathbf{E}_0(\mathbf{r})}{2}\left[e^{i(\phi(\mathbf{r})-\omega t)} + c.c.\right]. \tag{A.1}$$

Dipole approximation assumes that the optical wavelength is large compare to the size of the atom and hence appear invariant to the spatial integral on the interaction Hamiltonian. Under this assumption, the dipole interaction can be expressed as[152]

$$\mathcal{H} = \hat{H}_0 + \hat{H}_1 = \hat{H}_0 - e\mathbf{r}\cdot\mathbf{E}(\mathbf{r},t). \tag{A.2}$$

The perturbation under dipole approximation has the form

$$\hat{H}_1 = \begin{pmatrix} \hbar\omega_0 & \frac{\langle e|\,\hat{\mu}\,|g\rangle\cdot\mathbf{E}_0(r)}{2}\left(e^{i(\phi(r)-\omega t)} + c.c.\right) \\ \frac{\langle g|\,\hat{\mu}\,|e\rangle\cdot\mathbf{E}_0(r)}{2}\left(e^{i(\phi(r)-\omega t)} + c.c.\right) & 0 \end{pmatrix}.$$

ω is the frequency of the driving field and $\hbar\omega_0$ is the energy difference between the two atomic levels. $\langle e|\,\hat{\mu}\,|g\rangle = -e\,\langle e|\,\hat{\mathbf{r}}\,|g\rangle$ is the dipole matrix element.

Performing an unitary transformation

$$|\tilde{\psi}\rangle = U\,|\psi_S\rangle = \begin{pmatrix} e^{i\omega t} & \\ & 1 \end{pmatrix}|\psi_S\rangle$$

to go into the "rotating frame", and use rotating wave approximation to drop out fast oscillating terms with frequency $\omega + \omega_0$, the interaction Hamiltonian transforms according to

$$\begin{aligned}\hat{H}_{\text{rot}} &= i\hbar(\partial_t U)U^\dagger + U\hat{H}_1U^\dagger \\ &= \frac{\hbar}{2}\begin{pmatrix} -2(\omega-\omega_0) & \frac{e^{i\phi(r)}\mathbf{E}_0(r)}{\hbar}\cdot\langle e|\,\hat{\mu}\,|g\rangle \\ \frac{e^{-i\phi(r)}\mathbf{E}_0(r)}{\hbar}\cdot\langle g|\,\hat{\mu}\,|e\rangle & 0 \end{pmatrix} = \frac{\hbar}{2}\begin{pmatrix} -2\Delta & \Omega \\ \Omega^* & 0 \end{pmatrix}.\end{aligned}$$

Here we have defined the coupling strength $\Omega = \dfrac{e^{i\phi(r)}\mathbf{E}_0(r)}{\hbar} \cdot \langle e|\,\hat{\mu}\,|g\rangle$ and the detuning $\Delta = \omega - \omega_0$.

In order to take into account the spontaneous decay, the dynamics of this two level system is described by its density matrix in the rotating frame

$$\partial_t \tilde{\rho} = -\frac{i}{\hbar}[\hat{H}_{\text{rot}}, \tilde{\rho}] + \hat{L}_{\{\tilde{\rho}\}},$$

where

$$\tilde{\rho} = \begin{pmatrix} \tilde{\rho}_{ee} & \tilde{\rho}_{eg} \\ \tilde{\rho}_{ge} & \tilde{\rho}_{gg} \end{pmatrix} = \begin{pmatrix} |\tilde{c}_e|^2 & \tilde{c}_e\tilde{c}_g^* \\ \tilde{c}_g\tilde{c}_e^* & |\tilde{c}_g|^2 \end{pmatrix}$$

and

$$\hat{L}_{\{\tilde{\rho}\}} = \Gamma \begin{pmatrix} -\tilde{\rho}_{ee} & -\tilde{\rho}_{eg}/2 \\ -\tilde{\rho}_{ge}/2 & \tilde{\rho}_{ee} \end{pmatrix}$$

is the Lindblad operator. $\Gamma = \dfrac{\omega^3 |\langle e|\,\hat{\mu}\,|g\rangle|^2}{3\pi\epsilon_0\hbar c^3}$ denotes the natural line width.

Writing out explicitly the equations for each density matrix elements, they are known as the optical Bloch equations

$$\begin{aligned}
\dot{\tilde{\rho}}_{ee} &= -\Gamma\tilde{\rho}_{ee} + \frac{i}{2}\left(\Omega^*\tilde{\rho}_{eg} - \Omega\tilde{\rho}_{ge}\right) \\
\dot{\tilde{\rho}}_{eg} &= \left(-\frac{\Gamma}{2} + i\Delta\right)\tilde{\rho}_{eg} + \frac{i}{2}\Omega\left(\tilde{\rho}_{ee} - \tilde{\rho}_{gg}\right) \\
\dot{\tilde{\rho}}_{ge} &= \dot{\tilde{\rho}}_{eg}^* \\
\dot{\tilde{\rho}}_{gg} &= -\dot{\tilde{\rho}}_{ee}.
\end{aligned}$$

This set of equations has steady state solution

$$\begin{aligned}
\tilde{\rho}_{ee}^{(s.s)} &= \frac{|\Omega|^2}{\Gamma^2 + 2|\Omega|^2 + 4\Delta^2} = \frac{1}{2}\frac{s}{1+s} \\
\tilde{\rho}_{eg}^{(s.s)} &= \frac{(2\Delta - i\Gamma)\Omega}{\Gamma^2 + 2|\Omega|^2 + 4\Delta^2} = \frac{2\Delta - i\Gamma}{\Omega^*}\frac{s}{1+s} \\
\tilde{\rho}_{ge}^{(s.s)} &= \frac{(2\Delta + i\Gamma)\Omega^*}{\Gamma^2 + 2|\Omega|^2 + 4\Delta^2} = \frac{2\Delta + i\Gamma}{\Omega}\frac{s}{1+s} \\
\tilde{\rho}_{gg}^{(s.s)} &= 1 - \tilde{\rho}_{ee}^{(s.s)},
\end{aligned}$$

where $s = \dfrac{I/I_{\text{sat}}}{1 + 4\Delta^2/\Gamma^2} = \dfrac{2\Omega^2}{\Gamma^2 + 4\Delta^2}$.

The force by this driving field can be calculated from the expectation value of its gradient

$$\begin{aligned}\mathbf{F} &= -\left\langle \nabla \hat{H}_{\text{rot}} \right\rangle = -\text{Tr}(\tilde{\rho} \nabla \hat{H}_{\text{rot}}) \\ &= -\frac{\hbar}{2}\left[\tilde{\rho}_{eg}(\nabla \Omega^*) + \tilde{\rho}_{ge}(\nabla \Omega)\right]\end{aligned}$$

The Force experience by the atom can be separated into a dissipative part, which comes from the phase gradient of the driving field, and a conservative part, which comes from its amplitude gradient. Writing $\nabla \Omega = (q_r + i q_i)\Omega$, it follows

$$\begin{aligned}\mathbf{F} &= -\frac{\hbar}{2}\left[(q_r - i q_i)(2\Delta - i\Gamma) + (q_r + i q_i)(2\Delta + i\Gamma)\right] \\ &= \frac{\hbar s}{1+s}\left[-\Delta q_r + \frac{\Gamma}{2} q_i\right]. \end{aligned} \tag{A.3}$$

The q_i term corresponds to the radiation pressure from the laser momentum kick. For a plane wave, $\phi(\mathbf{r}) = \mathbf{k} \cdot \mathbf{r}$, and $q_i = \mathbf{k}$. Intuitively the scattering force is the product of a single momentum transfer by the scattering rate

$$\mathbf{F}_{\text{abs}} = \hbar \mathbf{k} \frac{\Gamma}{2} \frac{s}{1+s}.$$

If Doppler effect is considered and an extra detuning $\Delta_{\text{Doppler}} = \mathbf{k} \cdot \mathbf{v}$ is included, one recovers equation 2.1

$$\mathbf{F}_{\text{abs}} = \hbar \mathbf{k} \frac{\Gamma}{2} \frac{s}{1+s}\left(1 + \frac{2\mathbf{k} \cdot \mathbf{v} \Delta}{(1+s)(\Delta^2 + \Gamma^2/4)}\right) = F_0 - \beta v.$$

The q_r term gives rise to the conservative dipole force, such as in the standing wave created by two counter propagating laser beams.

$$\begin{aligned} q_r &= \frac{\nabla \mathbf{E}_0 \cdot \langle e| \hat{\mu} |g\rangle + \mathbf{E}_0 \cdot \langle e| - e\nabla \vec{\mathbf{r}} |g\rangle}{\frac{\mathbf{E}_0}{\hbar} \cdot \langle e| \hat{\mu} |g\rangle} \\ &= \frac{1}{2}\frac{\nabla |\mathbf{E}_0|^2}{|\mathbf{E}_0|^2} = \frac{|\langle e| \hat{\mu} |g\rangle|^2}{\epsilon_0 c \hbar^2 |\Omega|^2} \nabla I(\mathbf{r}). \end{aligned}$$

The conservative dipole force therefore is

$$\mathbf{F}_{\text{dip}} = -\frac{\hbar\Delta s}{1+s} q_r = -\frac{3\pi c^3 \Gamma \Delta}{\omega_0^3 |\Omega|^2} \frac{s}{1+s} \nabla I(\mathbf{r}).$$

The corresponding dipole potential is

$$\begin{aligned} U_{\text{dip}}(\mathbf{r}) &= \frac{3\pi c^3 \Gamma \Delta}{\omega_0^3 |\Omega|^2} \frac{s}{1+s} I(\mathbf{r}) \\ &\overset{\text{large}\Delta}{\approx} -\frac{3\pi c^2}{2\omega_0^3} \frac{\Gamma}{\Delta} I(\mathbf{r}). \end{aligned}$$

This has the same form as equation 2.2 but only contains the $\omega - \omega_0$ term due to rotating wave approximation in the earlier derivations.

APPENDIX B
THERMODYNAMIC RELATIONS USED FOR EOS FIT

Ideal Fermi gas

A system of single component ideal fermi gas follow the grand partition function parametrized by the chemical potential μ, volume V and temperature T

$$\begin{aligned}\Xi(\mu, V, T) &= \sum_{N=0}^{\infty} e^{\beta\mu N} \mathcal{Z}_N(N, V, T) \\ &= \prod_{\alpha} \left[\sum_{n_\alpha} e^{\beta(\mu-\varepsilon_\alpha)n_\alpha} \right] \\ &= \prod_{\alpha} \left[1 + e^{\beta(\mu-\varepsilon_\alpha)}\right].\end{aligned}$$

The grand canonical potential is

$$\begin{aligned}\Omega &= -k_B T \ln \Xi \\ &= -k_B T \sum_{\alpha} \ln \left[1 + e^{\beta(\mu-\varepsilon_\alpha)}\right] \\ &= -k_B T \int_0^{\infty} \frac{4\pi V}{h^3} p^2 dp \ln\left(1 + e^{\beta\mu} e^{-\frac{\beta p^2}{2m}}\right) \\ &= \frac{k_B T V}{\lambda_{\text{dB}}^3} \text{Li}_{5/2}(-z).\end{aligned}$$

In the last line we have used the notations $z = e^{\beta\mu}$ for fugacity, $\lambda_{\text{dB}} = \dfrac{h}{\sqrt{2\pi m k_B T}}$ for thermal de Broglie wavelength, and $\text{Li}_n(z) = \sum_{k=1}^{\infty} \dfrac{z^k}{k^n}$ for the polylogarithm function.

One can obtain the equation of states (EOS)

$$N = -\left(\frac{\partial \Omega}{\partial \mu}\right)_{\beta,V} = z \left(\frac{\partial}{\partial z} \ln \Xi\right)_{\beta,V}$$

$$\begin{aligned}n = \frac{N}{V} &= -\frac{1}{\lambda_{\text{dB}}^3} z \frac{\partial}{\partial z} \text{Li}_{5/2}(-z) \\ &= -\frac{1}{\lambda_{\text{dB}}^3} \text{Li}_{3/2}(-z)\end{aligned} \tag{B.1}$$

and

$$P_0 V = -\Omega$$
$$P_0 = -\frac{k_B T}{\lambda_{\text{dB}}^3} \text{Li}_{5/2}(-z).$$

Here we have added subscript on pressure P to distinguish from the interacting case.

There are useful expansions on the above EOS at high temperature and low temperature limits. For large T, the polylogarithm functions are expanded in z. The expansion of P in terms of fugacity is also known as the Virial expansion.

$$P_0(\mu, T) = \frac{k_B T}{\lambda_{\text{dB}}^3} \sum_j b_j^{\text{ideal}} \left(e^{\beta\mu}\right)^j .$$

Apparently $b_j^{\text{ideal}} = \dfrac{(-1)^{j-1}}{j^{5/2}}$ based on the definition of polylogarithm function above.

At low temperature, the EOSs can be expanded in orders of $(\beta\mu)^{-2} = \left(\dfrac{k_B T}{\mu}\right)^2$, with the help of sommerfeld expansion:

$$\int_{-\infty}^{\infty} \frac{H(\varepsilon)}{1 + e^{\beta(\varepsilon-\mu)}} d\varepsilon = \int_{-\infty}^{\mu} H(\varepsilon) d\varepsilon + \frac{\pi^2}{6} (k_B T)^2 H'(\mu) + O(k_B T)^4.$$

For example, atom number $N = \int_0^{\infty} \dfrac{\rho(\varepsilon) d\varepsilon}{1 + e^{\beta(\varepsilon-\mu)}}$, where

$$\rho(\varepsilon) = \frac{V}{4\pi^2} \left(\frac{2m}{\hbar^2}\right)^{\frac{3}{2}} \sqrt{\varepsilon}$$

is the state density. Ignoring the exponentially small contribution from the integral along minus half of the real line, the atom number density can be expressed as

$$n = \frac{1}{4\pi^2} \left(\frac{2m}{\hbar^2}\right)^{\frac{3}{2}} \left[\frac{2}{3} \mu^{\frac{3}{2}} + \frac{\pi^2}{12} (k_B T)^2 \mu^{-\frac{1}{2}} + \dots\right]. \tag{B.2}$$

From which one can relate n to the Fermi energy $\varepsilon_F = \dfrac{\hbar^2}{2m} (6\pi^2 n)^{2/3}$, and obtain an expansion of finite temperature chemical potential μ in terms of T/T_F:

$$\mu = \varepsilon_F \left[1 - \frac{\pi^2}{12} \left(\frac{T}{T_F}\right)^2 + O(\frac{T}{T_F})^4\right].$$

A similar expansion for energy is

$$E = \int_0^\infty \frac{\rho(\varepsilon)\varepsilon d\varepsilon}{1+e^{\beta(\varepsilon-\mu)}} = \frac{3}{5}N\varepsilon_F\left[1+\frac{5\pi^2}{12}\left(\frac{T}{T_F}\right)^2+\dots\right].$$

The expression for pressure follows

$$P_0 = \frac{2}{3}\frac{E}{V} = \frac{1}{15\pi^2}\left(\frac{2m}{\hbar^2}\right)^{\frac{3}{2}}\varepsilon_F^{\frac{5}{2}}\left[1+\frac{5\pi^2}{12}\left(\frac{T}{T_F}\right)^2+\dots\right]$$
$$= \frac{1}{15\pi^2}\left(\frac{2m}{\hbar^2}\right)^{\frac{3}{2}}\mu^{\frac{5}{2}}\left[1+\frac{5}{2}\cdot\frac{5\pi^2}{12}\left(\frac{T}{T_F}\right)^2+O(\frac{T}{T_F})^4\right]\left[1+\frac{5\pi^2}{12}\left(\frac{T}{T_F}\right)^2+O(\frac{T}{T_F})^4\right]$$
$$P_0(\mu,T) = P_0(\mu,0)\left[1+\frac{5\pi^2}{8}\left(\frac{T}{T_F}\right)^2+\dots\right].$$

Spin-balanced interacting gas at unitarity

Finding the equation of states for interacting quantum gas is difficult. However, at unitarity where scattering length diverges, the EOS takes the same form as in an non-interacting ideal Fermi gas, with an extra correction function that only depends on $\beta\mu$:

$$P(\mu,T) = P_0(\mu,T)\times\psi(\beta\mu).$$

Under high temperature limit, the pressure EOS can still be written in a Virial expansion for each of the spin component, but the Virial coefficients are modified for the interactions. The pressure per spin is

$$P(\mu,T) = \frac{k_BT}{\lambda_{dB}^3}\sum_j b_j(e^{\beta\mu})^j, \tag{B.3}$$

with $b_1 = 1$, $b_2 = \frac{3\sqrt{2}}{8}$[153], and $b_3 = -0.29095295$[154].

the EOS for number density follows as

$$n = \left.\frac{\partial P}{\partial\mu}\right|_T = \frac{1}{\lambda_{\text{dB}}^3}\sum_j jb_j(e^{\beta\mu})^j. \tag{B.4}$$

And subsequently $\frac{T}{T_F} = \frac{4\pi}{(6\pi^2 n\lambda_{\text{dB}})^{2/3}}$ is a function of $\beta\mu$ only.

under low temperature limit, only two types of excitation exist — the Bogoliubov-Anderson phonons and the gapped Bogoliubov quasi-particles. They contribute to the excitation energy[155, 156].

$$E_{\text{ph+qp}} = \frac{3}{5}N\varepsilon_F\left[\xi + \frac{\sqrt{3}\pi^4}{16\xi^{3/2}}\left(\frac{T}{T_F}\right)^4 + \frac{5}{2}\sqrt{\frac{2\pi\Delta^3 T}{k_B^3 T_F^4}}\exp\left(-\frac{\Delta}{k_B T}\right)\right], \tag{B.5}$$

where ξ = 0.376 is the Bertsch parameter, ε_F is the Fermi energy for the spin component with density $n = N/V$, and Δ the paring gap.

$$\Delta \approx \left(\frac{2}{e}\right)^{7/3}\varepsilon_F \exp\left(\frac{\pi}{2k_F a}\right) \overset{a\to\infty}{=} C\varepsilon_F.$$

At Unitarity, the pairing gap is proportional to the Fermi energy by a constant factor $C = \left(\frac{2}{e}\right)^{7/3}$, and the relation $E = \frac{3}{2}PV$ still holds[157]. Hence the pressure can be written as a function of ε_F and T/T_F only.

$$P = \frac{2}{3}\frac{E}{V} = \frac{1}{15\pi^2}\left(\frac{2m}{\hbar^2}\right)^{\frac{3}{2}}\varepsilon_F^{\frac{5}{2}}\mathcal{G}(\tfrac{T}{T_F}), \tag{B.6}$$

where

$$\mathcal{G}(x) = \xi + \frac{\sqrt{3}\pi^4}{16\xi^{3/2}}x^4 + \frac{5}{2}\sqrt{2\pi C^3 x}\exp\left(-\frac{C}{x}\right).$$

For the purpose of EOS temperature fitting mentioned in chapter 3.2, it is also convenient to establish a relation between $\beta\mu$ and T/T_F through the following thermodynamic relations:

$$\begin{aligned} S &= \int_0^T \frac{dT'}{T'}\left(\frac{\partial E}{\partial T'}\right)_{N,V}, \\ F &= E - T\cdot S, \\ \beta\mu &= \frac{1}{k_B T}\left(\frac{\partial F}{\partial N}\right)_{V,T} = \frac{T_F}{T}\mathcal{G}(\tfrac{T}{T_F}) - \frac{3}{5}\int_0^T dT'\frac{\mathcal{G}(\frac{T}{T_F})}{T'}. \end{aligned} \tag{B.7}$$

APPENDIX C
ABSORPTION IMAGING

Absorption imaging is a widely used method to estimate the atom number and temperature of an atomic cloud. Shining a beam of resonant light on an atomic cloud, the reduction in the beam intensity follows

$$I = I_0 e^{\mathrm{OD}(x,y)} = I_0 e^{-n\sigma z}, \tag{C.1}$$

where n is the spatial density of the atom cloud, z is the thickness of the cloud along the imaging axis, and σ is the cross section for the imaging light

$$\sigma = \kappa \frac{3\lambda^2}{2\pi} \frac{1}{1 + I_0/I_{sat} + (2\Delta/\Gamma)^2}. \tag{C.2}$$

κ accounts for the Clebsch-Gordan coefficients in the allowed electric dipole transitions induced by the imaging light.

Due to the poissonian noise on the photon count from camera pixels, the best signal to noise ratio is obtained for an intermediate value of OD around 2.55. Practically, the OD is obtained from three imaging pictures to minimize the effect of stray light. In the first picture the camera exposes with the presence of the atom cloud and receives intensity I_{atoms}; In the second picture the imaging light is shined without atoms, and the camera receives intensity I_{light}; In the third picture the camera exposes a dark image while light is turned off, the intensity is I_{dark}. The measured optical density is:

$$\mathrm{OD} = \ln \frac{I_{light} - I_{dark}}{I_{atoms} - I_{dark}}. \tag{C.3}$$

From this measured OD, we can reconstruct the atom number

$$N_{atoms} = \frac{1}{\sigma} \int_{-\inf}^{\inf} \int_{-\inf}^{\inf} \mathrm{OD}\, dxdy. \tag{C.4}$$

For thermal cloud, the temperature can be estimate from the ballistic expansion speed using the time of flight (TOF) technique. By fitting the cloud size at various time of flight

$$\sigma(t) = \sqrt{\sigma_0^2 + \bar{v}^2 t^2}, \tag{C.5}$$

The root mean square velocity is obtained and the cloud temperature is $T = m\bar{v}^2/k_B$.

APPENDIX D
DMD SETUP

The DMD setup used to create homogeneous potential is shown in figure D.1(a). The green light source of model "Verdi V-10" provides 10 W power. The Beam after fiber is expanded to about 1 cm diameter after a telescope, so as to cover enough micromirrors on the DMD. The DMD chipset "DLP9500" contains a 1920 by 1080 array of micromirrors. Each mirror can be flipped to either the on ($+12^\circ$) or off (-12°) angle. The incident light shines at 24° angle with respect to the DMD surface normal to have the maximum diffraction power from the micromirrors in the "on" state. The diffracted beam is first cleaned up at its fourier plane by a pinhole of 2.5 mm diameter, to avoid noisy intensity spikes from the dithering algorithm. Then a portion of the intensity is shined on a camera. The intensity pattern on the camera is compared to the programmed pattern for real-time feedback on the DMD. The mirror positions are motorized by a controller module "Vialux VX4100" to converge to the designed pattern based on Floyd-Steinberg dithering algorithm [158]. An example picture for the intensity gradient is as shown in figure D.1(b). The rest of the power shines into the science cell in two 4-f configurations, which demagnifies the image by 20 times and gives a 5 μm resolution on the atoms. The peak intensity at the atoms position is about 3.0×10^7 W·m^{-2}, corresponding to a maximum dipole potential of around 2 μK, three times higher than what is needed for the gravity compensation over a 100 μm height. This leaves enough margin for the control program to model the intensity slope accurately.

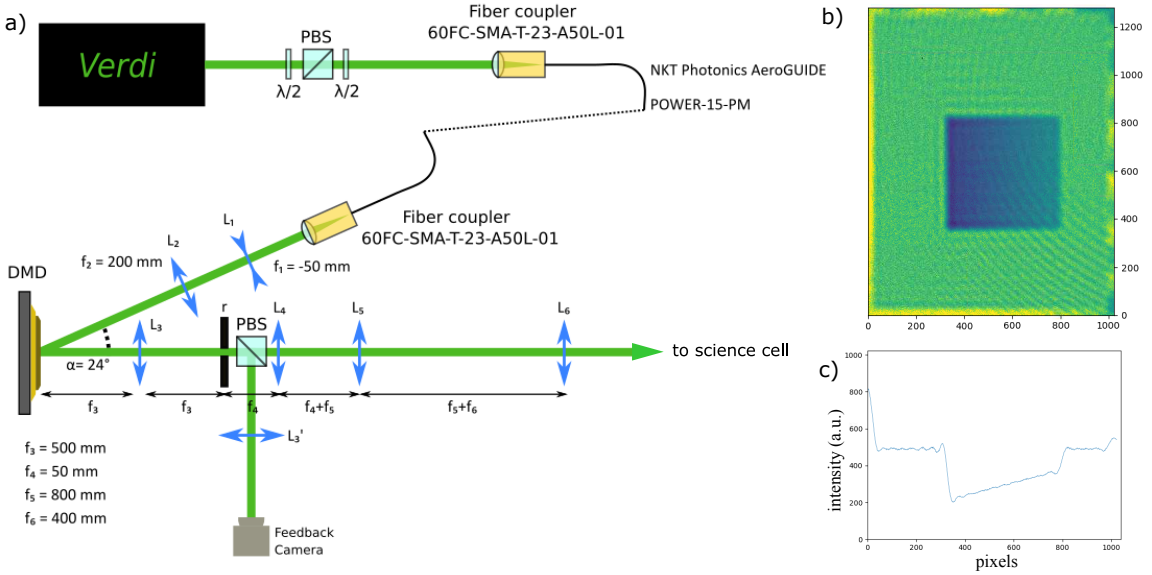

Figure D.1: a) Laser setup to prepare linear intensity gradient using the DMD. A camera is put in 4f configuration to monitor the intensity pattern and feedback on the micromirrors. At science cell the image is demagnified by 20 times and the intensity gradient can compensate gravity over a height of 100 μm. b) the intensity pattern seen by the monitor camera. c) the intensity along a vertical cut. the linearity of intensity is well realized within the region controlled by DMD diffraction.

REFERENCES

[1] T. Jennewein, C. Simon, G. Weihs, H. Weinfurter, and A. Zeilinger, "Quantum cryptography with entangled photons," *Physical review letters*, vol. 84, no. 20, p. 4729, 2000.

[2] D. Naik, C. Peterson, A. White, A. Berglund, and P. G. Kwiat, "Entangled state quantum cryptography: Eavesdropping on the ekert protocol," *Physical Review Letters*, vol. 84, no. 20, p. 4733, 2000.

[3] W. Tittel, J. Brendel, H. Zbinden, and N. Gisin, "Quantum cryptography using entangled photons in energy-time bell states," *Physical review letters*, vol. 84, no. 20, p. 4737, 2000.

[4] J. M. Chow *et al.*, "Universal quantum gate set approaching fault-tolerant thresholds with superconducting qubits," *Physical review letters*, vol. 109, no. 6, p. 060 501, 2012.

[5] R. Barends *et al.*, "Superconducting quantum circuits at the surface code threshold for fault tolerance," *Nature*, vol. 508, no. 7497, pp. 500–503, 2014.

[6] J. Benhelm, G. Kirchmair, C. F. Roos, and R. Blatt, "Towards fault-tolerant quantum computing with trapped ions," *Nature Physics*, vol. 4, no. 6, pp. 463–466, 2008.

[7] T. Harty *et al.*, "High-fidelity preparation, gates, memory, and readout of a trapped-ion quantum bit," *Physical review letters*, vol. 113, no. 22, p. 220 501, 2014.

[8] C. Figgatt *et al.*, "Parallel entangling operations on a universal ion-trap quantum computer," *Nature*, vol. 572, no. 7769, pp. 368–372, 2019.

[9] K. Maller *et al.*, "Rydberg-blockade controlled-not gate and entanglement in a two-dimensional array of neutral-atom qubits," *Physical Review A*, vol. 92, no. 2, p. 022 336, 2015.

[10] Y.-Y. Jau, A. Hankin, T. Keating, I. H. Deutsch, and G. Biedermann, "Entangling atomic spins with a rydberg-dressed spin-flip blockade," *Nature Physics*, vol. 12, no. 1, pp. 71–74, 2016.

[11] M. S. Grinolds *et al.*, "Nanoscale magnetic imaging of a single electron spin under ambient conditions," *Nature Physics*, vol. 9, no. 4, pp. 215–219, 2013.

[12] M. Ledbetter, K. Jensen, R. Fischer, A. Jarmola, and D. Budker, "Gyroscopes based on nitrogen-vacancy centers in diamond," *Physical Review A*, vol. 86, no. 5, p. 052 116, 2012.

[13] M. W. Doherty *et al.*, "Electronic properties and metrology applications of the diamond nv- center under pressure," *Physical review letters*, vol. 112, no. 4, p. 047 601, 2014.

[14] I. Bloch, J. Dalibard, and W. Zwerger, "Many-body physics with ultracold gases," *Reviews of modern physics*, vol. 80, no. 3, p. 885, 2008.

[15] M. Woerdemann, C. Alpmann, M. Esseling, and C. Denz, "Advanced optical trapping by complex beam shaping," *Laser & Photonics Reviews*, vol. 7, no. 6, pp. 839–854, 2013.

[16] C. Chin, R. Grimm, P. Julienne, and E. Tiesinga, "Feshbach resonances in ultracold gases," *Reviews of Modern Physics*, vol. 82, no. 2, p. 1225, 2010.

[17] J. G. Bednorz and K. A. Müller, "Possible hight c superconductivity in the ba- lacu- o system," *Zeitschrift für Physik B Condensed Matter*, vol. 64, no. 2, pp. 189–193, 1986.

[18] M. N. Baibich *et al.*, "Giant magnetoresistance of (001) fe/(001) cr magnetic superlattices," *Physical review letters*, vol. 61, no. 21, p. 2472, 1988.

[19] I. Bloch, J. Dalibard, and S. Nascimbene, "Quantum simulations with ultracold quantum gases," *Nature Physics*, vol. 8, no. 4, pp. 267–276, 2012.

[20] J. Bardeen, L. N. Cooper, and J. R. Schrieffer, "Theory of superconductivity," *Physical review*, vol. 108, no. 5, p. 1175, 1957.

[21] L. N. Cooper, "Bound electron pairs in a degenerate fermi gas," *Physical Review*, vol. 104, no. 4, p. 1189, 1956.

[22] F. Werner and Y. Castin, "Unitary gas in an isotropic harmonic trap: Symmetry properties and applications," *Physical Review A*, vol. 74, no. 5, p. 053 604, 2006.

[23] S. Tan, "Energetics of a strongly correlated fermi gas," *Annals of Physics*, vol. 323, no. 12, pp. 2952–2970, 2008.

[24] NASA. "Chandra x-ray observatory, Multiwavelength images of psr b1509-58." (2009), (visited on 08/18/2022).

[25] H. Feshbach, "Unified theory of nuclear reactions," *Annals of Physics*, vol. 5, no. 4, pp. 357–390, 1958.

[26] H. Feshbach, "A unified theory of nuclear reactions. ii," *Annals of Physics*, vol. 19, no. 2, pp. 287–313, 1962.

[27] S Inouye, M. Andrews, J Stenger, H.-J. Miesner, D. M. Stamper-Kurn, and W Ketterle, "Observation of feshbach resonances in a bose–einstein condensate," *Nature*, vol. 392, no. 6672, pp. 151–154, 1998.

[28] P. Courteille, R. Freeland, D. J. Heinzen, F. Van Abeelen, and B. Verhaar, "Observation of a feshbach resonance in cold atom scattering," *Physical review letters*, vol. 81, no. 1, p. 69, 1998.

[29] B. DeMarco and D. S. Jin, "Onset of fermi degeneracy in a trapped atomic gas," *science*, vol. 285, no. 5434, pp. 1703–1706, 1999.

[30] A. G. Truscott, K. E. Strecker, W. I. McAlexander, G. B. Partridge, and R. G. Hulet, "Observation of fermi pressure in a gas of trapped atoms," *Science*, vol. 291, no. 5513, pp. 2570–2572, 2001.

[31] F Schreck *et al.*, "Quasipure bose-einstein condensate immersed in a fermi sea," *Physical Review Letters*, vol. 87, no. 8, p. 080 403, 2001.

[32] G Roati, F Riboli, G Modugno, and M Inguscio, "Fermi-bose quantum degenerate k 40- r 87 b mixture with attractive interaction," *Physical Review Letters*, vol. 89, no. 15, p. 150 403, 2002.

[33] S. Granade, M. Gehm, K. O'Hara, and J. Thomas, "All-optical production of a degenerate fermi gas," *Physical Review Letters*, vol. 88, no. 12, p. 120 405, 2002.

[34] S. Jochim *et al.*, "Bose-einstein condensation of molecules," *Science*, vol. 302, no. 5653, pp. 2101–2103, 2003.

[35] K Dieckmann, C. Stan, S Gupta, Z Hadzibabic, C. Schunck, and W Ketterle, "Decay of an ultracold fermionic lithium gas near a feshbach resonance," *Physical review letters*, vol. 89, no. 20, p. 203 201, 2002.

[36] T. Loftus, C. A. Regal, C Ticknor, J. L. Bohn, and D. S. Jin, "Resonant control of elastic collisions in an optically trapped fermi gas of atoms," *Physical review letters*, vol. 88, no. 17, p. 173 201, 2002.

[37] K. OHara *et al.*, "Measurement of the zero crossing in a feshbach resonance of fermionic 6 li," *Physical Review A*, vol. 66, no. 4, p. 041 401, 2002.

[38] S Jochim *et al.*, "Magnetic field control of elastic scattering in a cold gas of fermionic lithium atoms," *Physical review letters*, vol. 89, no. 27, p. 273 202, 2002.

[39] M. Greiner, C. A. Regal, and D. S. Jin, "Emergence of a molecular bose–einstein condensate from a fermi gas," *Nature*, vol. 426, no. 6966, pp. 537–540, 2003.

[40] M Bartenstein *et al.*, "Crossover from a molecular bose-einstein condensate to a degenerate fermi gas," *Physical review letters*, vol. 92, no. 12, p. 120 401, 2004.

[41] M. W. Zwierlein *et al.*, "Observation of bose-einstein condensation of molecules," *Physical review letters*, vol. 91, no. 25, p. 250 401, 2003.

[42] C. Regal, M. Greiner, and D. S. Jin, "Observation of resonance condensation of fermionic atom pairs," *Physical review letters*, vol. 92, no. 4, p. 040 403, 2004.

[43] T. Bourdel *et al.*, "Experimental study of the bec-bcs crossover region in lithium 6," *Physical Review Letters*, vol. 93, no. 5, p. 050 401, 2004.

[44] J. Kinast, A. Turlapov, J. E. Thomas, Q. Chen, J. Stajic, and K. Levin, "Heat capacity of a strongly interacting fermi gas," *Science*, vol. 307, no. 5713, pp. 1296–1299, 2005.

[45] J. Kinast, S. Hemmer, M. Gehm, A Turlapov, and J. Thomas, "Evidence for superfluidity in a resonantly interacting fermi gas," *Physical Review Letters*, vol. 92, no. 15, p. 150 402, 2004.

[46] M Bartenstein *et al.*, "Collective excitations of a degenerate gas at the bec-bcs crossover," *Physical review letters*, vol. 92, no. 20, p. 203 201, 2004.

[47] C Chin *et al.*, "Observation of the pairing gap in a strongly interacting fermi gas," *Science*, vol. 305, no. 5687, pp. 1128–1130, 2004.

[48] G. B. Partridge, K. E. Strecker, R. I. Kamar, M. W. Jack, and R. G. Hulet, "Molecular probe of pairing in the bec-bcs crossover," *Physical Review Letters*, vol. 95, no. 2, p. 020 404, 2005.

[49] M. W. Zwierlein, J. R. Abo-Shaeer, A. Schirotzek, C. H. Schunck, and W. Ketterle, "Vortices and superfluidity in a strongly interacting fermi gas," *Nature*, vol. 435, no. 7045, pp. 1047–1051, 2005.

[50] S. Nascimbène, N. Navon, K. Jiang, F. Chevy, and C. Salomon, "Exploring the thermodynamics of a universal fermi gas," *Nature*, vol. 463, no. 7284, pp. 1057–1060, 2010.

[51] M. J. Ku, A. T. Sommer, L. W. Cheuk, and M. W. Zwierlein, "Revealing the superfluid lambda transition in the universal thermodynamics of a unitary fermi gas," *Science*, vol. 335, no. 6068, pp. 563–567, 2012.

[52] M. Horikoshi, S. Nakajima, M. Ueda, and T. Mukaiyama, "Measurement of universal thermodynamic functions for a unitary fermi gas," *Science*, vol. 327, no. 5964, pp. 442–445, 2010.

[53] N. Navon, S. Nascimbene, F. Chevy, and C. Salomon, "The equation of state of a low-temperature fermi gas with tunable interactions," *Science*, vol. 328, no. 5979, pp. 729–732, 2010.

[54] S. Tan, "Generalized virial theorem and pressure relation for a strongly correlated fermi gas," *Annals of Physics*, vol. 323, no. 12, pp. 2987–2990, 2008.

[55] S. Tan, "Large momentum part of a strongly correlated fermi gas," *Annals of Physics*, vol. 323, no. 12, pp. 2971–2986, 2008.

[56] J. Stewart, J. Gaebler, T. Drake, and D. Jin, "Verification of universal relations in a strongly interacting fermi gas," *Physical Review Letters*, vol. 104, no. 23, p. 235 301, 2010.

[57] Y. Sagi, T. E. Drake, R. Paudel, and D. S. Jin, "Measurement of the homogeneous contact of a unitary fermi gas," *Physical review letters*, vol. 109, no. 22, p. 220 402, 2012.

[58] B. Mukherjee, P. B. Patel, Z. Yan, R. J. Fletcher, J. Struck, and M. W. Zwierlein, "Spectral response and contact of the unitary fermi gas," *Physical review letters*, vol. 122, no. 20, p. 203 402, 2019.

[59] E. Kuhnle, S Hoinka, P Dyke, H Hu, P Hannaford, and C. Vale, "Temperature dependence of the universal contact parameter in a unitary fermi gas," *Physical Review Letters*, vol. 106, no. 17, p. 170 402, 2011.

[60] C Carcy *et al.*, "Contact and sum rules in a near-uniform fermi gas at unitarity," *Physical Review Letters*, vol. 122, no. 20, p. 203 401, 2019.

[61] S. Laurent, M. Pierce, M. Delehaye, T. Yefsah, F. Chevy, and C. Salomon, "Connecting few-body inelastic decay to quantum correlations in a many-body system: A weakly coupled impurity in a resonant fermi gas," *Physical review letters*, vol. 118, no. 10, p. 103 403, 2017.

[62] W. S. Bakr *et al.*, "Probing the superfluid–to–mott insulator transition at the single-atom level," *Science*, vol. 329, no. 5991, pp. 547–550, 2010.

[63] J. F. Sherson, C. Weitenberg, M. Endres, M. Cheneau, I. Bloch, and S. Kuhr, "Single-atom-resolved fluorescence imaging of an atomic mott insulator," *Nature*, vol. 467, no. 7311, pp. 68–72, 2010.

[64] J. Simon, W. S. Bakr, R. Ma, M. E. Tai, P. M. Preiss, and M. Greiner, "Quantum simulation of antiferromagnetic spin chains in an optical lattice," *Nature*, vol. 472, no. 7343, pp. 307–312, 2011.

[65] M. Cheneau *et al.*, "Light-cone-like spreading of correlations in a quantum many-body system," *Nature*, vol. 481, no. 7382, pp. 484–487, 2012.

[66] T. Fukuhara *et al.*, "Quantum dynamics of a mobile spin impurity," *Nature Physics*, vol. 9, no. 4, pp. 235–241, 2013.

[67] S. Hild *et al.*, "Far-from-equilibrium spin transport in heisenberg quantum magnets," *Physical review letters*, vol. 113, no. 14, p. 147 205, 2014.

[68] P. M. Preiss *et al.*, "Strongly correlated quantum walks in optical lattices," *Science*, vol. 347, no. 6227, pp. 1229–1233, 2015.

[69] T. Fukuhara *et al.*, "Microscopic observation of magnon bound states and their dynamics," *Nature*, vol. 502, no. 7469, pp. 76–79, 2013.

[70] T. Fukuhara *et al.*, "Spatially resolved detection of a spin-entanglement wave in a bose-hubbard chain," *Physical review letters*, vol. 115, no. 3, p. 035 302, 2015.

[71] R. Islam *et al.*, "Measuring entanglement entropy in a quantum many-body system," *Nature*, vol. 528, no. 7580, pp. 77–83, 2015.

[72] P. Schauß *et al.*, "Observation of spatially ordered structures in a two-dimensional rydberg gas," *Nature*, vol. 491, no. 7422, pp. 87–91, 2012.

[73] P. Schauß *et al.*, "Crystallization in ising quantum magnets," *Science*, vol. 347, no. 6229, pp. 1455–1458, 2015.

[74] J. Zeiher, P. Schauß, S. Hild, T. Macrì, I. Bloch, and C. Gross, "Microscopic characterization of scalable coherent rydberg superatoms," *Physical Review X*, vol. 5, no. 3, p. 031 015, 2015.

[75] E. Haller *et al.*, "Single-atom imaging of fermions in a quantum-gas microscope," *Nature Physics*, vol. 11, no. 9, pp. 738–742, 2015.

[76] G. J. Edge *et al.*, "Imaging and addressing of individual fermionic atoms in an optical lattice," *Physical Review A*, vol. 92, no. 6, p. 063 406, 2015.

[77] A. Omran *et al.*, "Microscopic observation of pauli blocking in degenerate fermionic lattice gases," *Physical review letters*, vol. 115, no. 26, p. 263 001, 2015.

[78] M. F. Parsons *et al.*, "Site-resolved imaging of fermionic li 6 in an optical lattice," *Physical review letters*, vol. 114, no. 21, p. 213 002, 2015.

[79] L. W. Cheuk *et al.*, "Quantum-gas microscope for fermionic atoms," *Physical review letters*, vol. 114, no. 19, p. 193 001, 2015.

[80] L. W. Cheuk, M. A. Nichols, K. R. Lawrence, M. Okan, H. Zhang, and M. W. Zwierlein, "Observation of 2d fermionic mott insulators of k 40 with single-site resolution," *Physical review letters*, vol. 116, no. 23, p. 235 301, 2016.

[81] D. Greif *et al.*, "Site-resolved imaging of a fermionic mott insulator," *Science*, vol. 351, no. 6276, pp. 953–957, 2016.

[82] M. F. Parsons, A. Mazurenko, C. S. Chiu, G. Ji, D. Greif, and M. Greiner, "Site-resolved measurement of the spin-correlation function in the fermi-hubbard model," *Science*, vol. 353, no. 6305, pp. 1253–1256, 2016.

[83] L. W. Cheuk *et al.*, "Observation of spatial charge and spin correlations in the 2d fermi-hubbard model," *Science*, vol. 353, no. 6305, pp. 1260–1264, 2016.

[84] M. Boll *et al.*, "Spin-and density-resolved microscopy of antiferromagnetic correlations in fermi-hubbard chains," *Science*, vol. 353, no. 6305, pp. 1257–1260, 2016.

[85] A. L. Gaunt, T. F. Schmidutz, I. Gotlibovych, R. P. Smith, and Z. Hadzibabic, "Bose-einstein condensation of atoms in a uniform potential," *Physical review letters*, vol. 110, no. 20, p. 200 406, 2013.

[86] L. Chomaz *et al.*, "Emergence of coherence via transverse condensation in a uniform quasi-two-dimensional bose gas," *Nature communications*, vol. 6, no. 1, pp. 1–10, 2015.

[87] K. Hueck, N. Luick, L. Sobirey, J. Siegl, T. Lompe, and H. Moritz, "Two-dimensional homogeneous fermi gases," *Physical review letters*, vol. 120, no. 6, p. 060 402, 2018.

[88] P. Fulde and R. A. Ferrell, "Superconductivity in a strong spin-exchange field," *Physical Review*, vol. 135, no. 3A, A550, 1964.

[89] A. Larkin and I. Ovchinnikov, "Inhomogeneous state of superconductors(production of superconducting state in ferromagnet with fermi surfaces, examining green function)," *Soviet Physics-JETP*, vol. 20, pp. 762–769, 1965.

[90] A. M. Clogston, "Upper limit for the critical field in hard superconductors," *Physical Review Letters*, vol. 9, no. 6, p. 266, 1962.

[91] S. Jin, "A new generation experiment for the study of strongly interacting fermi gases," Ph.D. dissertation, École Normale Supérieure, 2019.

[92] B. N. Laboratory. "Isotopes of lithium." (2008), (visited on 04/27/2022).

[93] P. Duarte *et al.*, "All-optical production of a lithium quantum gas using narrow-line laser cooling," *Physical Review A*, vol. 84, no. 6, p. 061 406, 2011.

[94] M. E. Ghem, *Properties of 6li*, 2003.

[95] G. Breit and I. Rabi, "Measurement of nuclear spin," *Physical Review*, vol. 38, no. 11, p. 2082, 1931.

[96] D. McCarron, S. King, and S. Cornish, "Modulation transfer spectroscopy in atomic rubidium," *Measurement science and technology*, vol. 19, no. 10, p. 105 601, 2008.

[97] G Ritt, G Cennini, C Geckeler, and M Weitz, "Laser frequency offset locking using a side of filter technique," *Applied Physics B*, vol. 79, no. 3, pp. 363–365, 2004.

[98] H. J. Metcalf and P. Van der Straten, "Laser cooling and trapping of neutral atoms," *The Optics Encyclopedia: Basic Foundations and Practical Applications*, 2007.

[99] G. Salomon, L. Fouché, P. Wang, A. Aspect, P. Bouyer, and T. Bourdel, "Gray-molasses cooling of 39k to a high phase-space density," *EPL (Europhysics Letters)*, vol. 104, no. 6, p. 63 002, 2014.

[100] D. R. Fernandes, "Trapping and cooling of fermionic alkali atoms to quantum degeneracy. sub-doppler cooling of potassium-40 and lithium-6 in gray molasses," Ph.D. dissertation, Université Pierre et Marie Curie, 2014.

[101] G. Valtolina, "superfluid and spin dynamics of strongly interacting atomic fermi gases," Ph.D. dissertation, proefschrift (Scuola Normale Superiore, Pisa, 2016), 2016.

[102] G. Colzi, "A new apparatus to simulate fundamental interactions with ultracold atoms," Ph.D. dissertation, University of Trento, 2018.

[103] C. Cohen-Tannoudji, "Physique atomique et moléculaire, 1973-2004," *Lannuaire du Collège de France. Cours et travaux*, no. 112, pp. 776–778, 2013.

[104] F Papoff, F Mauri, and E. Arimondo, "Transient velocity-selective coherent population trapping in one dimension," *JOSA B*, vol. 9, no. 3, pp. 321–331, 1992.

[105] R. Grimm, M. Weidemüller, and Y. B. Ovchinnikov, "Optical dipole traps for neutral atoms," in *Advances in atomic, molecular, and optical physics*, vol. 42, Elsevier, 2000, pp. 95–170.

[106] A. Ashkin, "Acceleration and trapping of particles by radiation pressure," *Physical review letters*, vol. 24, no. 4, p. 156, 1970.

[107] W. Ketterle and N. Van Druten, "Evaporative cooling of trapped atoms," in *Advances in atomic, molecular, and optical physics*, vol. 37, Elsevier, 1996, pp. 181–236.

[108] H. F. Hess, "Evaporative cooling of magnetically trapped and compressed spin-polarized hydrogen," *Physical Review B*, vol. 34, no. 5, p. 3476, 1986.

[109] N. Masuhara *et al.*, "Evaporative cooling of spin-polarized atomic hydrogen," *Physical Review Letters*, vol. 61, no. 8, p. 935, 1988.

[110] J. Dalibard, "Collisional dynamics of ultra-cold atomic gases," in *Bose-Einstein Condensation in Atomic Gases*, IOS Press, 1999, pp. 321–349.

[111] M. Gehm, S. Hemmer, K. OHara, and J. Thomas, "Unitarity-limited elastic collision rate in a harmonically trapped fermi gas," *Physical Review A*, vol. 68, no. 1, p. 011 603, 2003.

[112] A. Moerdijk, B. Verhaar, and A Axelsson, "Resonances in ultracold collisions of li 6, li 7, and na 23," *Physical Review A*, vol. 51, no. 6, p. 4852, 1995.

[113] G. Zürn, T. Lompe, A. N. Wenz, S. Jochim, P. Julienne, and J. Hutson, "Precise characterization of li 6 feshbach resonances using trap-sideband-resolved rf spectroscopy of weakly bound molecules," *Physical review letters*, vol. 110, no. 13, p. 135 301, 2013.

[114] L. Landau, "Zur theorie der energie übertragung, ii. phys. z. sowjetunion 2 (1932) 46; c. zener, non-adiabatic crossing of energy levels," *Proc. R. Soc. London Ser. A*, vol. 137, p. 696, 1932.

[115] C. Zener, "Non-adiabatic crossing of energy levels," *Proceedings of the Royal Society of London. Series A, Containing Papers of a Mathematical and Physical Character*, vol. 137, no. 833, pp. 696–702, 1932.

[116] A. Omran, "A microscope for fermi gases," Ph.D. dissertation, Ludwig Maximilians Universität München, 2016.

[117] M. F. Parsons, "Probing the hubbard model with single-site resolution," Ph.D. dissertation, 2016.

[118] C. Gross and W. S. Bakr, "Quantum gas microscopy for single atom and spin detection," *Nature Physics*, vol. 17, no. 12, pp. 1316–1323, 2021.

[119] W. Ketterle and M. W. Zwierlein, "Making, probing and understanding ultracold fermi gases," *La Rivista del Nuovo Cimento*, vol. 31, no. 5, pp. 247–422, 2008.

[120] Y. Castin, "Exact scaling transform for a unitary quantum gas in a time dependent harmonic potential," *Comptes Rendus Physique*, vol. 5, no. 3, pp. 407–410, 2004.

[121] T.-L. Ho and Q. Zhou, "Obtaining the phase diagram and thermodynamic quantities of bulk systems from the densities of trapped gases," *Nature Physics*, vol. 6, no. 2, pp. 131–134, 2010.

[122] S. Jin *et al.*, in preparation, 2022.

[123] F. Werner, "Virial theorems for trapped cold atoms," *Physical Review A*, vol. 78, no. 2, p. 025 601, 2008.

[124] P. L. Kapitza, "Viscosity of liquid helium below the λ-point," *Nature*, vol. 141, pp. 74–74, 1938.

[125] J. F. Allen and A. Misener, "Flow of liquid helium ii," *Nature*, vol. 141, no. 3558, pp. 75–75, 1938.

[126] F. London, "The λ-phenomenon of liquid helium and the bose-einstein degeneracy," *Nature*, vol. 141, no. 3571, pp. 643–644, 1938.

[127] L. Tisza, "Transport phenomena in helium ii," *Nature*, vol. 141, no. 3577, pp. 913–913, 1938.

[128] L. Landau, "Theory of the superfluidity of helium ii," *Physical Review*, vol. 60, no. 4, p. 356, 1941.

[129] A. J. Leggett, "A theoretical description of the new phases of liquid he 3," *Reviews of Modern Physics*, vol. 47, no. 2, p. 331, 1975.

[130] M Houbiers, R Ferwerda, H. Stoof, W. McAlexander, C. Sackett, and R. Hulet, "Superfluid state of atomic 6 li in a magnetic trap," *Physical Review A*, vol. 56, no. 6, p. 4864, 1997.

[131] C. Regal, M. Greiner, and D. S. Jin, "Observation of resonance condensation of fermionic atom pairs," *Physical review letters*, vol. 92, no. 4, p. 040 403, 2004.

[132] M. Zwierlein, C. Stan, C. Schunck, S. Raupach, A. Kerman, and W Ketterle, "Condensation of pairs of fermionic atoms near a feshbach resonance," *Physical Review Letters*, vol. 92, no. 12, p. 120 403, 2004.

[133] C. Lobo, A Recati, S Giorgini, and S Stringari, "Normal state of a polarized fermi gas at unitarity," *Physical Review Letters*, vol. 97, no. 20, p. 200 403, 2006.

[134] A Recati, C Lobo, and S Stringari, "Role of interactions in spin-polarized atomic fermi gases at unitarity," *Physical Review A*, vol. 78, no. 2, p. 023 633, 2008.

[135] M. W. Zwierlein, A. Schirotzek, C. H. Schunck, and W. Ketterle, "Fermionic superfluidity with imbalanced spin populations," *Science*, vol. 311, no. 5760, pp. 492–496, 2006.

[136] J. Verstraten, *Developing single-atom imaging of the unitary fermi gas in an optical lattice*, 2019.

[137] E. A. Donley, T. P. Heavner, F. Levi, M. Tataw, and S. R. Jefferts, "Double-pass acousto-optic modulator system," *Review of Scientific Instruments*, vol. 76, no. 6, p. 063 112, 2005.

[138] M. Gehm, K. Ohara, T. Savard, and J. Thomas, "Dynamics of noise-induced heating in atom traps," *Physical Review A*, vol. 58, no. 5, p. 3914, 1998.

[139] P. Kapitza and P. Dirac, "The reflection of electrons from standing light waves," in *Mathematical Proceedings of the Cambridge Philosophical Society*, Cambridge University Press, vol. 29, 1933, pp. 297–300.

[140] S. Gupta, A. E. Leanhardt, A. D. Cronin, and D. E. Pritchard, "Coherent manipulation of atoms with standing light waves," *Comptes Rendus de l'Académie des Sciences-Series IV-Physics*, vol. 2, no. 3, pp. 479–495, 2001.

[141] F. Gerbier, *Quantum gases in optical lattices*, Lecture at Sorbonne Université Campus Pierre et Marie Curie, 2015.

[142] A. Messiah, *Albert Messiah: Mécanique quantique. Tome 2*. Walter de Gruyter GmbH & Co KG, 2020.

[143] M. P. Marder, *Condensed matter physics*. John Wiley & Sons, 2010.

[144] J. Dalibard, "Des cages de lumière pour les atomes: La physique des pièges et des réseaux optiques," *Cours du Collège de France*, 2013.

[145] G. J. Edge *et al.*, "Imaging and addressing of individual fermionic atoms in an optical lattice," *Physical Review A*, vol. 92, no. 6, p. 063 406, 2015.

[146] D. A. Cotta, "A single-site resolution fermionic quantum-gas microscope," Ph.D. dissertation, University of Strathclyde, 2018.

[147] R. Han, H. Khoon Ng, and B.-G. Englert, "Raman transitions without adiabatic elimination: A simple and accurate treatment," *Journal of Modern Optics*, vol. 60, no. 4, pp. 255–265, 2013.

[148] Z. Yan, P. B. Patel, B. Mukherjee, R. J. Fletcher, J. Struck, and M. W. Zwierlein, "Boiling a unitary fermi liquid," *Physical Review Letters*, vol. 122, no. 9, p. 093 401, 2019.

[149] A. Schirotzek, C.-H. Wu, A. Sommer, and M. W. Zwierlein, "Observation of fermi polarons in a tunable fermi liquid of ultracold atoms," *Physical review letters*, vol. 102, no. 23, p. 230 402, 2009.

[150] M. Zwierlein, C. Schunck, C. Stan, S. Raupach, and W Ketterle, "Formation dynamics of a fermion pair condensate," *Physical review letters*, vol. 94, no. 18, p. 180 401, 2005.

[151] F. Werner, private communication.

[152] M. O. Scully and M. S. Zubairy, *Quantum optics*, 1999.

[153] E. Beth and G. E. Uhlenbeck, "The quantum theory of the non-ideal gas. ii. behaviour at low temperatures," *Physica*, vol. 4, no. 10, pp. 915–924, 1937.

[154] X.-J. Liu, H. Hu, and P. D. Drummond, "Virial expansion for a strongly correlated fermi gas," *Physical review letters*, vol. 102, no. 16, p. 160 401, 2009.

[155] A. Bulgac, J. E. Drut, and P. Magierski, "Spin 1/2 fermions in the unitary regime: A superfluid of a new type," *Physical review letters*, vol. 96, no. 9, p. 090 404, 2006.

[156] J Carlson, S.-Y. Chang, V. Pandharipande, and K. E. Schmidt, "Superfluid fermi gases with large scattering length," *Physical review letters*, vol. 91, no. 5, p. 050 401, 2003.

[157] T.-L. Ho, "Universal thermodynamics of degenerate quantum gases in the unitarity limit," *Physical review letters*, vol. 92, no. 9, p. 090 402, 2004.

[158] R. W. Floyd, "An adaptive algorithm for spatial gray-scale," in *Proc. Soc. Inf. Disp.*, vol. 17, 1976, pp. 75–77.

DEDICATION

This dedication goes to my supervisors, my colleagues and my family.

I would like to thank Tarik for the guidance throughout my thesis project, and for always being patient in teaching me the laboratory and writing skills. I would like to thank Christophe and Antoine for the overall supervision. It is my great pleasure to have worked on this large project together with Joris, Tim, Maxim, Shuwei and Bruno, from whom I have learned the most and have received the most support. I thank Julian, Clement and Gentle also for their support and accompany. I must express my gratitude to my parents, who always hang on to me despite of the large physical distance. At last I would like to put a place holder for my love, who has not come into my life yet but surely will deserve a line in this dedication.

SUMMARY

Cette thèse sinscrit dans le cadre général de la simulation quantique avec pour système détude un mélange de fermions en interaction forte. En particulier, l'équipe souhaite étudier avec une haute résolution spatiale des nuages spatialement homogènes à l'aide d'un microscope à gaz quantique. Le manuscrit est divisé en six chapitres:

- Le premier chapitre décrit le montage expérimental et les différents lasers utilisés dans les expériences.
- Le deuxième chapitre développe les étapes pour aboutir à un nuage ultra-froid dans la chambre de science : chargement dun piège magnéto-optique, refroidissement dans une mélasse rouge puis bleue, transport par pince optique dans la chambre de science puis chargement dans un piège dipolaire croisé.
- Le troisième chapitre décrit létape de refroidissement évaporatif avec la méthode utilisée pour mesurer la température ainsi que lobservation du régime superfluide.
- Le quatrième sintéresse au système dimagerie. La mesure se faisant par fluorescence avec une résolution spatiale espérée de lordre du micron, un objectif de grande ouverture numérique est nécessaire et a été caractérisé.
- Il faut rajouter un réseau optique de blocage (pinning lattice) afin que les atomes ńne bougent pasż pendant la durée dimagerie qui prendra plusieurs dizaines voire centaines de millisecondes. Cet réseau de blocage est caractérisé dans le cinquième chapitre via méthodes de chauffage paramétrique. Le chapitre se poursuit par une expérience de ńband mappingż et une étude de lefficacité du blocage par le réseau.
- Le sixième chapitre décrit létape indispensable pour observer des atomes uniques par imagerie: le refroidissement Raman par bandes latérales dans le réseau de blocage. L'effet de refroidissement est démontré par le spectre Raman clairement résolu et l'extension de la durée de vie des atomes dans le réseau. Le chapitre se termine par une première image de fluorescence des atomes individuels.

RÉSUMÉ

Cette thèse présente une expérience de nouvelle génération dédiée à l'étude de gaz quantique ^{6}Li, dotée de vastes capacités et visant à étudier les propriétés microscopiques d'un gas de Fermi à fortes interactions au voisinage et sous le seuil de la transition suerfluide. Sur ce dispositif, nous sommes parvenus à refroidir les atomes ^{6}Li jusqu'à un état fortement dégénéré grâce à une séquence de refroidissment d'une durée de 13 s. Avec un réseau optique correctement caractérisé et d'un microscope à haute résolution, le montage a été préparé pour enregistrer des images de fluorescence à l'échelle de l'atome individuel.

Cette expérience sera un puissant outil pour l'étude des corrélations dans les systèmes de Fermi en fortes interactions. En combinaison avec des potentiels optiques correctement ajustés, nous pouvons étendre nos measures à des gas homogénes et à la recherche de phases superfluides avec différentes populations de spins.

MOTS CLÉS

Gaz Ultrafroid --- Fermions en interaction forte --- Superfluidité --- Imagerie d'atomes individuels

ABSTRACT

This thesis presents our new generation ^{6}Li-based quantum gas experiment with wide-ranging capabilities, mainly aiming to study the microscopic properties of strongly interacting Fermi gases near and below the superfluid transition. On this setup, we have achieved efficient cooling of the ^{6}Li atoms to deep quantum degeneracy within 13 s sequence duration. With a well characterized pinning lattice and a high-resolution microscope objective, the machine has been prepared to take single-atom fluorescence images of bulk ultracold Fermi gases.

This machine will serve as a powerful tool to study the correlations in strongly interacting Fermi systems. Combining with tailored optical potentials, we can extend our measurements to homogeneous gases and search for exotic spin-imbalanced superfluid phases.

KEYWORDS

Ultracold Gases --- Strongly Interacting Fermions --- Superfluidity --- Single Atom Imaging